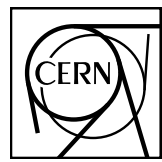


EUROPEAN ORGANIZATION FOR NUCLEAR RESEARCH



ALICE-ANA-2019-981
May 29, 2020

p_T -differential production of J/ψ in Pb–Pb collisions at $\sqrt{s_{NN}} = 5.02$ TeV with the 2015 and 2018 data samples

C. Hadjidakis¹, C.L. Huang¹, L. Massacrier¹

1. Institut de Physique Nucléaire d'Orsay

Contact Email : chun-lu.huang@cern.ch

Abstract

We report on the nuclear modification factor R_{AA} measurements of inclusive J/ψ production in Pb–Pb collisions at $\sqrt{s_{NN}} = 5.02$ TeV. J/ψ are measured in the dimuon-decay channel, at forward rapidity, using the ALICE muon spectrometer. The analysis is based on the data collected in LHC Run2 (2015+2018). R_{AA} is measured as a function of the transverse momentum p_T for the 0–20%, 20–40% and 40–90% centrality intervals, extending the previous measurement up to $p_T = 20$ GeV/c.

Contents

1	Information on the analysis	3
2	Introduction	3
3	Data Sample	3
3.1	Event Selection	3
3.2	Track Selection	5
4	Signal Extraction	5
4.1	Signal and background shapes	5
4.2	Direct fit	7
4.3	Event mixing method	7
4.4	Combination of the systematic tests	14
4.5	Results	14
5	Acceptance efficiency	22
5.1	Acceptance efficiency determination	22
5.2	Run dependence	23
5.3	Realistic input MC distribution: iterative procedure	23
5.4	Results	28
6	Normalization factor	36
6.1	The F_{norm} calculation methods	36
6.1.1	Offline method	36
6.1.2	Online method	37
6.2	Results	37
7	Systematic Uncertainties	38
7.1	Signal extraction	38
7.2	Monte Carlo parametrisation	39
7.3	Tracking efficiency	39
7.4	Trigger efficiency	39
7.5	Matching trigger-tracker track efficiency	40
7.6	pp reference cross sections	40
7.7	Others	40

8 Results	40
9 Conclusion	48
10 Plots for preliminary	49
A Graphs of all systematic tests performed on signal extraction in various p_T bins for various centrality classes	51
B Signal function tail parameters	61
C Systematic uncertainty on the trigger efficiency	64
D Fit parameters for the iteration procedure on tuning of the input MC shapes	72
E Acceptance efficiency and checks	76

1 1 Information on the analysis

2 The analysis note presents currently the result for the 0–20%, 20–40% and 40–90% centrality classes.
3 The results for 0–20% centrality class was approved for QM in 2019. The R_{AA} results for 20–40% and
4 40–90% centrality classes are shown in Fig. 32 and 33 with the corresponding values tabulated in Table
5 18 and 19. The invariant yield results for 20–40% and 40–90% centrality classes are shown in Fig. 29
6 and 30, respectively. Their corresponding values are tabulated in Table 15 and 16. The remaining works
7 for this analysis are the following:

- 8 – systematic uncertainty on MC input to be computed by studying the p_T -y distribution correlation.
9 – systematic uncertainty on intrinsic trigger efficiency to be computed by considering a new effi-
10 ciency map in MC.

11 The differences with respect to previous version (v4) are the following:

- 12 – A typo in Table 9 is updated with the correct number.
13 – Figures for J/ ψ p_T and rapidity differential distribution corrected by $A\varepsilon_0$ and $A\varepsilon_1$ are updated again
14 with the ones for 20–30%, 30–40% and 40–90% centrality class. They can be found in Fig. 16, 17
15 24, 25.
16 – Fit parameters for the iterative procedure in 20–30%, 30–40% and 40–90% centrality bins are
17 updated in Table D.1, D.3, D.5, D.7.
18 – The plots showing the difference between $A \times \varepsilon_1$ and $A \times \varepsilon_0$ are updated in Fig. 19, 20, 22, and 23.
19 – Acceptance and efficiency is estimated for 20–40% and 40–90%. Their numbers are written in
20 Table 10.
21 – Appendix E is added with the links to presentations that discuss the checks on AxEff.

22 2 Introduction

23 Charmonium measurements in Pb–Pb collisions are useful to investigate the properties of the QGP. Two
24 main mechanisms exist to describe the nuclear effects of the hot medium on J/ ψ production in Pb–Pb
25 collisions at low p_T : the J/ ψ suppression by colour screening and the J/ ψ regeneration. At high p_T ,
26 the J/ ψ suppression can be described by colour screening and energy loss mechanisms. The nuclear
27 modification factor measurements, R_{AA} over a wide kinematical range (p_T , y) and as a function of the
28 centrality of the collision are essential to understand the various mechanisms. In this note, the analysis
29 of inclusive J/ ψ production in Pb–Pb collisions at $\sqrt{s_{\text{NN}}} = 5.02$ TeV with the 2015 and 2018 datasets is
30 presented. J/ ψ are studied in their dimuon decay channel in the forward rapidity region ($2.5 < y < 4$)
31 with the muon spectrometer. The J/ ψ invariant yield as a function of p_T is extracted and the R_{AA} is
32 obtained from the pp cross section measured with the 2017 dataset at $\sqrt{s} = 5.02$ TeV.

33 3 Data Sample

34 3.1 Event Selection

35 The analyzed data samples are the Pb–Pb collisions from 2015 and 2018, at $\sqrt{s_{\text{NN}}} = 5.02$ TeV. They
36 consist of 365 runs passing the QA selection . Tab. 1 shows the list of runs analyzed. In this analy-
37 sis, the invariant mass fits are built from events firing either the unlike-sign dimuon trigger CMUL7-
38 B-NOPF-MUFAST (CMUL7) or the like-sign dimuon trigger CMLL7-B-NOPF-MUFAST (CMLL7).

Such selection is less biased than CMUL7 triggered events when one wants to use the event mixing technique¹ to subtract the uncorrelated background. It was checked that in CMLL only events the number of J/ψ is negligible. We also remind that the CMLL7 triggered events were heavily downscaled. For event-mixing purpose, another trigger is used. It is the single low- p_T muon trigger CMSL7-B-NOPPF-MUFAST (CMSL7). Besides, the physics selection (PS) criteria (AliVEvent::kAny) is applied to remove the beam induced background events. For LHC15o, the muon_calo_pass1 AOD229 are used, while for LHC18q and LHC18r, the muon_calo_pass3 AOD225 are used. In 2018 and 2015, those AODs are produced with a new alignment correction.

LHC15o				LHC18q				LHC18r		
244918	245705	246222	246859	295584	295829	296197	296550	296690	296975	297441
244980	245729	246225	246864	295585	295831	296198	296551	296691	296976	297442
244982	245731	246272	246865	295586	295854	296241	296552	296694	296977	297446
244983	245738	246275	246867	295587	295855	296242	296553	296749	296979	297450
245064	245752	246276	246871	295588	295856	296243	296615	296750	297029	297451
245066	245759	246390	246930	295589	295859	296244	296616	296752	297031	297452
245068	245766	246391	246937	295612	295860	296246	296618	296781	297035	297479
245145	245775	246392	246942	295615	295861	296247	296619	296784	297085	297481
245146	245785	246424	246945	295665	295863	296269	296622	296785	297117	297483
245151	245793	246428	246948	295666	295881	296270	296623	296786	297118	297512
245152	245829	246431	246949	295667	295908	296273		296787	297119	297537
245231	245831	246433	246980	295668	295909	296279		296791	297123	297540
245232	245833	246434	246982	295671	295910	296280		296793	297124	297541
245233	245949	246487	246984	295673	295913	296303		296794	297128	297542
245253	245952	246488	246989	295675	295936	296304		296799	297129	297544
245259	245954	246493	246991	295676	295937	296307		296836	297132	297558
245343	245963	246495	246994	295677	295941	296309		296838	297133	297588
245345	245996	246675		295714	295942	296312		296839	297193	297590
245346	246001	246676		295716	295943	296376		296848	297194	297595
245347	246003	246750		295717	295945	296377		296849	297196	
245353	246012	246751		295718	295947	296378		296850	297218	
245401	246036	246755		295719	296061	296379		296851	297219	
245407	246037	246757		295723	296062	296380		296852	297221	
245409	246042	246758		295725	296063	296381		296890	297222	
245410	246048	246759		295753	296065	296383		296894	297278	
245446	246049	246760		295754	296066	296414		296899	297310	
245450	246053	246763		295755	296068	296419		296900	297312	
245496	246087	246765		295758	296123	296420		296903	297315	
245501	246089	246804		295759	296128	296423		296930	297317	
245504	246113	246805		295762	296132	296424		296931	297363	
245505	246115	246806		295763	296133	296433		296932	297366	
245507	246148	246807		295786	296134	296472		296934	297367	
245535	246151	246808		295788	296135	296509		296935	297372	
245540	246152	246809		295791	296142	296510		296938	297379	
245542	246153	246844		295816	296143	296511		296941	297380	
245543	246178	246845		295818	296191	296514		296966	297405	
245554	246181	246846		295819	296192	296516		296967	297408	
245683	246182	246847		295822	296194	296547		296968	297413	
245692	246217	246851		295825	296195	296548		296969	297414	
245700	246220	246855		295826	296196	296549		296971	297415	
CMUL7 triggered events before PS				CMUL7 triggered events before PS				CMUL7 triggered events before PS		
1.269×10^8				1.112×10^8				1.634×10^8		
CMUL7 triggered events after PS				CMUL7 triggered events after PS				CMUL7 triggered events after PS		
1.266×10^8				1.108×10^8				1.630×10^8		

Table 1: List of QA checked runs in muon_calo_pass1 for LHC15o and muon_calo_pass3 for LHC18q and LHC18r, along with the total CMUL7 triggered events before and after physics selection.

¹For more detail of the event mixing technique, see section 4.3.

47 **3.2 Track Selection**

48 The following track selections are applied:

- 49 – $-4 < \eta_\mu < -2.5$ to reject tracks at the edges of the Muon Spectrometer acceptance;
- 50 – $2 < \theta_{abs} < 10^\circ$, where θ_{abs} is the angle between the beam axis and the track at the end of the
51 absorber, in order to exclude the tracks crossing the thicker part of the absorber;
- 52 – tracking track matches a trigger track, whose p_T is required to be above the trigger low p_T^{trig}
53 threshold, with $p_T^{trig} \sim 1$ GeV/c. It reduces the background from π and K decays.
- 54 – $p \times \text{DCA}$ cut within 6σ is applied, where $p \times \text{DCA}$ is the product of the track momentum with the
55 Distance of Closest Approach (DCA). The DCA is the distance in the transverse plane between
56 the interaction point and the extrapolated muon track. This cut removes the tracks which do not
57 originate from the interaction point.

58 The selected muons are combined to form muon pairs. Further selections are applied on the muon pairs
59 (dimuons):

- 60 – the two muons have opposite charges (OS dimuon),
- 61 – the dimuon satisfies the following rapidity cut and p_T cut: $2.5 < y < 4.0$, $p_T < 20$ GeV/c.

62 **4 Signal Extraction**

63 The signal extraction is first performed with a direct fit of the OS dimuon invariant mass spectra with
64 a sum of two functions describing the signal shapes (J/ψ and $\psi(2S)$) and one function describing the
65 background shape. The event mixing method is also used to estimate the uncorrelated background. In
66 that case, the subtracted invariant mass spectra is then fitted by functions describing the signal shape and
67 the residual background.

68 Various fitting tests are performed to extract the J/ψ signal and the associated systematic uncertainty.
69 The tests are done by multiple choices of signal functions, background functions, and fitting ranges, as
70 explained below.

71 In all cases, a likelihood approach is used to fit the spectra. The signal extraction is performed in several
72 p_T and centrality bins.

73 **4.1 Signal and background shapes**

74 – Signal shape:

75 The J/ψ peak was fitted with either [1]:

- 77 – an extended Crystal Ball (CB2),
78 – a function adapted from the one of the NA60 experiment (NA60).

79 The formulas of the two signal functions are defined in Appendix B. The CB2 function connects
80 a Gaussian core with a power-law tail at low mass to account for energy loss fluctuations and
81 radiative decays. An additional power-law tail at high mass is added to account for alignment
82 and calibration biases. The CB2 function is described by 7 parameters. The NA60 function is a
83 variable width Gaussian described by 11 parameters. Tails of each function are fixed (see below).

The J/ψ mass pole and width are left free during the fitting procedure. The mass of the $\psi(2S)$ is bound to the J/ψ one by adding the mass difference from the PDG between the two states. The ratio of $\psi(2S)$ over J/ψ width has been fixed to 1.01 according to the study performed on the large statistics sample of pp data at $\sqrt{s} = 13$ TeV [2], in which the $\psi(2S)$ width could be let free during the fit of the integrated (over p_T and y) spectrum. The effect of varying the $\psi(2S)$ width on the measured number of J/ψ was evaluated with a single fit. Indeed, similarly to the 13 TeV analysis, the $\psi(2S)$ over J/ψ width ratio was varied from 1.01 to 1.05. The effect on the number of J/ψ was found to be of 0.2 permil on the integrated p_T/y /centrality spectra. The variation of the $\psi(2S)$ width was therefore neglected in the signal extraction systematic studies.

- Background shape:

For the direct fit, the background was fitted with either:

- A ratio of second order polynomial over a third order polynomial² (POL2/POL3),
- A variable width Gaussian (VWG), with 5 free parameters.

The formula of the VWG is the same as the one in [1].

In the case of the event mixing procedure, the subtracted mass spectra was fitted with:

- A sum of two exponential functions³ describing the residual background.

- Fitting ranges:

Two invariant mass fitting ranges have been considered for the global fitting of the signal and background functions:

- $2.2 < M < 4.5 \text{ GeV}/c^2$.
- $2.4 < M < 4.7 \text{ GeV}/c^2$.

- Signal tails:

Several hypotheses have been considered for tuning the CB2 and NA60 function tail parameters with embedding MC simulations and data, as a function of p_T . Two sets of tails have been considered:

- tails obtained by fitting the hadronic J/ψ production in embedding MC simulations using the Geant3 transport code (MC production LHC19a2 for LHC18q and LHC18r, MC productions LHC16e2 and LHC16e2_plus for LHC15o, see Section 5 for more details). The mass spectra were merged after weighting them period per period, by the number of CMUL7 events in data over the number of CINT7 events in the MC. Finally, the tail values are given in Appendix B.
- tails obtained by fitting the J/ψ production in pp data at $\sqrt{s} = 13$ TeV [2] (for CB2 function only).

Note that the reconstructed J/ψ mass spectra in various p_T bins are also obtained by merging the embedding MC productions LHC19a2, LHC16e2 and LHC16e2_plus. To obtain the tail parameters in each p_T ranges, we used the CB2 and NA60 functions to fit the integrated in centrality mass spectra.

²The formula of this polynomial ratio is expressed as $f_{\frac{\text{POL2}}{\text{POL3}}}(x; p_0, \dots, p_6) = p_0 \cdot \frac{1 + p_1 x + p_2 x^2}{p_3 + p_4 x + p_5 x^2 + p_6 x^3}$

³The formula of the two exponential sum is expressed as $f_{\text{exp}}(x; p_0, \dots, p_3) = p_0 e^{-x/p_1} + p_2 e^{-x/p_3}$

124 **4.2 Direct fit**

125 Figure 1 to 6 show examples of the OS dimuon invariant mass distribution for all the p_T ranges and
126 in 0–20%, 20–40% and 40–90% centrality intervals. The spectra are fitted with the sum of two signal
127 shapes describing the J/ ψ and $\psi(2S)$ and a background shape to describe the background. The shapes
128 used are indicated in the plots.

129 **4.3 Event mixing method**

130 Since there is a large background contribution around the J/ ψ mass region in Pb-Pb collisions, the mixed-
131 event method is applied to subtract the uncorrelated OS dimuon background. The idea of this method is
132 to mix one muon track in one event with another muon track with opposite charge in another event, in
133 order to build an OS muon pair which is not related to the decay of a particle. Those muon tracks are
134 selected from CMSL triggered events as it was shown in [3] that this trigger provides a better description
135 of the uncorrelated background for the like-sign pairs. A normalization factor is needed to normalize the
136 mixed dimuon background events to the raw mass spectra. The normalization factor is given by:

$$F = \frac{\int_{m_1}^{m_2} 2R_{\text{acc}} \sqrt{N_{\text{real}}^{++} N_{\text{real}}^{--}} dm}{\int_{m_1}^{m_2} N_{\text{mixed}}^{+-} dm} \quad (1)$$

137 where m is the dimuon mass. The upper and lower bounds are $m_1 = 2$ and $m_2 = 8$ GeV/ c^2 . The
138 acceptance factor R_{acc} is defined as:

$$R_{\text{acc}} = \frac{N_{\text{mixed}}^{+-}}{2\sqrt{N_{\text{mixed}}^{++} N_{\text{mixed}}^{--}}} \quad (2)$$

139 The other variables in Eq. 1 and Eq. 2 are defined such as:

140 – $N_{\text{mixed}}^{++}, N_{\text{mixed}}^{+-}, N_{\text{mixed}}^{--}$ are the number of dimuons obtained from the event mixing sample from the
141 CMSL triggered events. The superscripts specify the charges of the two muons.

142

143 – $N_{\text{real}}^{++}, N_{\text{real}}^{+-}, N_{\text{real}}^{--}$ are the number of dimuons obtained from the raw data from CMUL or CMLL
144 triggered events. The superscripts specify the charges of the two muons.

145

146 Since the CMLL trigger is downscaled, the OS and LS raw data dimuon pairs from CMLL&!CMUL
147 triggered events are weighted by the inverse of the downscaling factor.

148

149 Fig. 7 shows the mixed muon pair mass spectra of the acceptance factor for 0–10% centrality class of the
150 2018 and 2015 data samples in left and right panels, respectively. For the 2015 and 2018 data samples,
151 their R_{acc} values for $2 < m_{\mu\mu} < 8$ GeV/ c^2 approximate one as expected.

152 Table 2 tabulates the normalization factor (F_{2018} and F_{2015}) for the mixed dimuon event normalizing to
153 the raw mass spectra of the 2018 and 2015 Pb-Pb data samples, respectively.

154 After subtraction of the uncorrelated background by the event-mixing technique, the residual mass spec-
155 tra are fitted with a sum of two functions, a signal shape and a background shape. Note that only a sum
156 of two exponential functions is used to describe the residual background. Figure 9 shows an example of
157 the residual mass spectra fit for few p_T intervals.

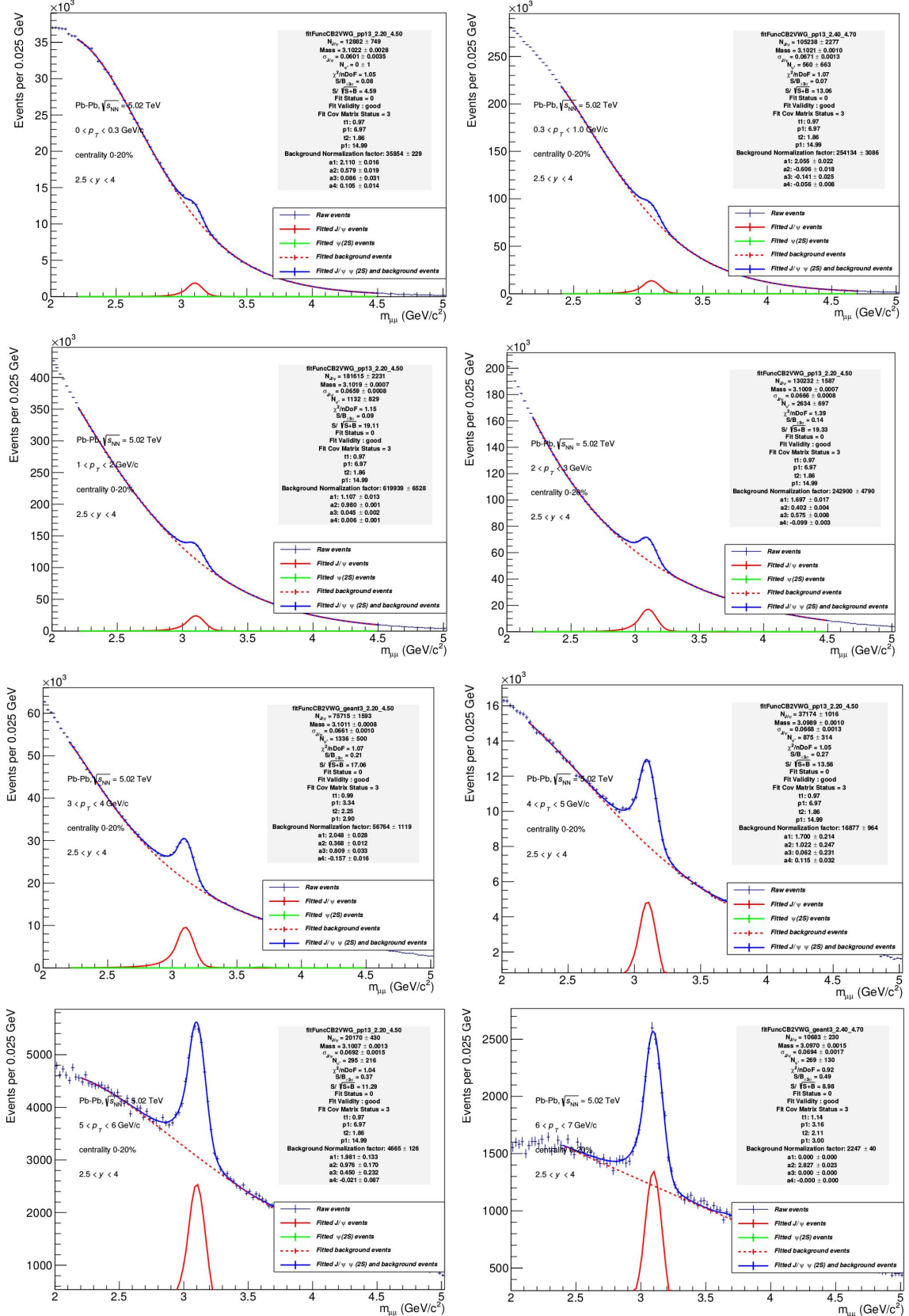


Fig. 1: Example of J/ψ dimuon OS invariant mass spectra fits in 0–20% centrality bins and in several p_T ranges, from 0 to 7 GeV/c .

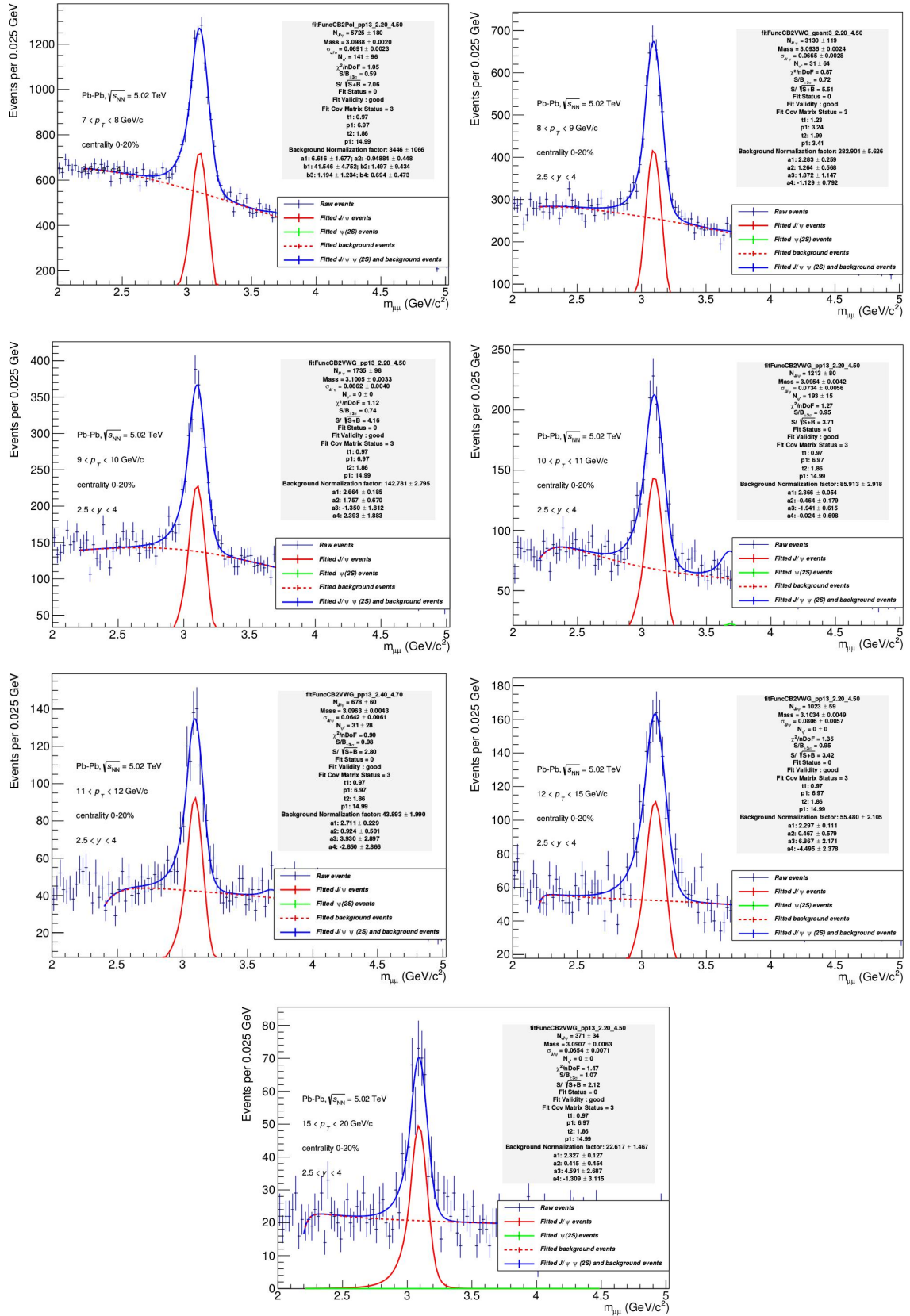


Fig. 2: Example of J/ψ dimuon OS invariant mass spectra fits in 0–20% centrality bins and in several p_T ranges, from 7 to 20 GeV/c .

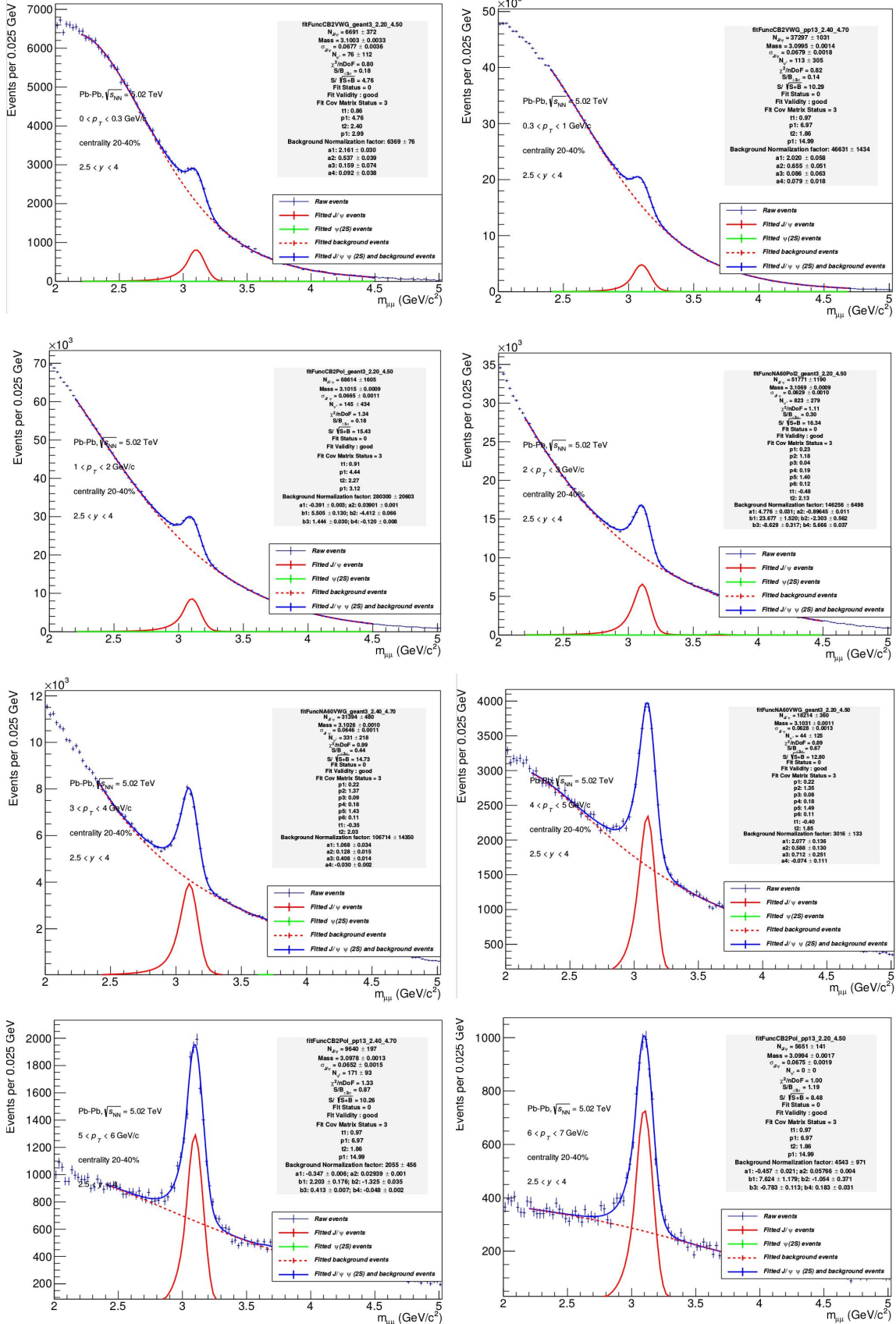


Fig. 3: Example of J/ψ dimuon OS invariant mass spectra fits in 20–40% centrality bins and in several p_T ranges, from 0 to 7 GeV/c .

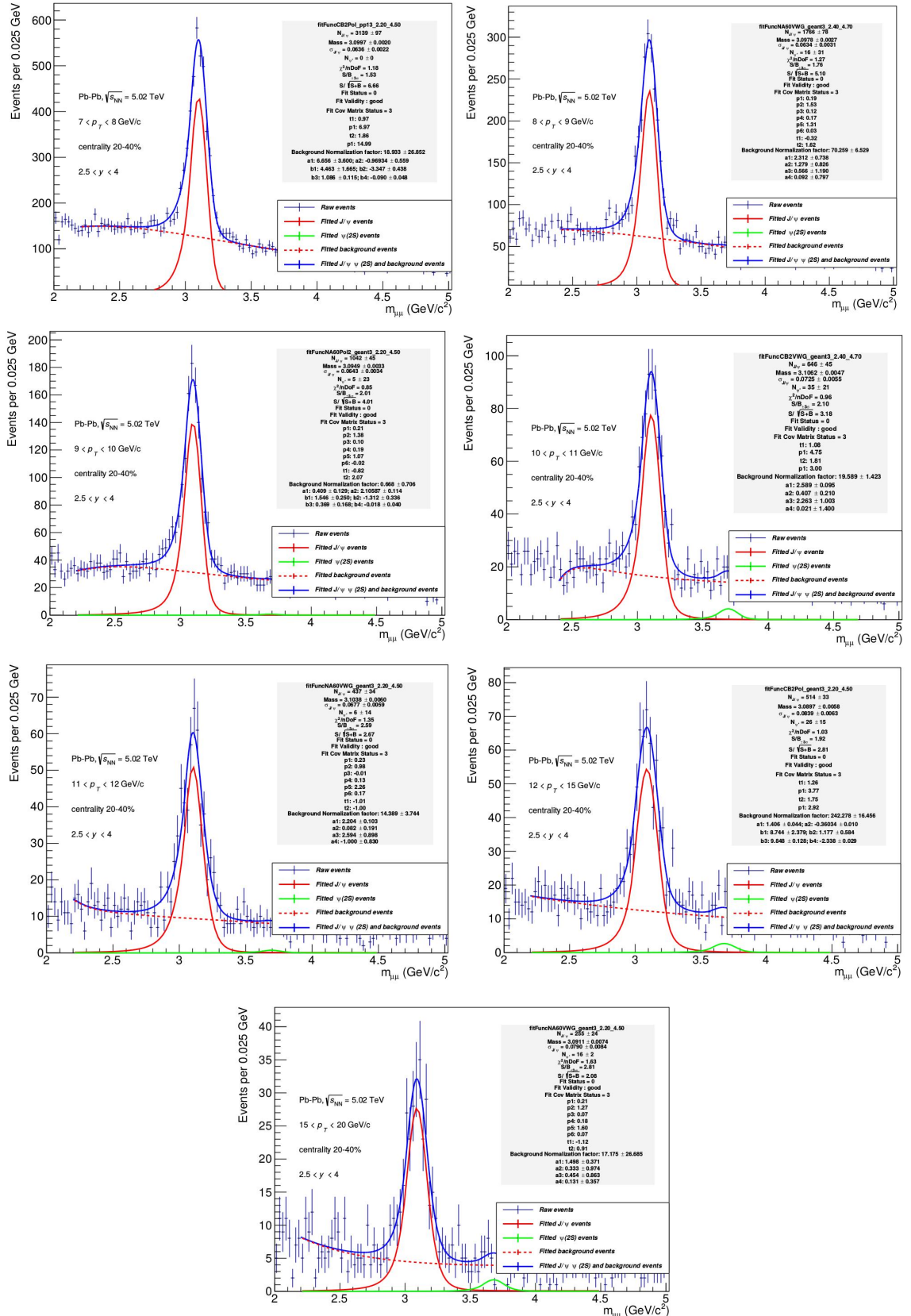


Fig. 4: Example of J/ψ dimuon OS invariant mass spectra fits in 20–40% centrality bins and in several p_T ranges, from 7 to 20 GeV/c .

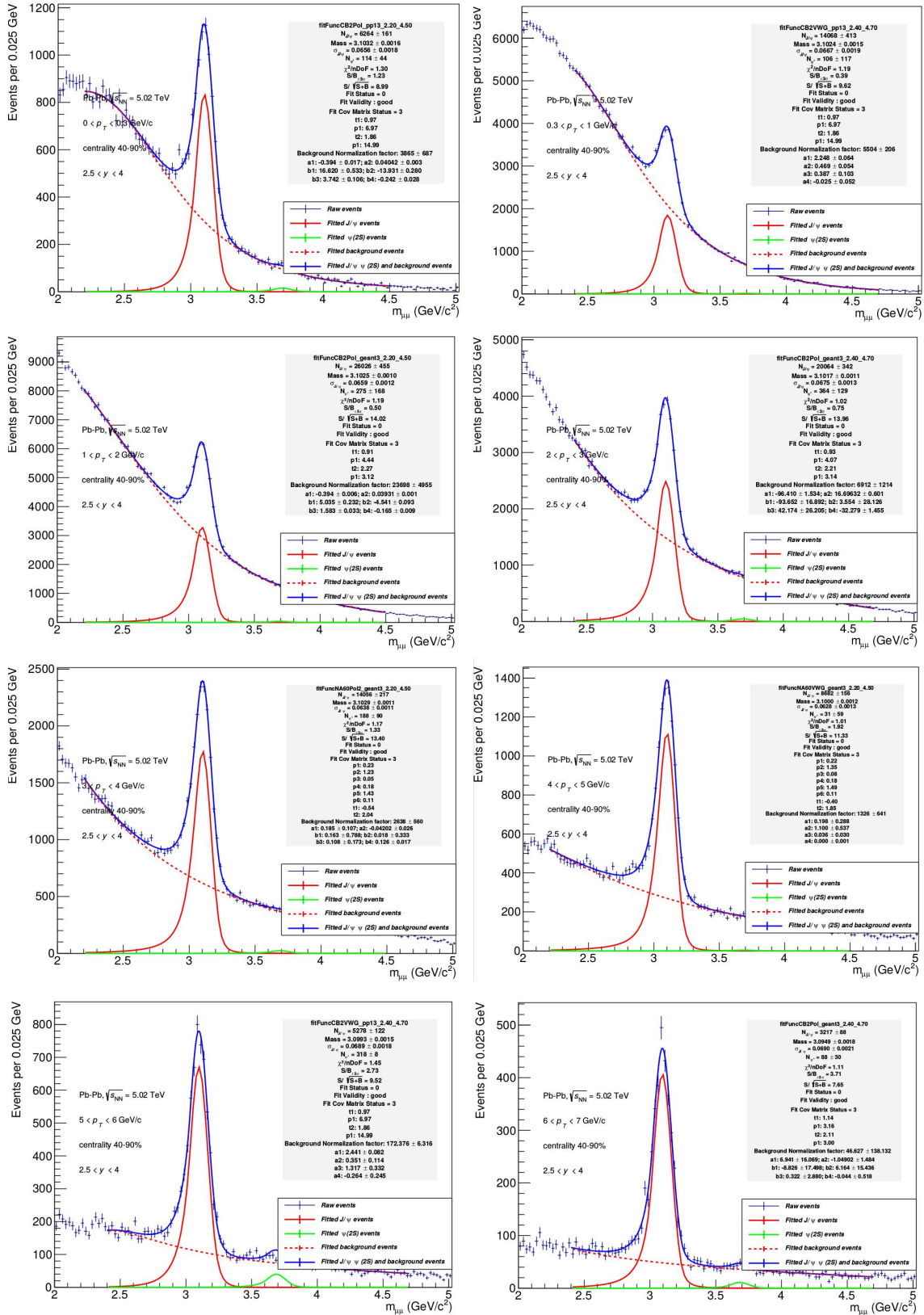


Fig. 5: Example of J/ψ dimuon OS invariant mass spectra fits in 40–90% centrality bins and in several p_T ranges, from 0 to 7 GeV/c .

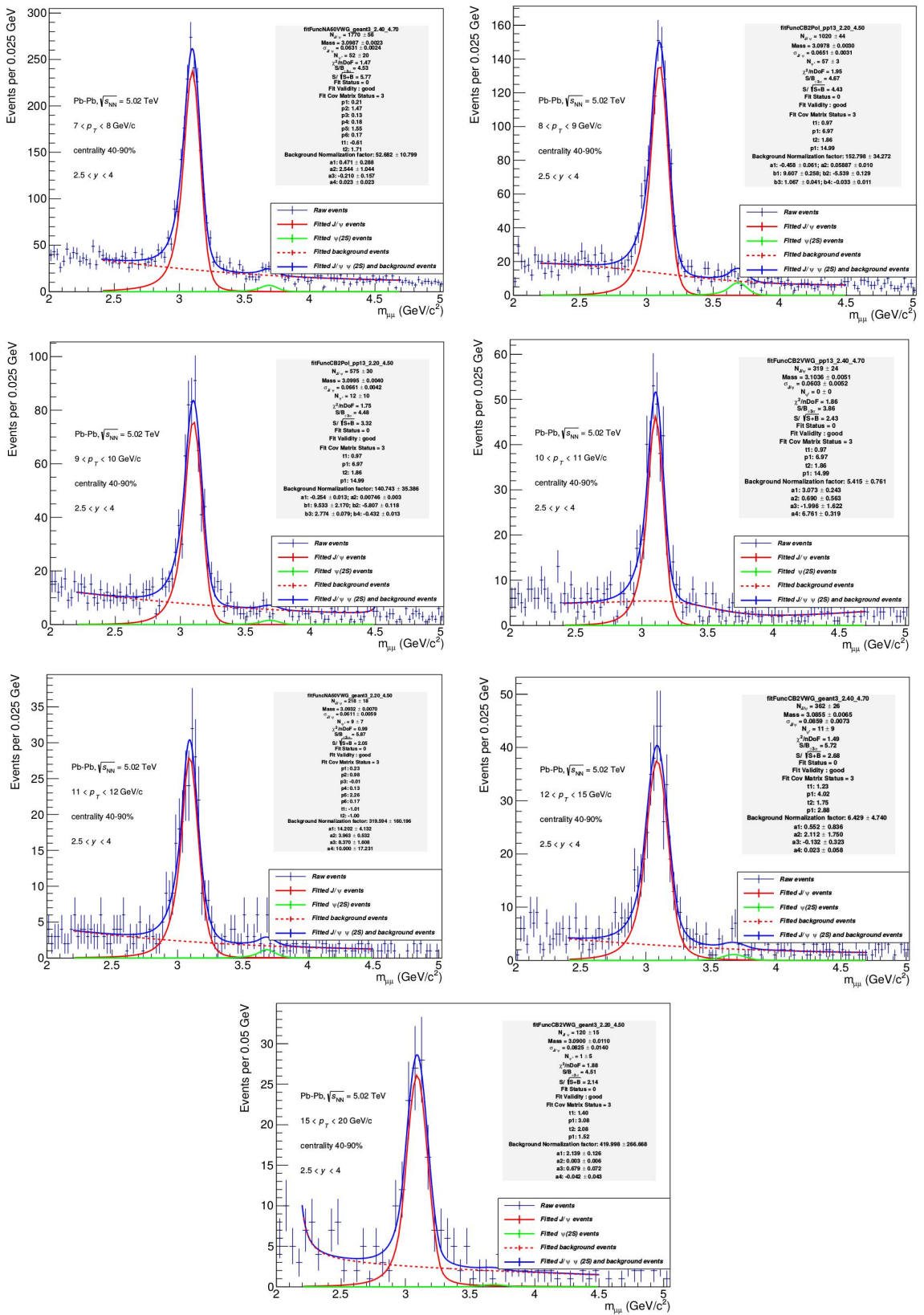


Fig. 6: Example of J/ψ dimuon OS invariant mass spectra fits in 40–90% centrality bins and in several p_T ranges, from 7 to 20 GeV/c .

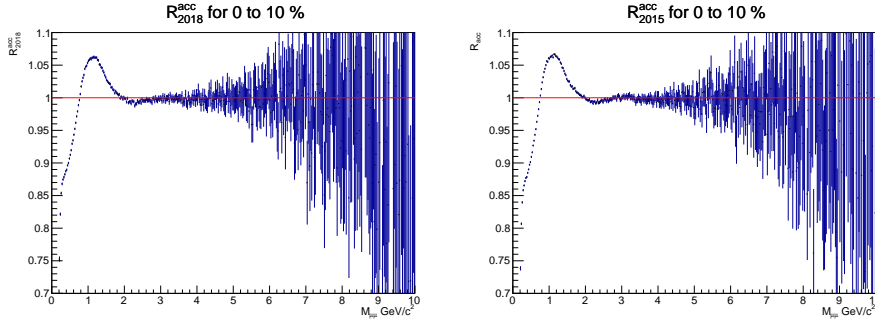


Fig. 7: The acceptance factor R_{acc} obtained with the mixed muon pair events for 0–10 % centrality class in the 2018 (left panel) and 2015 (right panel) data samples.

centrality	0–10%	10–20%	20–30%	30–40%	40–50%	50–60%	60–70%	70–80%	80–90%
F_{2018}	0.584	0.449	0.325	0.222	0.14	0.08	0.043	0.02	0.008
F_{2015}	0.199	0.153	0.111	0.075	0.047	0.027	0.015	0.0065	0.0028

Table 2: Summary of the normalization factor, F_{2018} and F_{2015} for the mixed dimuon events normalizing to raw mass spectra of 2018 and 2015 Pb-Pb data samples, respectively.

158 4.4 Combination of the systematic tests

159 In total, 18 fits are performed for the systematic study of signal extraction.

160 For each bin in p_T and centrality, the combination of all the signal shapes, background shapes, fitting
161 ranges and tail parameters have been considered. To be taken into account in the final results, the χ^2 of
162 the global fit normalized to the corresponding number of degrees of freedom of each test must be smaller
163 than 3, the fit status must be good (i.e. : the fit has converged) and the status of the covariant matrix
164 must be 3. The final number of J/ψ is calculated as the weighted mean of all the tests. The systematic
165 uncertainty is defined as the weighted RMS of the results. The results have been weighted such that fits
166 with pp data tail parameters have the same weight as tests with MC tail parameters. Figure 10, 11, and
167 12 shows the raw number of J/ψ versus the 18 systematic tests for $0 \leq p_T < 20$ GeV/ c , for 0–20 %,
168 20–40%, and 40–90% centrality classes respectively, as well as the J/ψ width, mass and χ^2/NDF of the
169 fits. Furthermore, the ones versus the 18 systematic test for various p_T bins are shown in appendix A.

170 4.5 Results

171 Table 3, 4 and 5 show the raw number of J/ψ in p_T intervals in 0–20%, 20–40%, and 40–90% centrality
172 classes, respectively.

173 Figure 13 shows the $J/\psi dN/dp_T$ as a function of p_T in 0–20%, 20–40%, and 40–90% centrality classes.
174 The results are also reported in Table 6, 7 and 8.

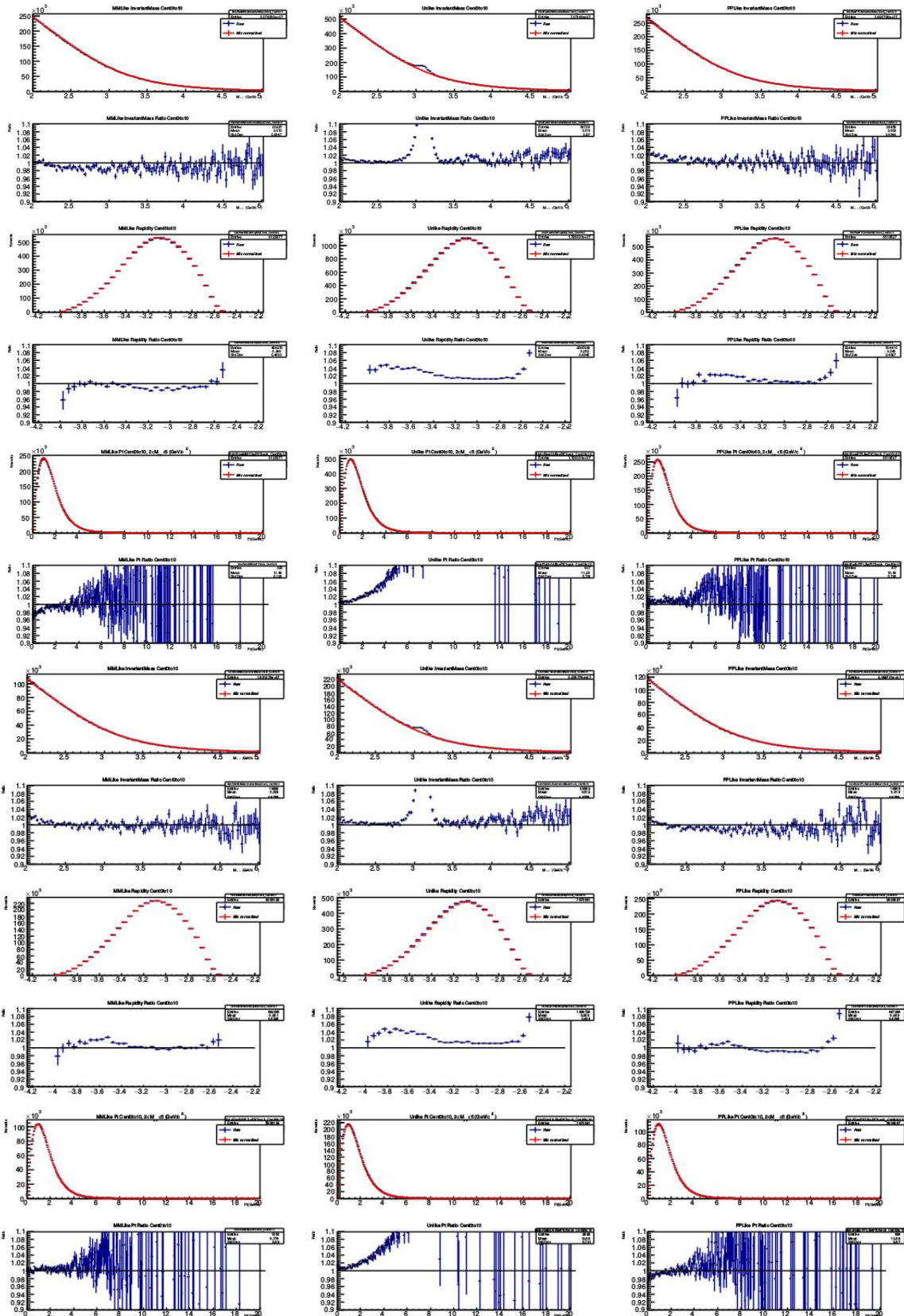


Fig. 8: Control plots with the mass, p_T and rapidity spectra of the raw events and the mixed muon pair events for 0–10 % centrality class in the 2018 (top panel) and 2015 (bottom panel) data samples.

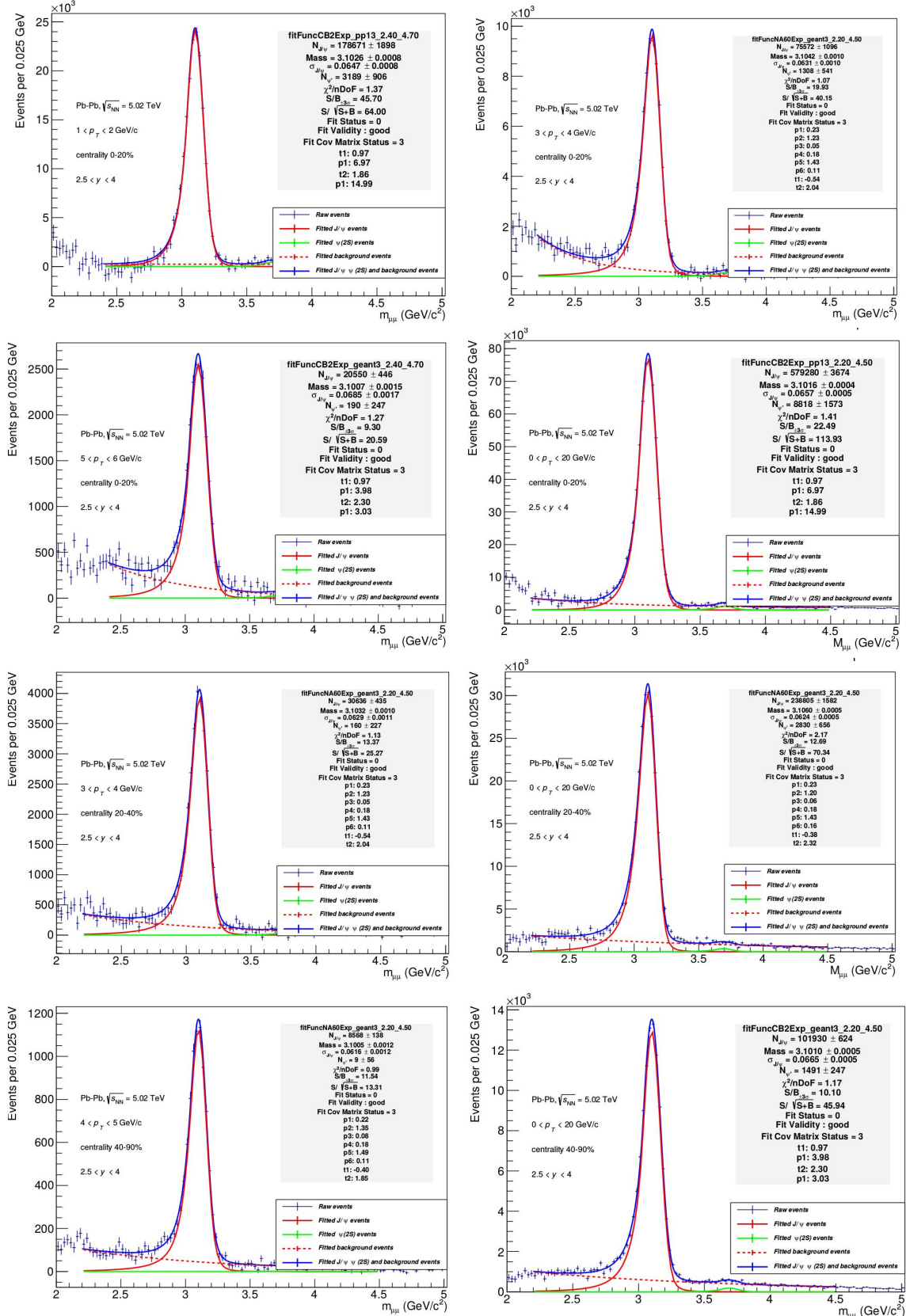


Fig. 9: Example of J/ψ dimuon OS invariant mass spectra event mixing fits in several p_T and centrality ranges.

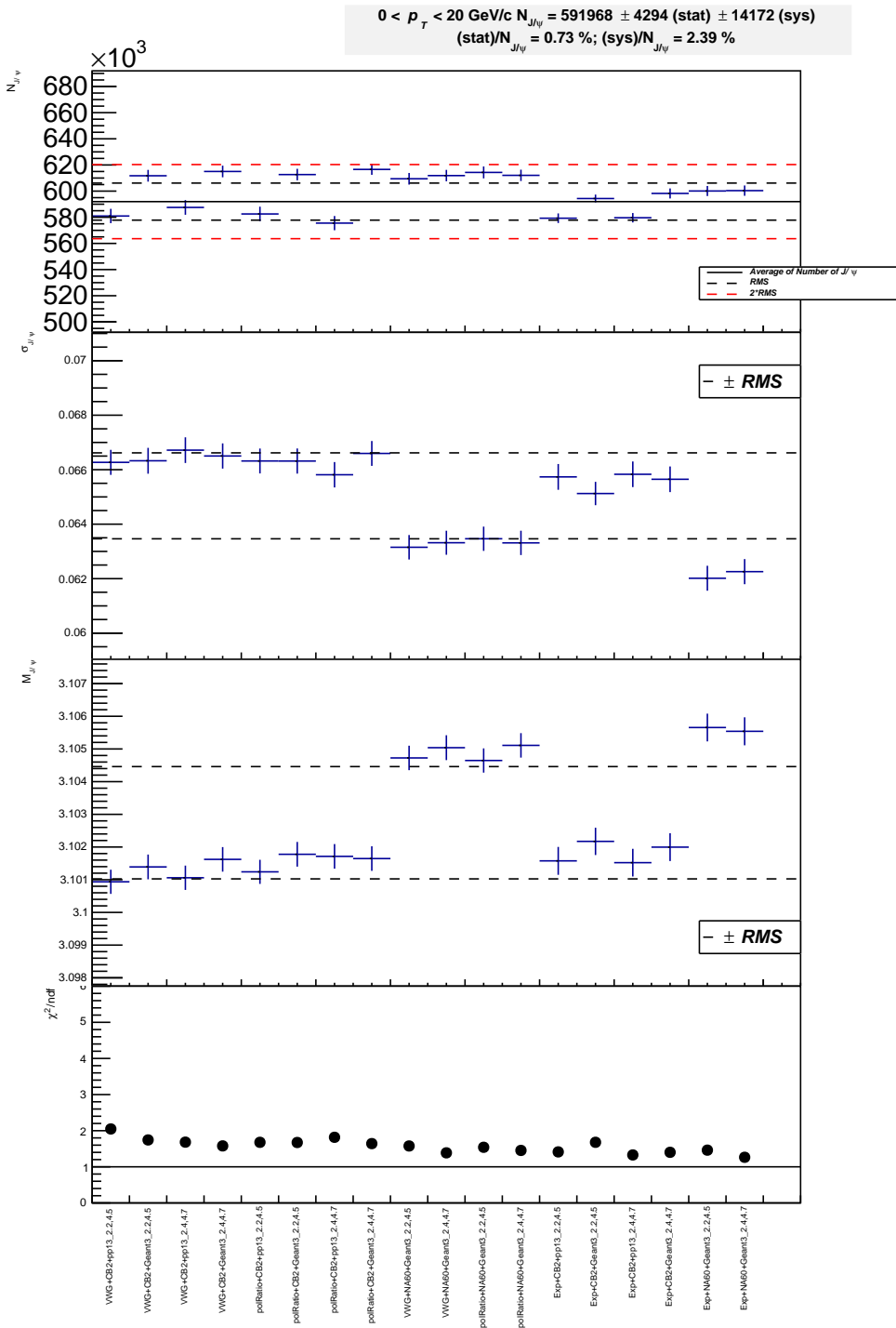


Fig. 10: Raw number of J/ψ , mass and sigma versus systematic tests for $0 \leq p_T < 20 \text{ GeV}/c$ and for 0–20 % centrality class, as well as fit χ^2/NDF versus systematic tests.

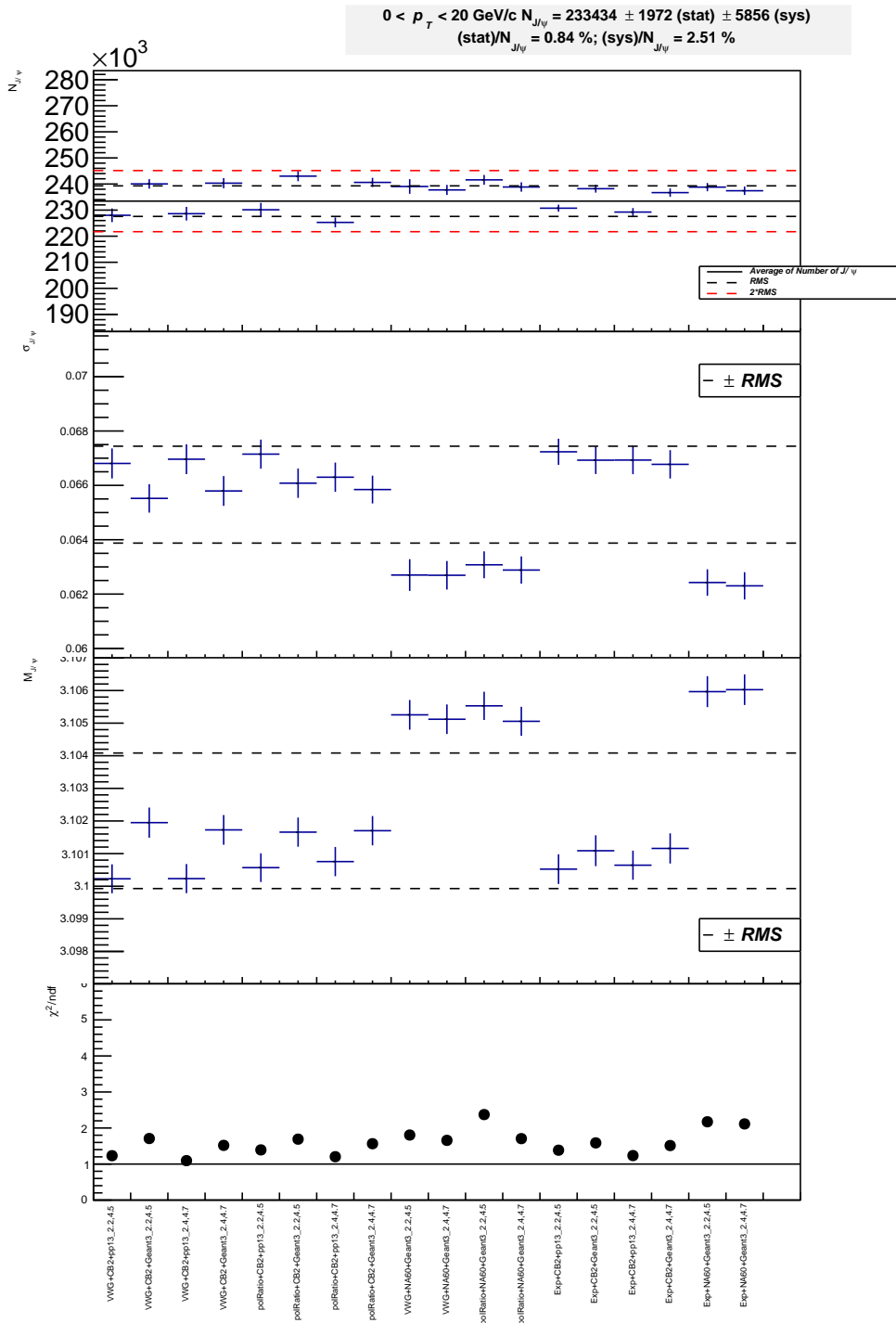


Fig. 11: Raw number of J/ψ , mass and sigma versus systematic tests for $0 \leq p_T < 20 \text{ GeV}/c$ and for 20–40 % centrality class, as well as fit χ^2/NDF versus systematic tests.

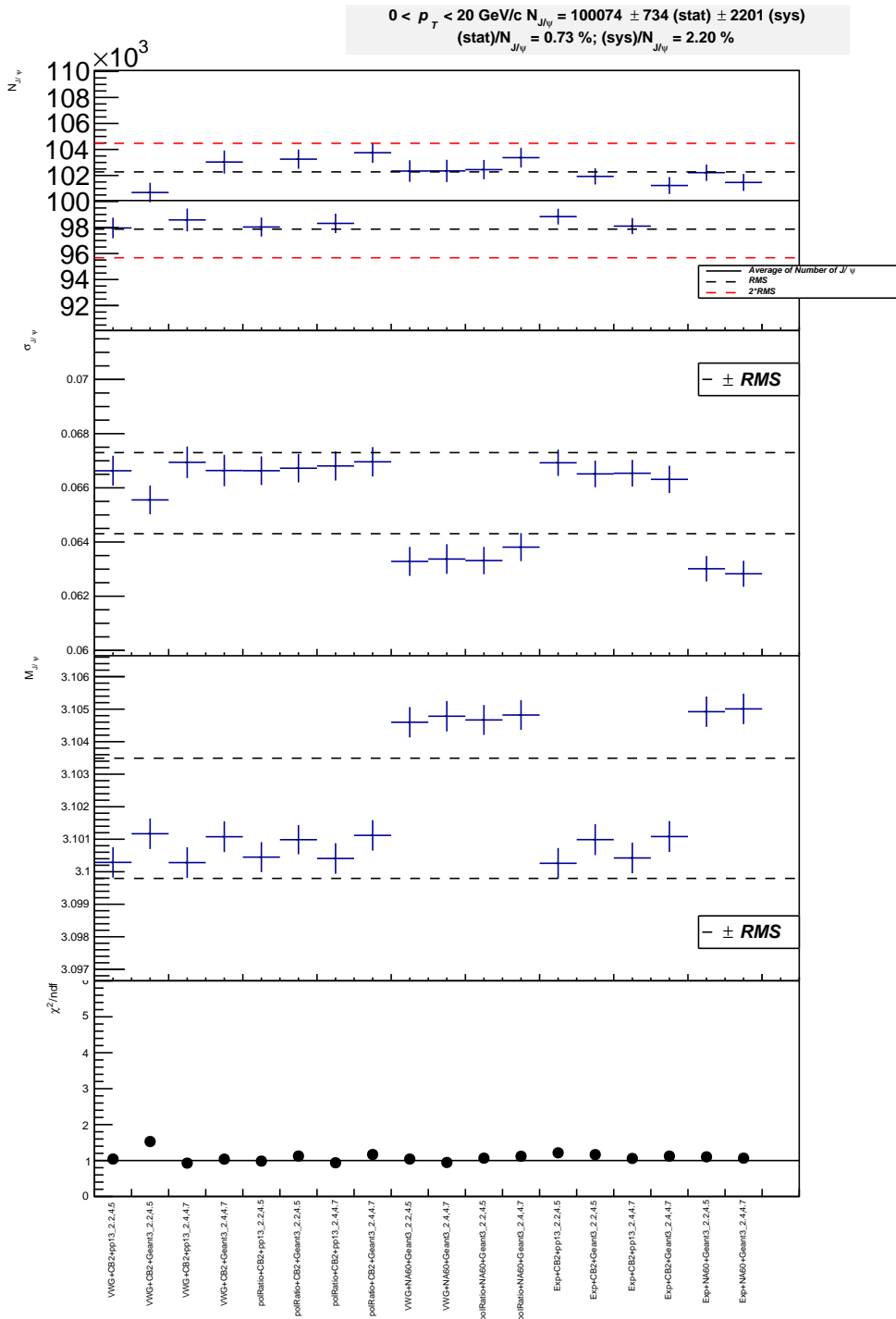


Fig. 12: Raw number of J/ψ , mass and sigma versus systematic tests for $0 \leq p_T < 20 \text{ GeV}/c$ and for 40–90 % centrality class, as well as fit χ^2/NDF versus systematic tests.

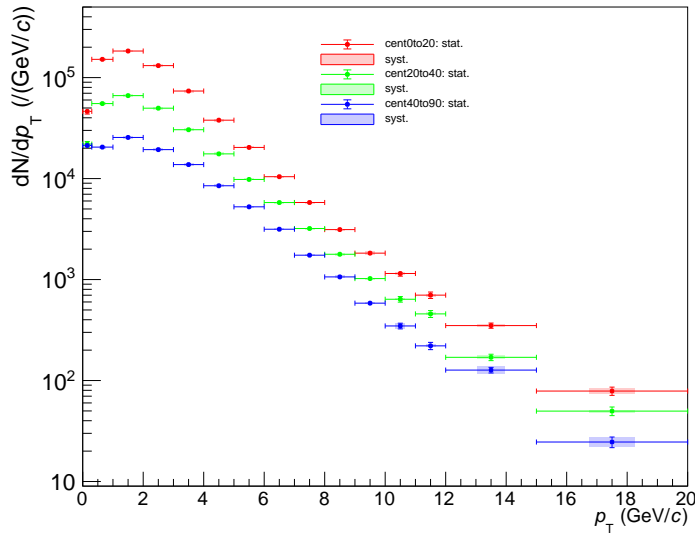
p_T (GeV/c)	$N_{\text{raw}}^{J/\psi} \pm \text{stat}(\%) \pm \text{syst}(\%)$
centrality 0 - 20%	
0–0.3	13890 \pm 824 (5.9) \pm 552 (4.0)
0.3–1	106158 \pm 2240 (2.1) \pm 2985 (2.8)
1–2	183306 \pm 2389 (1.3) \pm 3277 (1.8)
2–3	131450 \pm 1602 (1.2) \pm 3950 (3.0)
3–4	73631 \pm 1340 (1.8) \pm 2069 (2.8)
4–5	37874 \pm 764 (2.0) \pm 1064 (2.8)
5–6	20346 \pm 432 (2.1) \pm 329 (1.6)
6–7	10440 \pm 260 (2.5) \pm 188 (1.8)
7–8	5796 \pm 179 (3.1) \pm 99 (1.7)
8–9	3125 \pm 121 (3.9) \pm 46 (1.5)
9–10	1826 \pm 92 (5.0) \pm 70 (3.9)
10–11	1148 \pm 68 (5.9) \pm 34 (2.9)
11–12	701 \pm 51 (7.3) \pm 23 (3.3)
12–15	1050 \pm 63 (6.0) \pm 30 (2.9)
15–20	393 \pm 37 (9.4) \pm 23 (5.8)
0–20 (sum of p_T bins)	591137 \pm 4803 (0.7)
0–20 (fit)	591968 \pm 4294 (0.7) \pm 14172 (2.4)

Table 3: Raw number of J/ψ in p_T intervals and in 0–20% centrality class.

p_T (GeV/c)	$N_{\text{raw}}^{J/\psi} \pm \text{stat}(\%) \pm \text{syst}(\%)$
centrality 20 - 40%	
0–0.3	6584 \pm 401 (6.1) \pm 206 (3.1)
0.3–1	38709 \pm 984 (2.5) \pm 1052 (2.7)
1–2	66303 \pm 1241 (1.9) \pm 1748 (2.6)
2–3	49791 \pm 972 (2.0) \pm 1272 (2.6)
3–4	30467 \pm 491 (1.6) \pm 892 (2.9)
4–5	17566 \pm 306 (1.7) \pm 447 (2.5)
5–6	9805 \pm 206 (2.1) \pm 189 (1.9)
6–7	5789 \pm 140 (2.4) \pm 112 (1.9)
7–8	3203 \pm 97 (3.0) \pm 67 (2.1)
8–9	1781 \pm 70 (4.0) \pm 49 (2.8)
9–10	1023 \pm 54 (5.3) \pm 21 (2.1)
10–11	638 \pm 41 (6.4) \pm 13 (2.0)
11–12	457 \pm 36 (7.9) \pm 14 (3.0)
12–15	509 \pm 37 (7.3) \pm 23 (4.5)
15–20	249 \pm 24 (9.8) \pm 6 (2.4)
0–20 (sum of p_T bins)	232874 \pm 2008 (0.9)
0–20 (fit)	233434 \pm 1972 (0.8) \pm 5856 (2.5)

Table 4: Raw number of J/ψ in p_T intervals and in 20–40% centrality class.

p_T (GeV/c)	$N_{\text{raw}}^{J/\psi} \pm \text{stat}(\%) \pm \text{syst}(\%)$
centrality 40 - 90%	
0–0.3	$6379 \pm 156 (2.4) \pm 139 (2.2)$
0.3–1	$14349 \pm 389 (2.7) \pm 416 (2.9)$
1–2	$25545 \pm 436 (1.7) \pm 609 (2.4)$
2–3	$19354 \pm 321 (1.7) \pm 458 (2.4)$
3–4	$13759 \pm 215 (1.6) \pm 438 (3.2)$
4–5	$8491 \pm 148 (1.7) \pm 221 (2.6)$
5–6	$5252 \pm 111 (2.1) \pm 95 (1.8)$
6–7	$3151 \pm 78 (2.5) \pm 56 (1.8)$
7–8	$1743 \pm 55 (3.2) \pm 41 (2.4)$
8–9	$1062 \pm 42 (3.9) \pm 35 (3.3)$
9–10	$584 \pm 31 (5.3) \pm 9 (1.6)$
10–11	$347 \pm 23 (6.5) \pm 21 (6.0)$
11–12	$220 \pm 18 (8.3) \pm 6 (2.7)$
12–15	$381 \pm 24 (6.3) \pm 31 (8.1)$
15–20	$123 \pm 15 (12.1) \pm 13 (10.7)$
0–20 (sum of p_T bins)	$100740 \pm 750 (0.7)$
0–20 (fit)	$100074 \pm 734 (0.7) \pm 2201 (2.2)$

Table 5: Raw number of J/ψ in p_T intervals and in 40–90% centrality class.**Fig. 13:** J/ψ dN/dp_T versus p_T for several centrality classes.

p_T (GeV/c)	dN/d p_T ± stat(%) ± syst(%)
centrality 0 - 20%	
0–0.3	46299 ± 2747 (5.9) ± 1840 (4.0)
0.3–1	151654 ± 3200 (2.1) ± 4264 (2.8)
1–2	183306 ± 2389 (1.3) ± 3277 (1.8)
2–3	131450 ± 1602 (1.2) ± 3950 (3.0)
3–4	73631 ± 1340 (1.8) ± 2069 (2.8)
4–5	37874 ± 764 (2.0) ± 1064 (2.8)
5–6	20346 ± 432 (2.1) ± 329 (1.6)
6–7	10440 ± 260 (2.5) ± 188 (1.8)
7–8	5796 ± 179 (3.1) ± 99 (1.7)
8–9	3125 ± 121 (3.9) ± 46 (1.5)
9–10	1826 ± 92 (5.0) ± 70 (3.9)
10–11	1148 ± 68 (5.9) ± 34 (2.9)
11–12	701 ± 51 (7.3) ± 23 (3.3)
12–15	350 ± 21 (6.0) ± 10 (2.9)
15–20	79 ± 7 (9.4) ± 5 (5.8)

Table 6: J/ψ dN/d p_T values in 0–20% centrality class.

p_T (GeV/c)	dN/d p_T ± stat(%) ± syst(%)
centrality 20 - 40%	
0–0.3	21947 ± 1336.41 (6.1) ± 686 (3.1)
0.3–1	55298 ± 1405 (2.5) ± 1503 (2.7)
1–2	66303 ± 1241 (1.9) ± 1748 (2.6)
2–3	49791 ± 972 (2.0) ± 1272 (2.6)
3–4	30467 ± 491 (1.6) ± 892 (2.9)
4–5	17566 ± 306 (1.7) ± 447 (2.5)
5–6	9805 ± 206 (2.1) ± 189 (1.9)
6–7	5789 ± 140 (2.4) ± 112 (1.9)
7–8	3203 ± 97 (3.0) ± 67 (2.1)
8–9	1781 ± 70 (4.0) ± 49 (2.8)
9–10	1023 ± 54 (5.3) ± 21 (2.1)
10–11	638 ± 41 (6.4) ± 13 (2.0)
11–12	457 ± 36 (7.9) ± 14 (3.0)
12–15	170 ± 12 (7.3) ± 8 (4.5)
15–20	50 ± 5 (9.8) ± 1 (2.4)

Table 7: J/ψ dN/d p_T values in 20–40% centrality class.

175 5 Acceptance efficiency

176 5.1 Acceptance efficiency determination

177 The acceptance and efficiency ($A \times \epsilon$) of the detector was estimated by using LHC16e2, LHC16e2_plus
 178 and LHC19a2, the official MonteCarlo (MC) simulations based on the embedding technique. The MC
 179 J/ψ is embedded into each real event triggered by CINT7. Two kinematic cuts corresponding to the
 180 interval of the measurements, namely $-4 < y < -2.5$ and $0 \leq p_T < 20$ GeV/c, were applied on the
 181 generated and reconstructed MC data for the $A \times \epsilon$ calculation. The cuts on the reconstructed MC data
 182 in the simulation are similar to the ones used for the raw data sample except for the trigger. The CINT7

p_T (GeV/c)	$dN/dp_T \pm \text{stat}(\%) \pm \text{syst}(\%)$
centrality 40 - 90%	
0–0.3	21263 ± 519 (2.4) ± 465 (2.2)
0.3–1	20498 ± 556 (2.7) ± 595 (2.9)
1–2	25545 ± 436 (1.7) ± 609 (2.4)
2–3	19354 ± 321 (1.7) ± 458 (2.4)
3–4	13759 ± 215 (1.6) ± 438 (3.2)
4–5	8491 ± 148 (1.7) ± 221 (2.6)
5–6	5252 ± 111 (2.1) ± 95 (1.8)
6–7	3151 ± 78 (2.5) ± 56 (1.8)
7–8	1743 ± 55 (3.2) ± 41 (2.4)
8–9	1062 ± 42 (3.9) ± 35 (3.3)
9–10	584 ± 31 (5.3) ± 9 (1.6)
10–11	347 ± 23 (6.5) ± 21 (6.0)
11–12	220 ± 18 (8.3) ± 6 (2.7)
12–15	127 ± 8 (6.3) ± 10 (8.1)
15–20	25 ± 3 (12.1) ± 3 (10.7)

Table 8: J/ ψ dN/d p_T values in 40–90% centrality class.

183 trigger cut is used for the reconstructed simulation.

184 In order to make the number of MC J/ ψ proportional to the number of analyzed CMUL7 events and re-
185 constructed J/ ψ , to account for the evolution of the detector status with time, two weights are considered:

- 186 – a weight proportional to the number of CMUL7 events in each run (the run number weighting),
187 – a weight proportional to the number of reconstructed J/ ψ in data in each centrality bin (the cen-
188 trality weighting).

189 The $A \times \varepsilon_0$ was extracted run per run for each centrality bin and p_T interval. The index "0" for $A \times \varepsilon_0$
190 correspond to the original MC kinematical distributions. The uncertainty on the $A \times \varepsilon$ is computed
191 by selecting the maximum between the $1/N_{\text{gen}}$ and the binomial error, when the number of generated
192 J/ ψ N_{gen} is less or equal to the number of reconstructed J/ ψ N_{rec} . However, if the N_{rec} is larger than N_{gen} ,
193 the uncertainty is computed as $1/N_{\text{gen}}$. The binomial error σ_{bino} is calculated as:

$$\sigma_{\text{bino}} = \sqrt{\frac{N_{\text{rec}}}{N_{\text{gen}}} \times \left(\frac{1 - N_{\text{rec}}/N_{\text{gen}}}{N_{\text{gen}}} \right)}$$

194 5.2 Run dependence

195 Fig. 14 shows $A \times \varepsilon_0$ of the J/ ψ as a function of the run number for the three Pb–Pb periods, for $0 \leq p_T <$
196 20 GeV/c in 0–90% centrality class. The $A \times \varepsilon_0$ decreases at the end of the LHC18r period.

197 In a certain centrality bin, the $A \times \varepsilon_0$ was summed over the run list by weighting the $A \times \varepsilon_0$ with the
198 number of CMUL events. In this procedure, runs are discarded when N_{gen} is equal to 0. Such cases
199 happen mainly in the high p_T bins where the MC statistics can be scarce.

200 5.3 Realistic input MC distribution: iterative procedure

201 The embedding MC generated events according to MB events in centrality bin width of 10%. The p_T
202 and y J/ ψ shapes for the data depend on centrality. For example, the five panels of Fig. 16 and 17

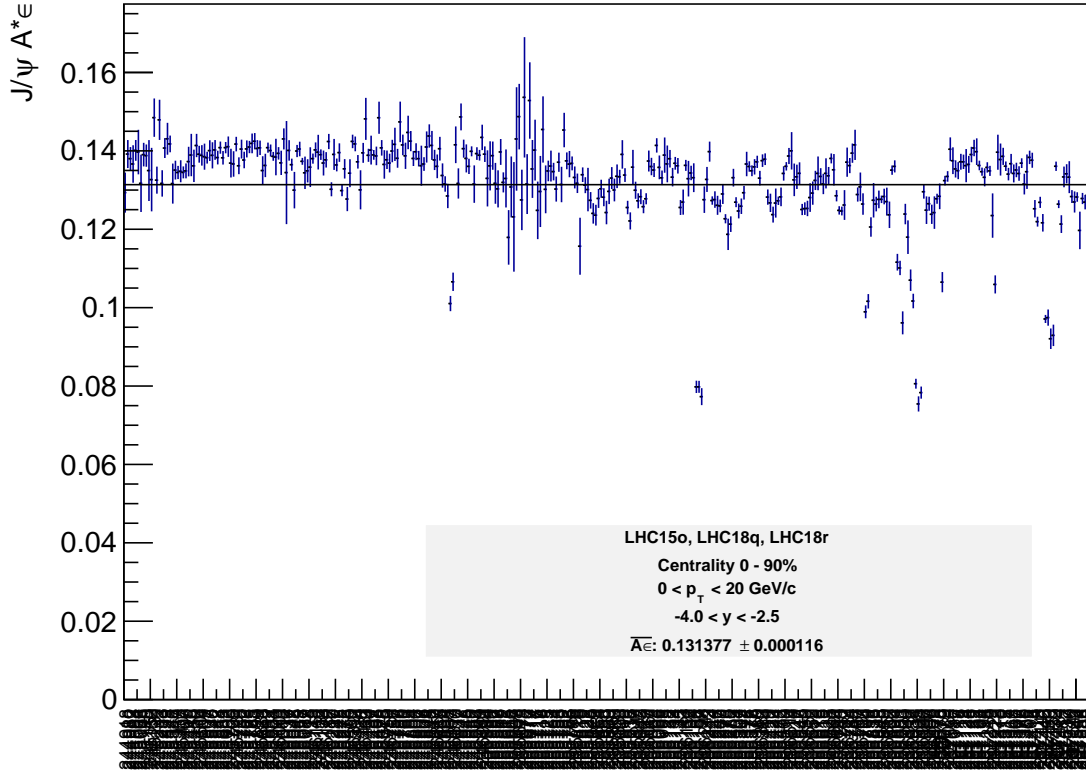


Fig. 14: $J/\psi A \times \varepsilon_0$ as a function of runs for LHC15o, 18q and 18r periods for $2.5 < y < 4$, $0 \leq p_T < 20$ GeV/ c and 0–90% centrality class.

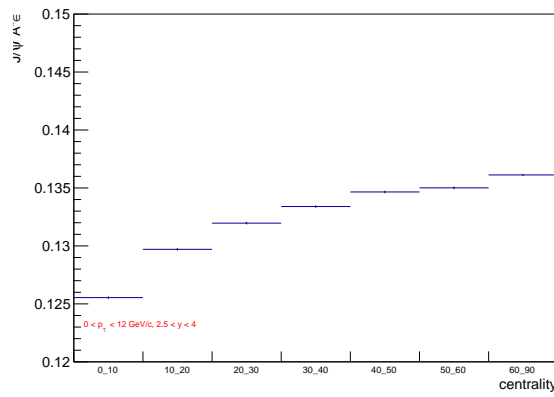


Fig. 15: $J/\psi A \times \varepsilon_0$ as a function of centrality class for LHC15o, 18q and 18r periods for $2.5 < y < 4$, $0 \leq p_T < 12$ GeV/ c .

203 show the p_T and rapidity distributions of the raw data corrected by $A \times \varepsilon_0$ and the absolutely normalized
 204 input MC distributions for 0–10%, 10–20%, 20–30%, 30–40% and 40–90% centrality intervals. The
 205 measured p_T distributions depend on the centrality interval. One needs to tune the distributions to each
 206 centrality class in order to estimate a reliable acceptance and efficiency of the detector. Fig. 15 shows
 207 $A \times \varepsilon_0$ as a function of centrality class for $0 < p_T < 12$ GeV/ c and $2.5 < y < 4$. The values of $A \times \varepsilon_0$ for

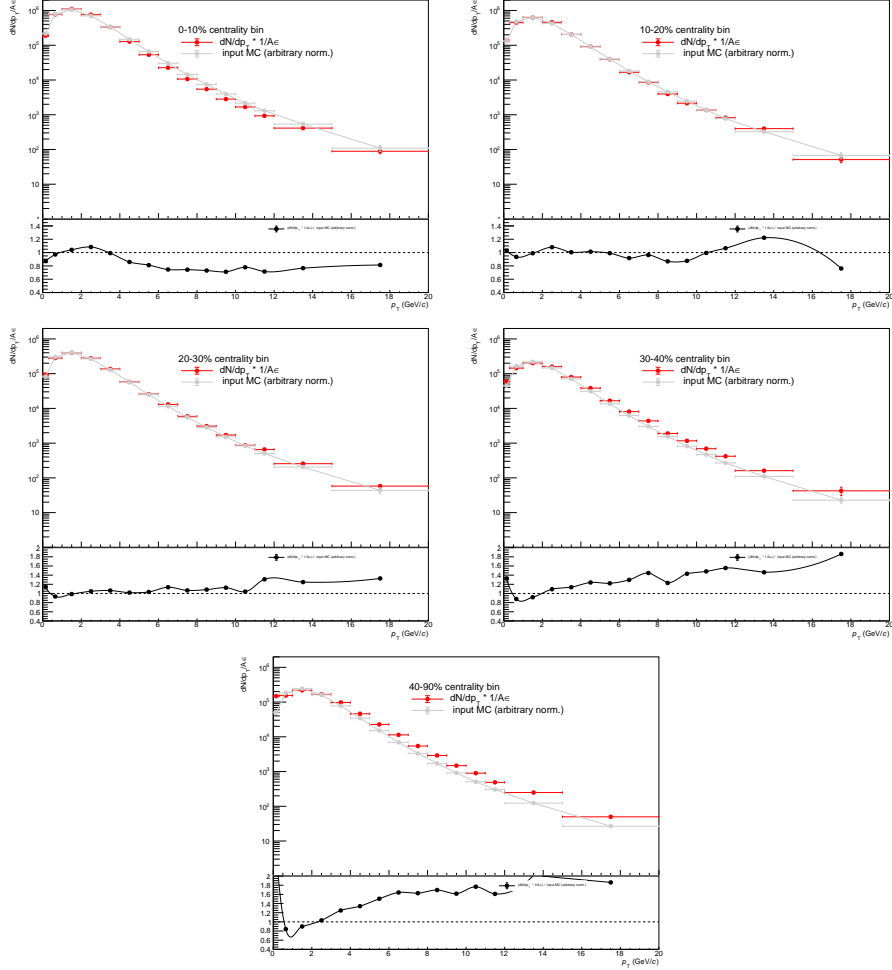


Fig. 16: J/ψ differential $A\varepsilon_0$ corrected distribution as a function of p_T for $2.5 < y < 4$, in 0–10% (left of top panel) and 10–20% (right of top panel), 20–30% (left of middle panel), 30–40% (right of middle panel) and 40–90% (last panel) centrality classes. The corrected distribution (red) are compared to the MC generated distribution (grey) before the iterative procedure.

208 40–50%, 50–60% and 60–90% are close. However, the values of $A \times \varepsilon_0$ for 0–10%, 10–20%, 20–30%
209 and 30–40% are more different. Therefore, the iteration procedure is implemented for 0–10%, 10–20%,
210 20–30%, 30–40% and 40–90%.

211 The p_T and y shapes are described by input functions, which are for p_T distribution:

$$f_i(p_T) = A \times \frac{p_T}{[1 + (\frac{p_T}{B})^{n_1}]^{n_2}} \quad (3)$$

212 where $A = 1.007 * 10^6$, $B = 3.50$, $n_1 = 1.93$ and $n_2 = 3.96$, and for y distribution:

$$f_i(y) = A \times e^{-0.5(\frac{y-n_1}{n_2})^2} \quad (4)$$

213 where $A = 1.099 * 10^6$, $n_1 = 0$, $n_2 = 2.13$. i is a given centrality class. The parameter values correspond
214 to the original input MC. Since the Eq. 3 is not able to describe the corrected data for high p_T , we
215 proposed another empirical functional form:

$$f_i(p_T) = A \times \frac{p_T}{[1 + (\frac{p_T}{B})^{n_1}]^{n_2}} + C \times e^{-n_3 p_T} \quad (5)$$

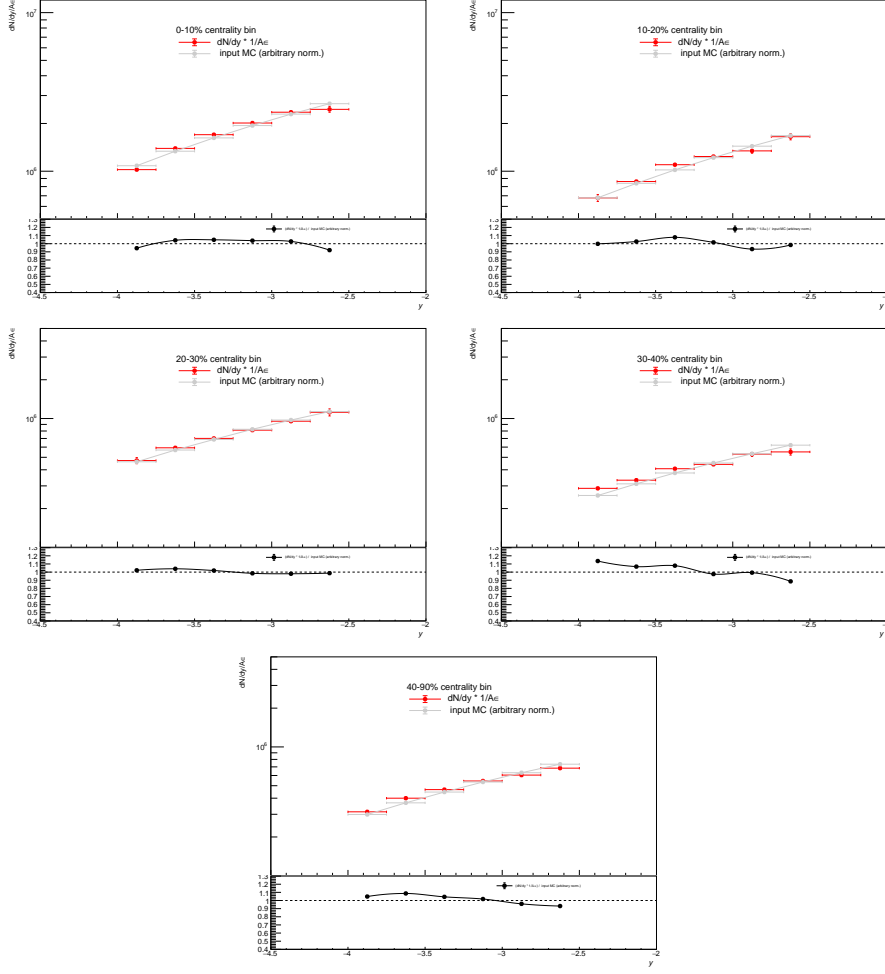


Fig. 17: J/ψ differential $A \times \varepsilon_0$ corrected distribution as a function of y for $0 \leq p_T < 20$ GeV/ c in 0-10% (left of top panel) and 10-20% (right of top panel), 20-30% (left of middle panel), 30-40% (right of middle panel) and 40-90% (last panel) centrality classes. The corrected distribution (red) is compared to the MC generated distribution (grey) before the iterative procedure.

We use the Eq. 4 and 5 to fit the input MC shapes and corrected data. From the fit, we obtained the new fit parameters. In the first and second iterations, the fit parameters of p_T dependence for the data and MC are given in Table D.1, D.2, D.3, and D.4. The fit parameters of rapidity dependence for the data and MC are tabulated in Table D.5, D.6, D.7, and D.8.

A weight can then be calculated as follows:

$$w_i(p_T^{\text{gen}}, y^{\text{gen}}) = w_i(p_T^{\text{gen}}) \times w_i(y^{\text{gen}}), \quad (6)$$

where

$$w_i(p_T^{\text{gen}}) = \frac{f_{i-1}^{\text{corr.}}(p_T^{\text{gen}})}{f_{i-1}^{\text{MC}}(p_T^{\text{gen}})}, \quad (7)$$

and

$$w_i(y^{\text{gen}}) = \frac{f_{i-1}^{\text{corr.}}(y^{\text{gen}})}{f_{i-1}^{\text{MC}}(y^{\text{gen}})}. \quad (8)$$

Note that, p_T^{gen} and y^{gen} are the generated J/ψ transverse momentum and rapidity. $f_i^{\text{corr.}}$ and f_i^{MC} are the functions fitted to the corrected data and the input MC at i step, respectively. Then the weights are

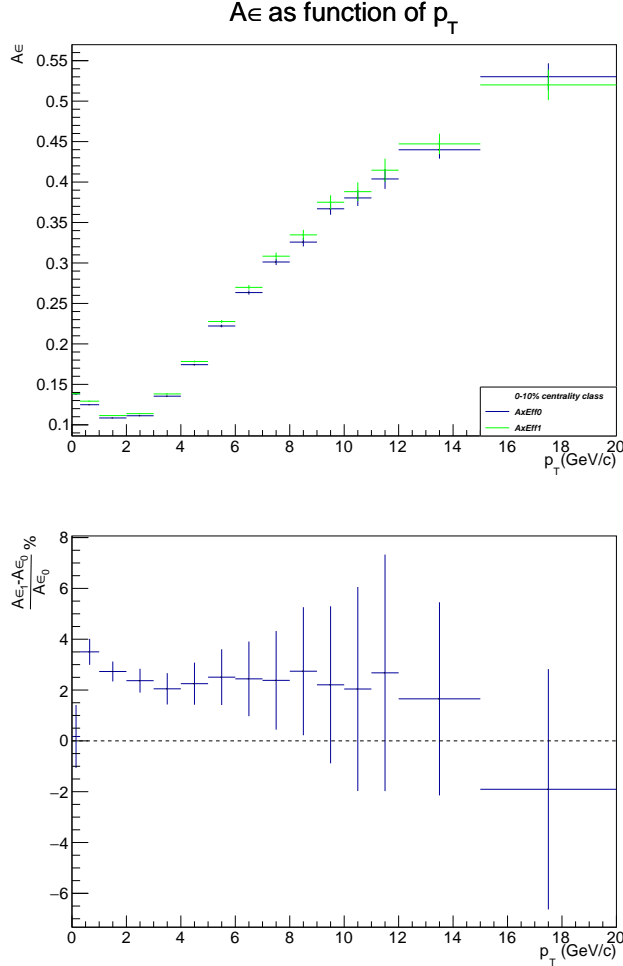


Fig. 18: Top: J/ ψ $A\epsilon$ as a function of p_T for LHC15o, 18q and 18r periods for $2.5 < y < 4$, and 0–10% centrality class. Bottom: The relative difference on J/ ψ $A \times \epsilon_0$ and $A \times \epsilon$ as a function of p_T for $2.5 < y < 4$ and 0–10% centrality class.

225 applied to each J/ ψ event at generated and reconstructed levels. The $A \times \epsilon$ is then recomputed with
 226 weighted MC. The new $A \times \epsilon$ is defined as $A \times \epsilon_1$. The index "1" of $A \times \epsilon_1$ specifies that the values are
 227 obtained from the first iterative procedure. $A \times \epsilon_1$ and $A \times \epsilon_0$ as a function of p_T and y are shown at top
 228 panels of Fig. 18, 19, 20, 21, 22, and 23. The blue points correspond to $A \times \epsilon_0$ with the original input MC
 229 shape while the green points correspond to $A \times \epsilon_1$ with the tuned input MC shape. The bottom panels of
 230 the two figures show the relative difference of $A \times \epsilon_1$ and $A \times \epsilon_0$. The effect of tuning increases $A \times \epsilon$
 231 as a function of p_T but decreases as a function of y for . However, the amount of relative difference as
 232 a function of y is small below 2.5%. Fig. 24 and 25 show the p_T and y distributions of the raw data
 233 corrected by $A \times \epsilon_1$ and the tuned normalized input MC distributions, and their ratios, for 0-10% and
 234 10-20%, 20-30%, 30-40%, 40-90% centrality intervals. The ratios are closed to one in most common p_T
 235 and y bins. Notice that the first p_T bin is excluded from the tuning procedure, as a result the ratio is not
 236 closed to unity in that bin. The effect on the second iteration was checked. The weights for the second
 237 iteration are obtained from the fitting on the weighted input shapes of the first iteration. Those weights
 238 of the second and the first iteration are applied again to each J/ ψ event at generated and reconstructed
 239 levels. The results turn out that the $A \times \epsilon_2$ obtained from the second iterative procedure is similar to $A\epsilon_1$.
 240 Hence we use $A \times \epsilon_1$ in this AN. The acceptance efficiency after the first iterative procedure is denoted
 241 as $A \times \epsilon$ in the following.

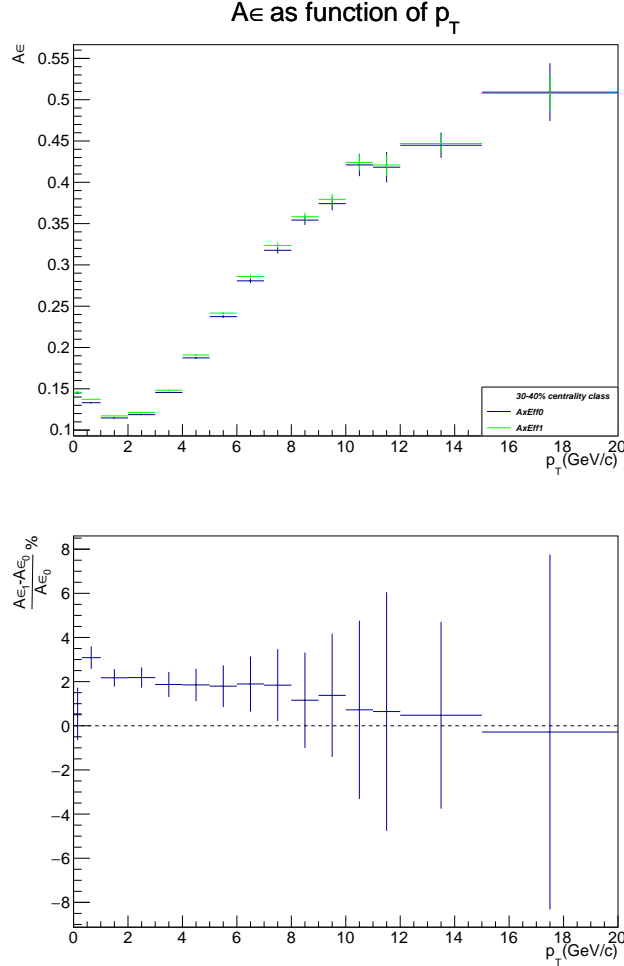


Fig. 19: Top: $J/\psi A \times \epsilon$ as a function of p_T for LHC15o, 18q and 18r periods for $2.5 < y < 4$, and 30–40% centrality class. Bottom: The relative difference on $J/\psi A \times \epsilon_0$ and $A \times \epsilon$ as a function of p_T for $2.5 < y < 4$ and 30–40% centrality class.

242 5.4 Results

243 Table 9 gives the values of $A \times \epsilon$ in different p_T intervals for 0–20% centrality class. The iterative
 244 procedure is also completed for 20–40% and 40–90% centrality classes. Table 10 gives the values of
 245 $A \times \epsilon$ in different p_T intervals for 20–40% and 40–90% centrality classes.

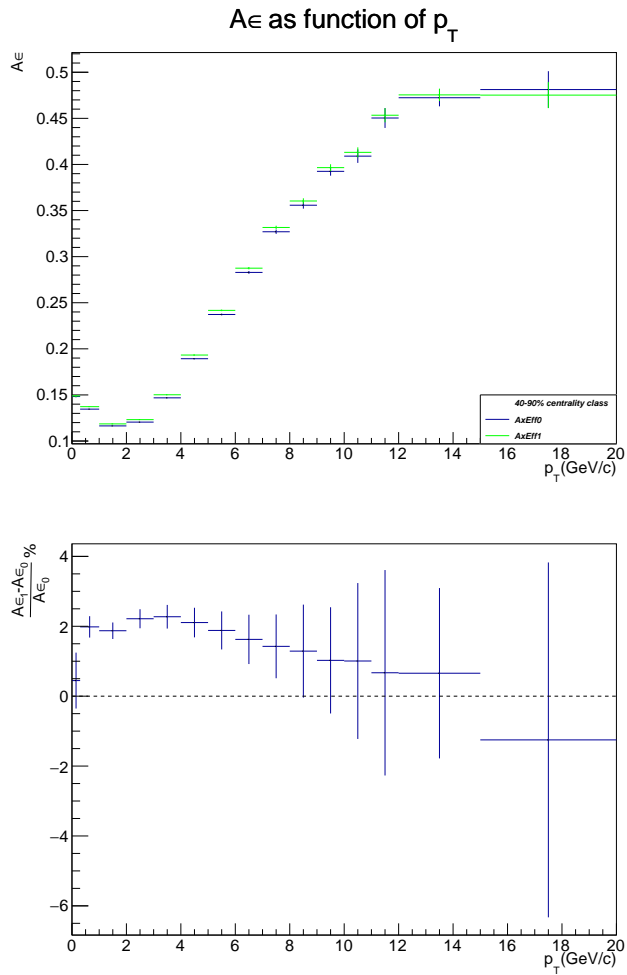


Fig. 20: Top: J/ ψ $A \times \epsilon$ as a function of p_T for LHC15o, 18q and 18r periods for $2.5 < y < 4$, and 40–90% centrality class. Bottom: The relative difference on J/ ψ $A \times \epsilon_0$ and $A \times \epsilon$ as a function of p_T for $2.5 < y < 4$ and 40–90% centrality class.

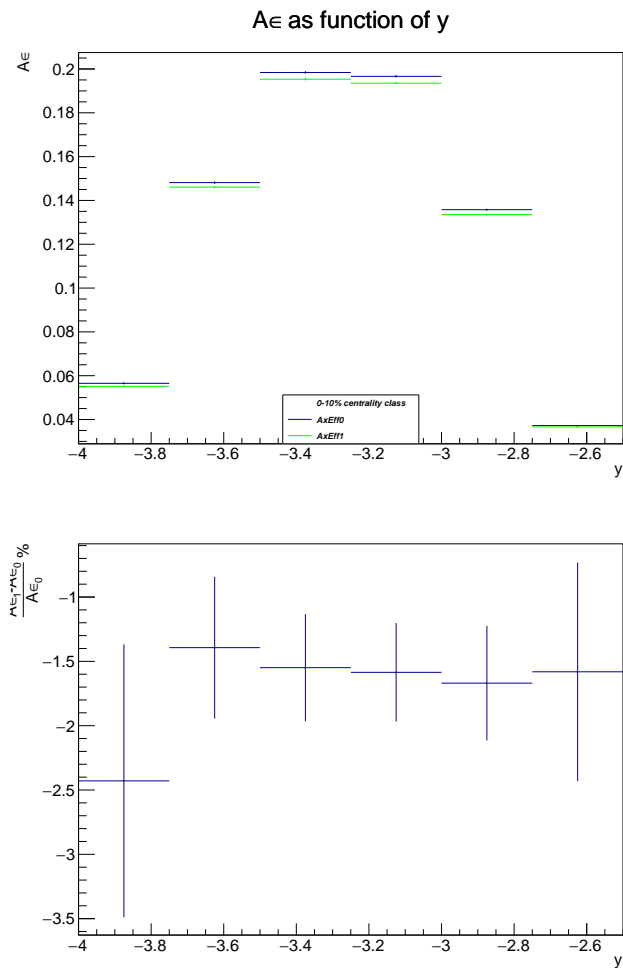


Fig. 21: Top: $J/\psi A \times \epsilon$ as a function of y for LHC15o, 18q and 18r periods for $0 \leq p_T < 20 \text{ GeV}/c$, and $0-10\%$ centrality class. Bottom: The relative difference on $J/\psi A \times \epsilon_0$ and $A \times \epsilon$ as a function of y for $0 \leq p_T < 20 \text{ GeV}/c$, and $0-10\%$ centrality class.

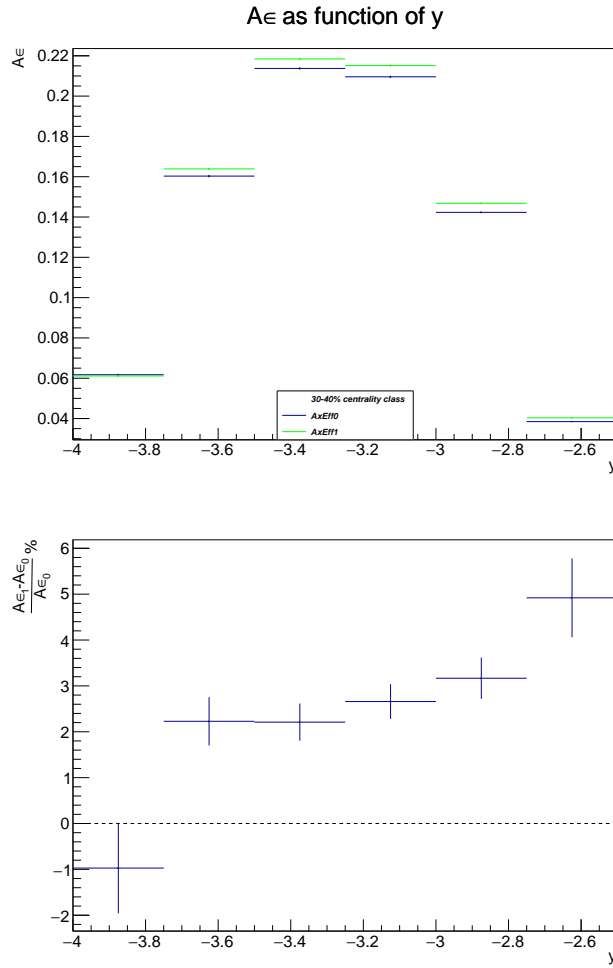


Fig. 22: Top: J/ ψ $A \times \epsilon$ as a function of y for LHC15o, 18q and 18r periods for $0 \leq p_T < 20$ GeV/ c , and 30–40% centrality class. Bottom: The relative difference on J/ ψ $A \times \epsilon_0$ and $A \times \epsilon$ as a function of y for $0 \leq p_T < 20$ GeV/ c , and 30–40% centrality class.

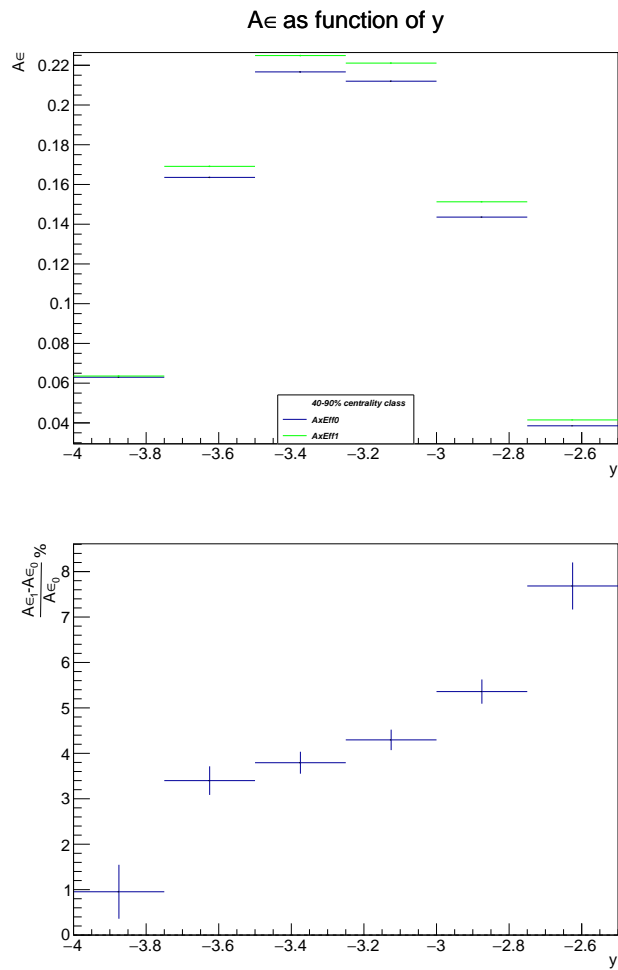


Fig. 23: Top: $J/\psi A \times \epsilon$ as a function of y for LHC15o, 18q and 18r periods for $0 \leq p_T < 20 \text{ GeV}/c$, and 40–90% centrality class. Bottom: The relative difference on $J/\psi A \times \epsilon_0$ and $A \times \epsilon$ as a function of y for $0 \leq p_T < 20 \text{ GeV}/c$, and 40–90% centrality class.

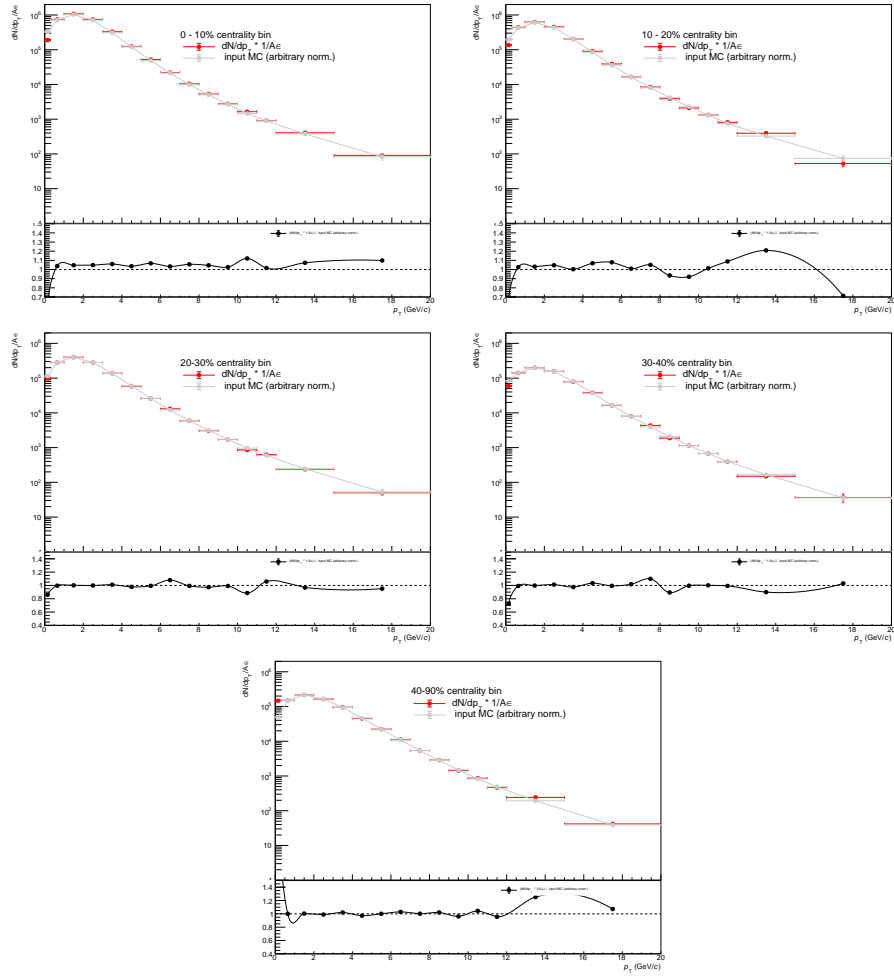


Fig. 24: J/ ψ differential $A \times \varepsilon_1$ corrected distribution as a function of p_T for $2.5 < y < 4$, in 0-10% (left of top panel) and 10-20% (right of top panel), 20-30% (left of middle panel), 30-40% (right of middle panel) and 40-90% (last panel) centrality classes. The corrected distribution (red) are compared to the MC generated distribution (grey) after the first step of the iterative procedure.

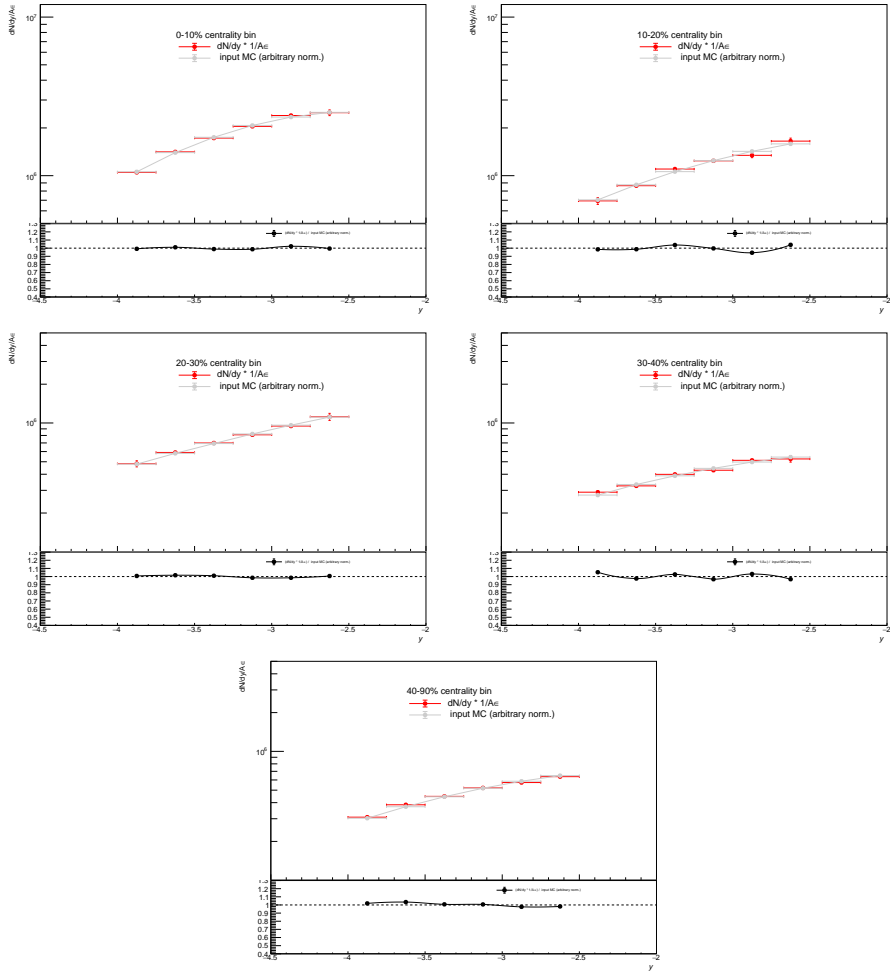


Fig. 25: J/ψ differential $A \times \epsilon_1$ corrected distribution as a function of y for $0 \leq p_T < 20$ GeV/c in 0-10% (left of top panel) and 10-20% (right of top panel), 20-30% (left of middle panel), 30-40% (right of middle panel) and 40-90% (last panel) centrality classes. The corrected distribution (red) are compared to the MC generated distribution (grey) after the first step of the iterative procedure.

centrality 0 – 20 %	
p_T (GeV/c)	$A \times \varepsilon \pm$ stat. (%)
0–0.3	0.139 ± 0.0008 (0.58)
0.3–1	0.130 ± 0.0003 (0.23)
1–2	0.113 ± 0.0002 (0.18)
2–3	0.116 ± 0.0003 (0.26)
3–4	0.140 ± 0.0004 (0.29)
4–5	0.181 ± 0.0007 (0.39)
5–6	0.228 ± 0.0012 (0.53)
6–7	0.275 ± 0.0020 (0.73)
7–8	0.312 ± 0.0029 (0.93)
8–9	0.339 ± 0.0041 (1.21)
9–10	0.370 ± 0.0056 (1.51)
10–11	0.389 ± 0.0073 (1.88)
11–12	0.414 ± 0.0092 (2.22)
12–15	0.447 ± 0.0082 (1.83)
15–20	0.492 ± 0.0114 (2.32)

Table 9: J/ ψ acceptance times efficiency as a function of p_T for $2.5 < y < 4$ and 0–20% centrality class.

centrality 20 – 40 %		centrality 40 – 90 %	
p_T (GeV/c)	$A \times \varepsilon \pm$ stat. (%)	p_T (GeV/c)	$A \times \varepsilon \pm$ stat. (%)
0–0.3	0.141 ± 0.0008 (0.59)	0–0.3	0.149 ± 0.0009 (0.58)
0.3–1	0.134 ± 0.0004 (0.26)	0.3–1	0.137 ± 0.0003 (0.23)
1–2	0.115 ± 0.0002 (0.20)	1–2	0.119 ± 0.0002 (0.17)
2–3	0.119 ± 0.0003 (0.23)	2–3	0.123 ± 0.0002 (0.19)
3–4	0.145 ± 0.0004 (0.29)	3–4	0.150 ± 0.0003 (0.23)
4–5	0.188 ± 0.0007 (0.38)	4–5	0.193 ± 0.0005 (0.28)
5–6	0.236 ± 0.0012 (0.50)	5–6	0.242 ± 0.0008 (0.35)
6–7	0.278 ± 0.0018 (0.65)	6–7	0.287 ± 0.0013 (0.45)
7–8	0.319 ± 0.0027 (0.86)	7–8	0.332 ± 0.0019 (0.57)
8–9	0.353 ± 0.0039 (1.09)	8–9	0.360 ± 0.0029 (0.81)
9–10	0.372 ± 0.0053 (1.41)	9–10	0.397 ± 0.0037 (0.93)
10–11	0.424 ± 0.0077 (1.82)	10–11	0.413 ± 0.0054 (1.32)
11–12	0.426 ± 0.0112 (2.64)	11–12	0.453 ± 0.0077 (1.70)
12–15	0.429 ± 0.0095 (2.21)	12–15	0.475 ± 0.0068 (1.42)
15–20	0.493 ± 0.0182 (3.70)	15–20	0.475 ± 0.0141 (2.97)

Table 10: J/ ψ acceptance times efficiency as a function of p_T for $2.5 < y < 4$ and several centrality classes.

246 6 Normalization factor

247 In order to compute the number of minimum bias (MB) events, N_{MB} , equivalent to the number of CMUL
 248 events in our data sample, N_{CMUL} , the evaluation of the normalization factor F_{norm} has been done. In this
 249 analysis, we take the values of F_{norm}^i where i is the run number, computed by another analyzer for the
 250 2015 analysis and the 2018 analysis [4] to obtain the average normalization factor, F_{norm} . In this way, in
 251 order to have the final F_{norm} , we consider our numbers of analyzed CMUL events run per run.

252 6.1 The F_{norm} calculation methods

253 Although we do not calculate the normalization factor, we introduce the methods to obtain F_{norm} run by
 254 run for completeness.

255 F_{norm}^i is defined in Eq. 9. N_{MB}^i is the number of MB events in the 0–90% centrality class in a run i :

$$N_{\text{MB}}^i = F_{\text{norm}}^i \times N_{\text{CMUL7}}^i \quad (9)$$

256 with N_{CMUL7}^i the number of CMUL7 triggered events in the same centrality class. The normalization
 257 factors F_{norm}^i can be calculated with two different methods. Each method is described in the following
 258 sections.

259 We also would like to introduce the pile-up factor PU , which corrects for pile-up events in the collisions.
 260 The pile-up factor correction should be applied to both offline and online method since the relevant
 261 offline selection are not applied in both cases. The pile-up factor is defined as:

$$PU^i = \frac{\mu^i}{1 - e^{-\mu^i}}, \quad (10)$$

262 where μ^i is the mean number of collisions per bunch crossing in a run i , and is defined as:

$$\mu^i = -\ln\left(1 - \frac{F_{\text{purity}}^{\text{MB},i} \times L0b_{\text{rate}}^{\text{MB},i}}{N_{\text{colliding}}^i \times f_{\text{LHC}}}\right). \quad (11)$$

263 $F_{\text{purity}}^{\text{MB},i}$ is the purity factor associated to minimum bias events. $L0b_{\text{rate}}^{\text{MB},i}$ is the rate of MB triggered events.
 264 $N_{\text{colliding}}^i$ is the number of colliding bunches. f_{LHC} is the revolution frequency of the LHC beam. According
 265 to reference [4], the average of the pileup factor over Run2 (2015+2018) is around 1.0004 which is
 266 a tiny correction. It was therefore neglected in the following.

267 6.1.1 Offline method

268 The offline indirect method is based on the offline counters from reconstructed data, namely AODs. The
 269 $F_{\text{Norm}}^{\text{offline},i}$ is computed for each run i by using the following formula:

$$F_{\text{norm}}^{\text{offline1},i} = \frac{N_{\text{MB}}^i}{N_{\text{MB}\&0\text{MUL}}^i} \quad (12)$$

270 where:

271 – $N_{\text{MB}}^i\&0\text{MUL}$ is the subsample of MB (CINT7) events, which is also fired by the 0MUL trigger
 272 input.

273 However, the CINT7 trigger is heavily downsampled, leading to a low number of reconstructed CINT7
 274 triggered events. Thus this method lacks of statistics. To increase the statistical precision, an intermediate

trigger, with a lower downscaling factor is used, the CMSL7 trigger. The formula for the offline method becomes:

$$F_{\text{norm}}^{\text{offline2},i} = \frac{N_{\text{MB}}^i}{N_{\text{MB}\&0\text{MSL}}^i} \times \frac{N_{\text{CMSL7}}^i}{N_{\text{CMSL7}\&0\text{MUL}}^i} \quad (13)$$

where:

- N_{CMSL7}^i is the number of physics selected CMSL7 (low p_T single muon) triggered events,
- $N_{\text{MB}\&0\text{MSL}}^i$ is the subsample of CINT7 events fired also by the 0MSL trigger input,
- $N_{\text{CMSL7}\&0\text{MUL}}^i$ is the subsample of CMSL7 events fired also by the 0MUL trigger input.

6.1.2 Online method

The second method uses the $L0b$ scaler inputs stored in the OCDB (online information). In that case, F_{norm}^i is computed for each run i as:

$$F_{\text{norm}}^{\text{online},i} = \frac{L0b_{\text{MB}}^i \times P_{\text{MB}}^i}{L0b_{\text{CMUL7}}^i \times P_{\text{CMUL7}}^i} \quad (14)$$

where:

- P_{MB}^i and P_{CMUL7}^i are the purity factor for MB (CINT7) and unlike-sign dimuon (CMUL7) triggers, respectively,
- $L0b_{\text{MB}}^i$ and $L0b_{\text{CMUL7}}^i$ are the scaler counters of CINT7 and CMUL7 triggers, respectively.

The purity factor in that method is computed offline from reconstructed events, as the fraction of events which pass the physics selection in the corresponding trigger class.

6.2 Results

The normalization factor is computed by using the online and offline methods as discussed in Section 6.1.1 and 6.1.2. In this section, we show the F_{norm}^i obtained by other analyzers, as a function of the run number, in Fig. 26 for LHC15o and in Fig. 27 for LHC18q and LHC18r.

In order to compute the average F_{norm} factor over a period, the CMUL7 events in our analysis is used for each run i by using:

$$F_{\text{norm}} = \frac{\sum_i F_{\text{norm}}^i \times N_{\text{CMUL7}}^i}{\sum_i N_{\text{CMUL7}}^i} \quad (15)$$

and the uncertainty is obtained as:

$$F_{\text{norm}}^{\text{err}} = \frac{\sqrt{\sum_i (\delta F_{\text{norm},i})^2 \times (N_{\text{CMUL7}}^i)^2}}{\sum_i N_{\text{CMUL7}}^i} \quad (16)$$

The results of the average normalization factors are shown in Table 11. The results are compared to another analysis. The agreement is within 0.1% in each period because the analysed statistics is quite similar in each run. The average F_{norm} for the three methods in a given period is obtained by taking into account the statistical error on F_{norm} as a weight. The average F_{norm} for the three periods is also obtained according to Eq. 15 considering the periods from LHC15o to LHC18r. To determine the systematic uncertainty on F_{norm} , the value from online method is taken as the central value because of the highest

statistical precision. The largest relative difference between the central value and values obtained with the other methods among the three periods is taken as systematic uncertainty.

In order to calculate the number of minimum bias (MB) events in the 0–90% centrality class, we use:

$$N_{\text{MB}} = F_{\text{norm}} \times N_{\text{CMUL7}} \quad (17)$$

Since the MB events are distributed equally in each centrality bin, we can derive the number of MB events in each centrality bin by dividing by the factor $90/\Delta_{\text{cent}}$, where Δ_{cent} is the centrality bin width. One could also derive the normalisation factor in each centrality bin. In that case, larger statistical uncertainty should be obtained, therefore this method was not used. Note that the total cross section of Pb-Pb collisions at $\sqrt{s_{\text{NN}}} = 5.02 \text{ TeV}$ σ_{PbPb} is equal to 7.67 ± 0.16 (syst.) b [5].

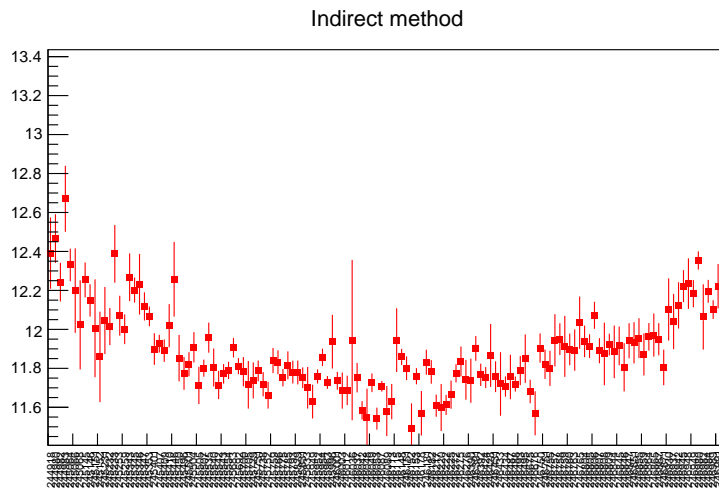


Fig. 26: The normalization factor run by run in LHC15o obtained with the indirect offline method (Sizar).

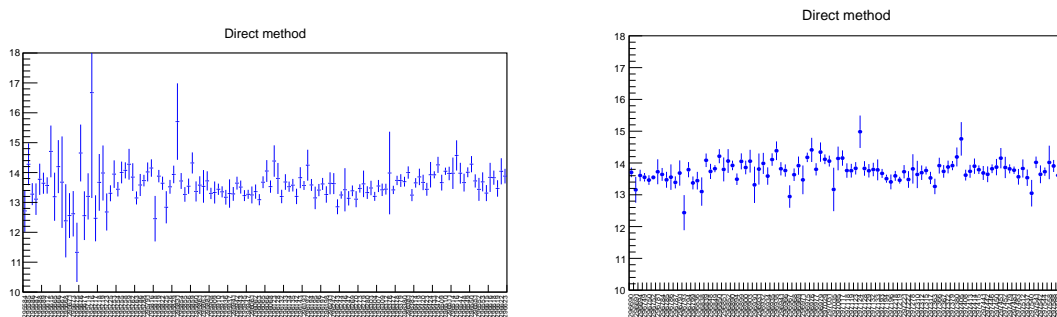


Fig. 27: The normalization factor run by run in LHC18q obtained with the direct offline method in LHC18q (left) and LCH18r (right).

311 7 Systematic Uncertainties

In this section the systematic uncertainties on the $J/\psi R_{AA}$ measurement (see Eq. 19) as a function of p_T are discussed, and summarized in Table 12.

314 7.1 Signal extraction

The systematic uncertainty on signal extraction are discussed in Section 4 and are given in Table 3, Table 4 and Table 5 for each p_T interval.

	$F_{\text{norm}} \pm \text{stat}$ Offline direct CINT7	$F_{\text{norm}} \pm \text{stat}$ Offline indirect CINT7	$F_{\text{norm}} \pm \text{stat}$ Online COVOM	Avg.
LHC15o	11.84 ± 0.012 (CL)	11.85 ± 0.007 (CL)	11.88 ± 0.001 (CL)	$11.87 \pm 0.01\%$ (CL)
	11.84 ± 0.011 (Sizar)	11.85 ± 0.007 (Sizar)	11.88 ± 0.001 (Sizar)	11.87 (Sizar)
LHC18q	13.59 ± 0.026 (CL)	13.59 ± 0.013 (CL)	13.56 ± 0.0012 (CL)	$13.56 \pm 0.01\%$ (CL)
	13.57 ± 0.022 (Sizar)	13.57 ± 0.012 (Sizar)	13.54 ± 0.0012 (Sizar)	13.54 (Sizar)
LHC18r	13.75 ± 0.022 (CL)	13.72 ± 0.012 (CL)	13.65 ± 0.001 (CL)	$13.65 \pm 0.01\%$ (CL)
	13.76 ± 0.021 (Sizar)	13.73 ± 0.011 (Sizar)	13.65 ± 0.001 (Sizar)	13.65 (Sizar)
Results				$13.06 \pm 0.73\%$ (syst.) (CL)

Table 11: Normalization factor for LHC15o, LHC18q, LHC18r in the three periods. The values are compared to another analysis.

317 7.2 Monte Carlo parametrisation

318 This systematic uncertainty is taken from the largest relative difference between $A\varepsilon$ and $A\varepsilon_0$ shown in
 319 bottom panel of Fig. 18, which is 3.5% at second p_T bin. For 20–40% centrality class, its systematic
 320 uncertainty is taken from the largest relative difference on acceptance efficiency shown in Fig. 19 is 3%
 321 at second p_T bin. As for 40–90% centrality class, its systematic uncertainty of 2.4% is also taken from
 322 the largest relative difference on acceptance efficiency.

323 7.3 Tracking efficiency

324 The systematic uncertainty of tracking efficiency has been evaluated for the LHC18q and LHC18r peri-
 325 ods [6]. The tracking efficiency systematic uncertainty is found to be 1.5% at the single muon level, hence
 326 3% for the J/ψ , and is assumed uncorrelated versus p_T , however, correlated as a function of centrality.
 327 The same tracking efficiency systematic uncertainty was also found in the 2015 analysis. We therefore
 328 adopted this 3% value for the 2015+2018 data sample. There is an additional systematic uncertainty in
 329 most central collisions from the loss of tracking efficiency with increasing collision centrality estimated
 330 to be 0.5% for single muon and consequently, 1% for dimuons. This latter uncertainty is correlated over
 331 p_T [7].

332 7.4 Trigger efficiency

333 There are two components to this systematic bias: the uncertainty on the trigger response and the uncer-
 334 tainty on the intrinsic trigger efficiency. The evaluation of this systematic uncertainty is done by another
 335 analysis on 2015 data sample and the detail is described in [8]. In this AN, for 0–20% centrality interval,
 336 we have considered the largest uncertainty on the trigger response which is 2.9% with 1% correlated
 337 systematic over p_T and an intrinsic trigger efficiency of 1.5%. The latter is the same as in the 2015 Pb–Pb
 338 analysis [9]. As a result, the total uncorrelated systematic uncertainty over p_T is 3.3 %. In this version of
 339 the AN, the systematic uncertainty on the muon trigger is estimated and the results is written in appendix
 340 C. According to Table C.2, their range of the uncertainty on the trigger is from 0.11–1.4%. Besides, an
 341 intrinsic trigger efficiency of 1.5% is considered. Therefore, the total uncorrelated systematic uncertainty
 342 range is from 1.5–2%. The correlated systematic over p_T for 20–40%, and 40–90% centrality intervals
 343 are 0.5% and 0, respectively [8]. Note that the trigger uncertainty from the intrinsic trigger efficiency is
 344 not yet evaluated for 2018. We checked the stability of the J/ψ invariant yield in the 2015 and 2015+2018
 345 periods. This check shows that the trigger efficiency is expected not to vary significantly between the
 346 two data taking periods.

347 7.5 Matching trigger-tracker track efficiency

348 A 1% systematic uncertainty is considered as in previous analyses of Run2 [9]. Indeed the reconstruction
 349 parameters did not change in Run2.

350 7.6 pp reference cross sections

351 The systematic uncertainties on the pp cross sections are taken from [10].

352 7.7 Others

353 The systematic uncertainty on the $\langle T_{AA} \rangle$ is obtained by the Glauber model for several centrality bins
 354 in [5]. Its corresponding values have been given in Table 13.

355 The systematic uncertainty on the centrality limits were computed by comparing the number of J/ψ with
 356 difference centrality estimator in [7] for the 2015 sample.

357 The systematic uncertainty on F_{norm} has been given in Table 11.

358 The uncertainties on $\langle T_{AA} \rangle$, centrality limit, F_{norm} and the correlated part of the pp cross section, track-
 359 ing and trigger uncertainties lead to a global correlated systematic uncertainty of 2.6%, 2.5% and 3.2%
 360 in 0–20%, 20–40% and 40–90% centrality intervals, respectively. This does not include the systematic
 361 on branching ratio which cancel out in the R_{AA} computation.

source	vs p_T (%) (0–20%)	vs p_T (%) (20–40%)	vs p_T (%) (40–90%)
Branching ratio		0.5*	
F_{norm}		0.73*	
Signal extraction	1.6 – 5.8	1.9 – 4.5	1.6 – 10.7
MC input	3.5	3	2.3
MCH efficiency	3.0 + 1.0*	3.0 + 0.5*	3.0
MTR efficiency	3.3 + 1.0*	1.5-2.0	1.5-2.0
Matching		1	
T_{AA}	0.75*	1.31*	2.04*
Centrality limit	0.4*	0.2*	1.4*
pp cross section reference		3.5 – 5.6 + 1.9*	

Table 12: Summary of the systematic uncertainties. The values marked with an asterisk correspond to uncertainties correlated over p_T . The values in red means the systematic uncertainties are preliminary.

362 8 Results

363 The J/ψ invariant yield, N_{AA} , is defined as:

$$N_{AA} = \frac{N_{J/\psi \rightarrow \mu\mu}(\Delta y, \Delta p_T)}{BR(J/\psi \rightarrow \mu\mu) \times N_{MB} \times A \times \varepsilon(\Delta y, \Delta p_T)}, \quad (18)$$

364 where BR is the J/ψ to dimuon branching ratio and amounts to $5.96 \pm 0.03\%$ [11], N_{MB} is the number
 365 of minimum bias events as described in Section 6. $N_{J/\psi}(\Delta y, \Delta p_T)$ is the inclusive J/ψ yield for a given
 366 range in p_T and y . $A \times \varepsilon(\Delta y, \Delta p_T)$ is the acceptance times efficiency of the detector. Note that for the
 367 calculation of the $A\varepsilon$, the J/ψ production is assumed to be unpolarized.

368 The J/ψ nuclear modification factor is computed as:

$$R_{AA} = \frac{N_{AA}}{\sigma_{J/\psi}^{pp} \times \langle T_{AA} \rangle}, \quad (19)$$

369 where $\sigma_{J/\psi}^{pp}$ is the J/ψ cross section in pp collisions at $\sqrt{s} = 5.02$ TeV and $\langle T_{AA} \rangle$ the average nuclear
 370 overlap function. The values for $\langle T_{AA} \rangle$ are given in Table 13. Note that the systematic uncertainty on
 371 $\langle T_{AA} \rangle$ in 40–90% centrality bin is estimated by using the weighted average of the systematic bias in
 10% centrality interval. The weight is the width of the centrality bin.

Centrality	$T_{\text{PbPb}} \pm \text{syst. (\%)} (1/\text{mbarn})$
0–20%	$18.83 \pm 0.142 (0.75)$
20–40%	$6.93 \pm 0.091 (1.31)$
40–60%	$2.05 \pm 0.039 (0.04)$
40–90%	$1.00 \pm 0.021 (2.04)$
60–80%	$0.42 \pm 0.011 (2.53)$
80–90%	$0.08 \pm 0.002 (2.12)$

Table 13: T_{AA} and its systematic uncertainties for Pb–Pb collisions at $\sqrt{s_{NN}} = 5.02$ TeV for various centrality classes [5].

372
 373 The invariant yield obtained from Run2 statistics is compared to the 2015 results as a function of p_T
 374 in the three different centrality bins. The values in 0–20%, 20–40% and 40–90% centrality bins from
 375 2015 are taken from [12]. The statistical uncertainty on the ratio is calculated by considering that the
 376 two datasets are fully correlated. For 0–20% centrality bin, the yield ratio, shown in Fig. 28, is closed
 377 to unity as expected, for the all p_T range. For the 20–40% centrality bin, the yield ratio, shown in Fig.
 378 29, is also closed to unity. However, for the 40–90% centrality bin, the yield ratio, shown in Fig. 30,
 379 is systematically below unity. Note that the acceptance efficiency with the original MC input shape in
 380 20–40% and 40–90% centrality bins are used.

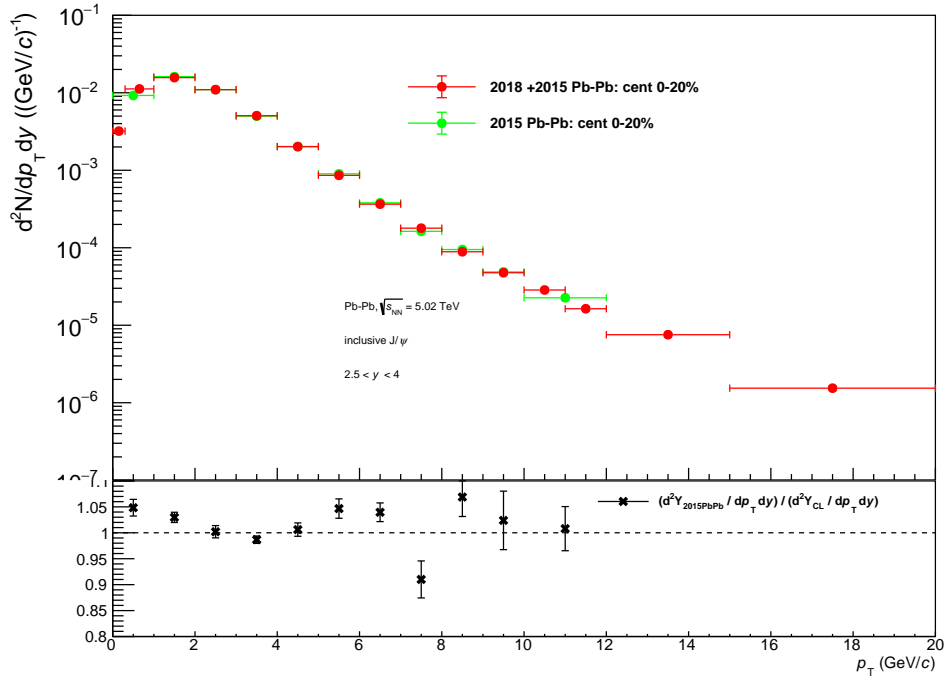


Fig. 28: J/ψ invariant yield as a function of p_T for $2.5 < y < 4$ in 0–20% centrality class compared to the 2015 analysis. The ratio uncertainties are calculated by considering that the data samples are fully correlated.

381 The R_{AA} values are compared to the 2015 data published results [9] in Fig. 31. Table 17 gives the
 382 R_{AA} in various p_T intervals in 0–20% centrality bin for the published and current analysis. The 2015

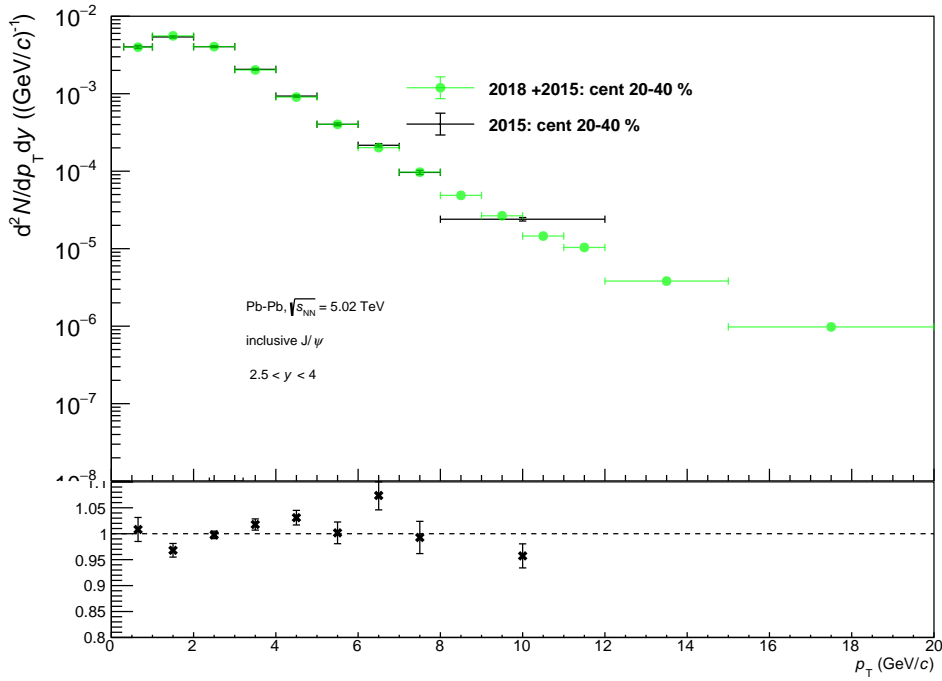


Fig. 29: J/ψ invariant yield as a function of p_T for $2.5 < y < 4$ in 20–40% centrality class compared to the 2015 analysis. The ratio uncertainties are calculated by considering that the data samples are fully correlated.

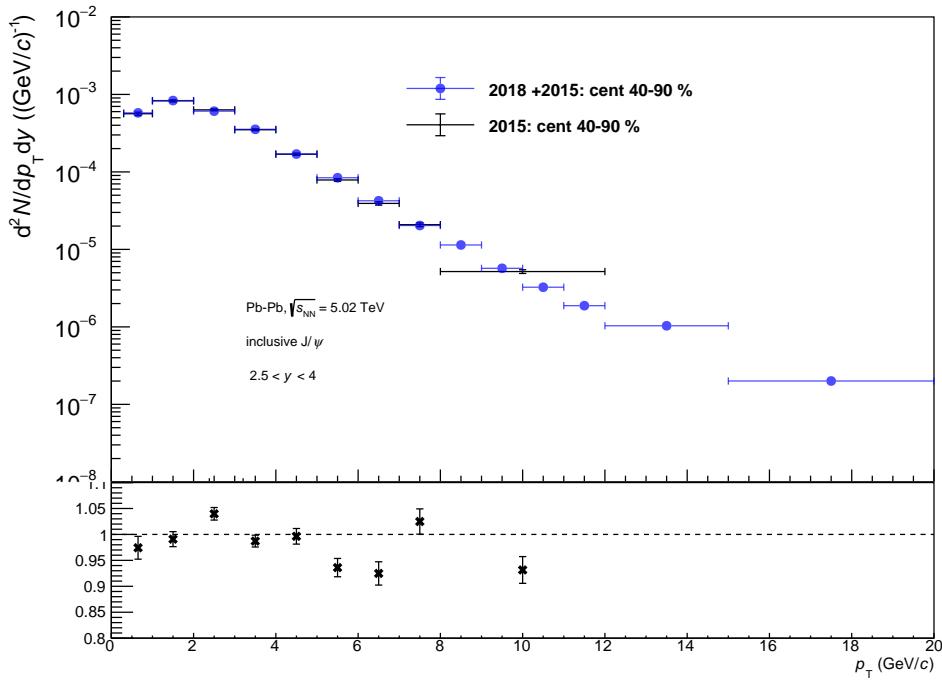


Fig. 30: J/ψ invariant yield as a function of p_T for $2.5 < y < 4$ in 40–90% centrality class compared to the 2015 analysis. The ratio uncertainties are calculated by considering that the data samples are fully correlated.

383 R_{AA} result uses the 2015 pp cross sections. In this analysis, the reference cross section was updated
 384 using the new preliminary pp cross sections from the 2017 data sample, which contains about 10 times
 385 more statistics than the 2015 one. The new R_{AA} versus p_T measurement in the centrality range 0–20%,

p_T (GeV/c)	$d^2N_{\text{AA}}/dydp_T \pm (\text{stat}) (\%) (\text{GeV}/c^{-1})$ (CL)	2015 data
0–0.3	3.22e-03 \pm 1.92e-04 (6.0) \pm 2.24e-04 (7.0)	–
0.3–1	1.13e-02 \pm 2.39e-04 (2.1) \pm 7.19e-04 (6.4)	–
0–1	8.81e-03 \pm 1.76e-04	9.24e-03 \pm 3.26e-04
1–2	1.58e-02 \pm 2.08e-04 (1.3) \pm 9.47e-04 (6.0)	1.62e-02 \pm 3.68e-04
2–3	1.10e-02 \pm 1.36e-04 (1.2) \pm 7.13e-04 (6.5)	1.10e-02 \pm 2.66e-04
3–4	5.08e-03 \pm 9.37e-05 (1.8) \pm 3.25e-04 (6.4)	4.99e-03 \pm 1.28e-04
4–5	2.02e-03 \pm 4.16e-05 (2.1) \pm 1.29e-04 (6.4)	2.03e-03 \pm 6.77e-05
5–6	8.63e-04 \pm 1.89e-05 (2.2) \pm 5.15e-05 (6.0)	9.00e-04 \pm 3.58e-05
6–7	3.67e-04 \pm 9.50e-06 (2.6) \pm 2.21e-05 (6.0)	3.80e-04 \pm 1.64e-05
7–8	1.80e-04 \pm 5.80e-06 (3.2) \pm 1.08e-05 (6.0)	1.63e-04 \pm 1.16e-05
8–9	8.91e-05 \pm 3.61e-06 (4.1) \pm 5.28e-06 (5.9)	9.49e-05 \pm 7.18e-06
9–10	4.78e-05 \pm 2.50e-06 (5.2) \pm 3.30e-06 (6.9)	4.88e-05 \pm 5.24e-06
10–11	2.86e-05 \pm 1.78e-06 (6.2) \pm 1.84e-06 (6.4)	–
11–12	1.64e-05 \pm 1.26e-06 (7.7) \pm 1.09e-06 (6.6)	–
10–12	2.24e-05 \pm 1.08e-06	2.26e-05 \pm 2.05e-06
12–15	7.58e-06 \pm 4.73e-07 (6.2) \pm 4.86e-07 (6.4)	–
15–20	1.55e-06 \pm 1.49e-07 (9.7) \pm 1.26e-07 (8.1)	–

Table 14: J/ ψ invariant yield in various p_T intervals for $2.5 < y < 4$ in 0–20% centrality class and compared to the 2015 analysis. The total statistics are quadratical sum of the statistical uncertainties on the J/ ψ signal extraction and acceptance efficiency.

p_T (GeV/c)	$d^2N_{\text{AA}}/dydp_T \pm (\text{stat}) (\%) (\text{GeV}/c^{-1})$ (CL)	2015 data
0–0.3	1.50e-03 \pm 9.18e-05 (6.1) \pm 9.09e-05 (6.1)	–
0.3–1	3.99e-03 \pm 1.02e-04 (2.6) \pm 2.20e-04 (5.5)	4.02e-03 \pm 1.95e-04 \pm 2.21e-04
1–2	5.58e-03 \pm 1.05e-04 (1.9) \pm 2.96e-04 (5.3)	5.40e-03 \pm 1.75e-04 \pm 2.57e-04
2–3	4.06e-03 \pm 7.97e-05 (2.0) \pm 2.14e-04 (5.3)	4.05e-03 \pm 1.09e-04 \pm 2.11e-04
3–4	2.03e-03 \pm 3.32e-05 (1.6) \pm 1.11e-04 (5.5)	2.06e-03 \pm 5.57e-05 \pm 9.21e-05
4–5	9.04e-04 \pm 1.61e-05 (1.8) \pm 4.76e-05 (5.3)	9.32e-04 \pm 2.93e-05 \pm 4.92e-05
5–6	4.02e-04 \pm 8.69e-06 (2.2) \pm 2.01e-05 (5.0)	4.03e-04 \pm 1.71e-05 \pm 1.70e-05
6–7	2.01e-04 \pm 5.04e-06 (2.5) \pm 1.01e-05 (5.0)	2.16e-04 \pm 1.10e-05 \pm 1.04e-05
7–8	9.72e-05 \pm 3.06e-06 (3.1) \pm 4.92e-06 (5.1)	9.65e-05 \pm 6.05e-06 \pm 4.70e-06
8–9	4.88e-05 \pm 1.99e-06 (4.1) \pm 2.62e-06 (5.4)	–
9–10	2.66e-05 \pm 1.45e-06 (5.5) \pm 1.34e-06 (5.0)	–
10–11	1.45e-05 \pm 9.72e-07 (6.7) \pm 7.33e-07 (5.0)	–
11–12	1.04e-05 \pm 8.62e-07 (8.3) \pm 5.74e-07 (5.5)	–
8–12	2.51e-05 \pm 6.96e-07(2.8)	2.40e-05 \pm 1.25e-06 \pm 1.03e-06
12–15	3.82e-06 \pm 2.90e-07 (7.6) \pm 2.47e-07 (6.5)	–
15–20	9.78e-07 \pm 1.01e-07 (10.3) \pm 5.09e-08 (5.2)	–

Table 15: J/ ψ invariant yield in various p_T intervals for $2.5 < y < 4$ in 20–40% centrality class and compared to the 2015 analysis. The total statistics are quadratical sum of the statistical uncertainties on the J/ ψ signal extraction and acceptance efficiency.

386 obtained with the Run 2 total statistics (2015+2018), is compatible with the 2015 published measurement,
387 provide more accurate measurements and allows to reach $p_T = 20$ GeV/c. One can however note that
388 the 2015+2018 results are systematically below the 2015 ones for $p_T > 4$ GeV/c, which is the direct
389 consequence of the deviation observed at high- p_T between the two measurements of the pp reference

p_T (GeV/ c)	$d^2N_{AA}/dydp_T \pm (\text{stat})\% (\text{GeV}/c^{-1})$ (CL)	2015 data
0–0.3	5.53e-04 \pm 1.39e-05 (2.5) \pm 2.92e-05 (5.3)	–
0.3–1	5.78e-04 \pm 1.57e-05 (2.7) \pm 3.05e-05 (5.3)	5.63e-04 \pm 2.80e-05 \pm 3.20e-05
1–2	8.34e-04 \pm 1.43e-05 (1.7) \pm 4.02e-05 (4.8)	8.26e-04 \pm 2.63e-05 \pm 4.12e-05
2–3	6.08e-04 \pm 1.02e-05 (1.7) \pm 2.92e-05 (4.8)	6.32e-04 \pm 1.79e-05 \pm 3.00e-05
3–4	3.55e-04 \pm 5.60e-06 (1.6) \pm 1.87e-05 (5.3)	3.50e-04 \pm 9.56e-06 \pm 1.74e-05
4–5	1.70e-04 \pm 3.00e-06 (1.8) \pm 8.39e-06 (4.9)	1.69e-04 \pm 5.55e-06 \pm 7.49e-06
5–6	8.41e-05 \pm 1.80e-06 (2.1) \pm 3.84e-06 (4.6)	7.87e-05 \pm 3.17e-06 \pm 3.34e-06
6–7	4.24e-05 \pm 1.07e-06 (2.5) \pm 1.93e-06 (4.6)	3.92e-05 \pm 1.94e-06 \pm 1.67e-06
7–8	2.03e-05 \pm 6.52e-07 (3.2) \pm 9.77e-07 (4.8)	2.08e-05 \pm 1.16e-06 \pm 8.77e-07
8–9	1.14e-05 \pm 4.60e-07 (4.0) \pm 6.08e-07 (5.3)	–
9–10	5.70e-06 \pm 3.07e-07 (5.4) \pm 2.54e-07 (4.5)	–
10–11	3.25e-06 \pm 2.20e-07 (6.8) \pm 2.39e-07 (7.4)	–
11–12	1.88e-06 \pm 1.57e-07 (8.4) \pm 9.39e-08 (5.0)	–
8–12	$5.56e-06 \pm 1.54e-07(2.77)$	$5.18e-06 \pm 2.87e-07 \pm 2.19e-07$
12–15	1.03e-06 \pm 6.68e-08 (6.5) \pm 9.52e-08 (9.2)	–
15–20	2.00e-07 \pm 2.51e-08 (12.6) \pm 2.30e-08 (11.5)	–

Table 16: J/ψ invariant yield in various p_T intervals for $2.5 < y < 4$ in 40–90% centrality class and compared to the 2015 analysis. The total statistics are quadratical sum of the statistical uncertainties on the J/ψ signal extraction and acceptance efficiency.

cross section (2015 versus 2017 samples). After detailed cross checks of the pp analyses, the observed deviation was attributed to statistical fluctuations of the data in the 2015 sample. The R_{AA} exhibits a flat p_T dependence in the high p_T region for $p_T > 6$ GeV/ c . The correlated uncertainties in the 2015+2018 results are slightly larger because of the normalization factor uncertainty. Concerning the point to point uncorrelated uncertainties, the reduced uncertainties in the 2015+2018 data sample are due to the reduced uncorrelated systematic uncertainties on the pp reference in the 2017 data sample, and also to the fact that we did not include the statistical uncertainty on the pp cross section as a point to point uncorrelated uncertainty versus p_T in the R_{AA} measurement (contrary to what was done in the 2015 analysis). For the 20–40%, 40–90% centrality classes, their R_{AA} values are compared with the 2015 data published results [12] in Fig. 32 and 33, respectively. Note that the acceptance efficiency with the tuned MC input shape in 20–40% and 40–90% centrality bins are used. The main difference between the published results for both centrality bins comes from the pp reference.

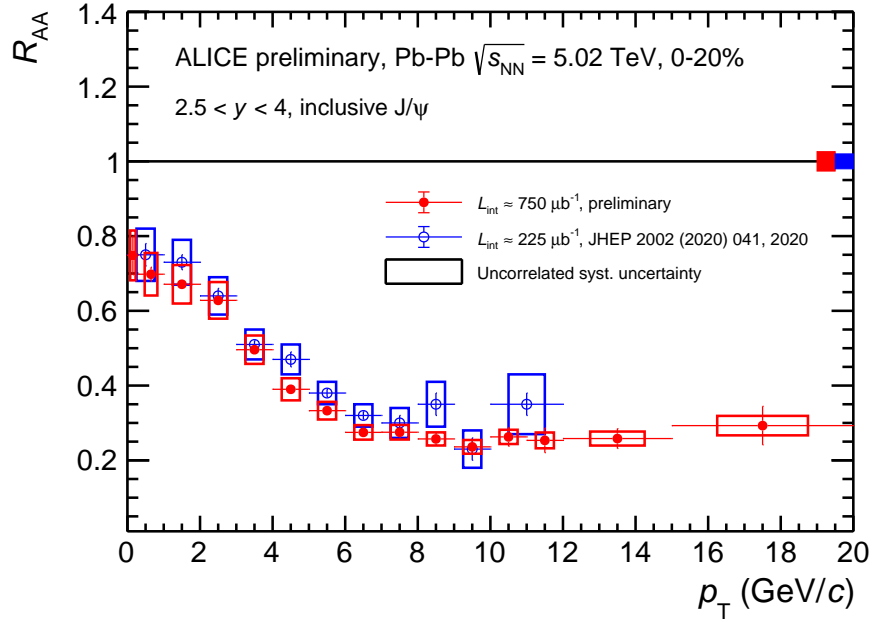


Fig. 31: J/ ψ R_{AA} as a function of p_T for $2.5 < y < 4$ in 0–20% centrality class compared to the 2015 analysis. The global uncertainty is 2.5% for the 2015+2018 and 2015 analyses.

p_T (GeV/c)	$R_{\text{AA}} \pm (\text{stat}) (\%) \pm (\text{syst}) (\%) (\text{CL})$	2015 data
0–0.3	$0.74 \pm 0.05 (6.9) \pm 0.07 (8.8)$	–
0.3–1	$0.70 \pm 0.02 (2.5) \pm 0.06 (8.0)$	–
0–1	–	$0.75 \pm 0.03 (4.0) \pm 0.07 (9.3)$
1–2	$0.67 \pm 0.01 (1.6) \pm 0.05 (7.5)$	$0.73 \pm 0.02 (2.7) \pm 0.06 (8.2)$
2–3	$0.63 \pm 0.01 (1.6) \pm 0.05 (7.7)$	$0.64 \pm 0.02 (3.1) \pm 0.05 (7.8)$
3–4	$0.50 \pm 0.01 (2.2) \pm 0.04 (7.5)$	$0.51 \pm 0.01 (2.0) \pm 0.04 (7.8)$
4–5	$0.39 \pm 0.01 (2.5) \pm 0.03 (7.4)$	$0.47 \pm 0.02 (4.3) \pm 0.04 (8.5)$
5–6	$0.33 \pm 0.01 (2.9) \pm 0.02 (6.9)$	$0.38 \pm 0.01 (2.6) \pm 0.03 (7.9)$
6–7	$0.28 \pm 0.01 (3.6) \pm 0.02 (6.9)$	$0.32 \pm 0.01 (3.1) \pm 0.03 (9.4)$
7–8	$0.28 \pm 0.01 (4.7) \pm 0.02 (6.9)$	$0.30 \pm 0.02 (6.7) \pm 0.04 (13.3)$
8–9	$0.26 \pm 0.02 (6.0) \pm 0.02 (6.7)$	$0.35 \pm 0.03 (8.6) \pm 0.06 (17.1)$
9–10	$0.24 \pm 0.02 (7.9) \pm 0.02 (7.6)$	$0.23 \pm 0.03 (13.0) \pm 0.05 (21.7)$
10–11	$0.26 \pm 0.03 (9.5) \pm 0.02 (7.1)$	–
11–12	$0.25 \pm 0.03 (12.9) \pm 0.02 (8.2)$	–
10–12	–	$0.35 \pm 0.03 (8.6) \pm 0.08 (22.9)$
12–15	$0.26 \pm 0.03 (10.2) \pm 0.02 (7.1)$	–
15–20	$0.29 \pm 0.05 (17.6) \pm 0.03 (8.8)$	–

Table 17: J/ ψ R_{AA} in various p_T intervals for $2.5 < y < 4$ in 0–20% centrality class and compared to the 2015 analysis. The total statistics are quadratical sum of the statistical uncertainties on the J/ ψ signal extraction, the acceptance efficiency and the pp reference. The global uncertainty (not included) is 2.6% and 2% for the 2015+2018 analysis and the 2015 analysis, respectively.

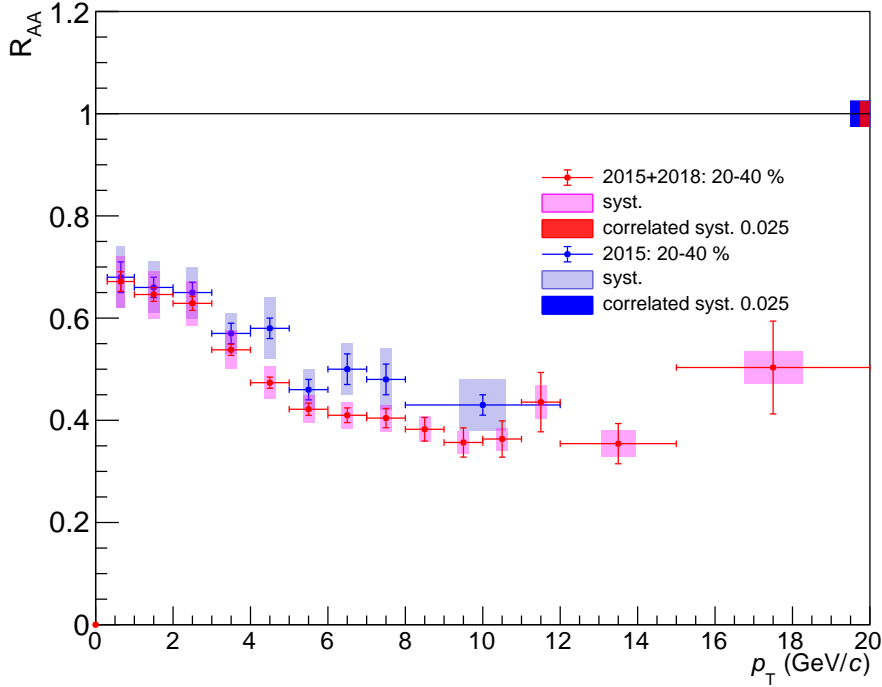


Fig. 32: $\text{J}/\psi R_{\text{AA}}$ as a function of p_{T} for $2.5 < y < 4$ in 20–40% centrality class and compared to the 2015 analysis [12]. The global uncertainties are 2% for the 2015+2018 and 2015 analyses.

p_{T} (GeV/c)	$R_{\text{AA}} \pm (\text{stat}) (\%) \pm (\text{syst}) (\%) (\text{CL})$	2015 data
0.3–1	$0.67 \pm 0.02 (2.9) \pm 0.05 (7.5)$	$0.68 \pm 0.03 (4.1) \pm 0.06 (8.8)$
1–2	$0.65 \pm 0.01 (2.1) \pm 0.05 (7.2)$	$0.66 \pm 0.02 (3.0) \pm 0.05 (7.6)$
2–3	$0.63 \pm 0.01 (2.2) \pm 0.04 (6.9)$	$0.65 \pm 0.02 (3.1) \pm 0.05 (7.7)$
3–4	$0.54 \pm 0.01 (2.02) \pm 0.04 (6.9)$	$0.57 \pm 0.02 (3.5) \pm 0.04 (7.0)$
4–5	$0.47 \pm 0.01 (2.32) \pm 0.03 (6.7)$	$0.58 \pm 0.02 (3.4) \pm 0.06 (10.3)$
5–6	$0.42 \pm 0.01 (2.85) \pm 0.03 (6.35)$	$0.46 \pm 0.02 (4.3) \pm 0.04 (8.7)$
6–7	$0.41 \pm 0.01 (3.5) \pm 0.03 (6.26)$	$0.50 \pm 0.03 (6.0) \pm 0.05 (10.0)$
7–8	$0.40 \pm 0.02 (4.6) \pm 0.03 (6.4)$	$0.48 \pm 0.03 (6.3) \pm 0.06 (12.5)$
8–9	$0.38 \pm 0.02 (6.0) \pm 0.02 (6.4)$	–
9–10	$0.36 \pm 0.03 (8.0) \pm 0.02 (6.2)$	–
10–11	$0.36 \pm 0.04 (9.8) \pm 0.02 (6.1)$	–
11–12	$0.44 \pm 0.06 (13.3) \pm 0.03 (7.5)$	–
8–12	–	$0.43 \pm 0.02 (4.7) \pm 0.05 (11.6)$
12–15	$0.35 \pm 0.04 (11.1) \pm 0.03 (7.3)$	–
15–20	$0.50 \pm 0.09 (18.0) \pm 0.03 (6.4)$	–

Table 18: $\text{J}/\psi R_{\text{AA}}$ in various p_{T} intervals for $2.5 < y < 4$ in 20–40% centrality class. The total statistics are quadratical sum of the statistical uncertainties on the J/ψ signal extraction, the acceptance efficiency and the pp reference. The global uncertainty (not included) is 2.5% for the 2015+2018 analysis and the 2015 analysis.

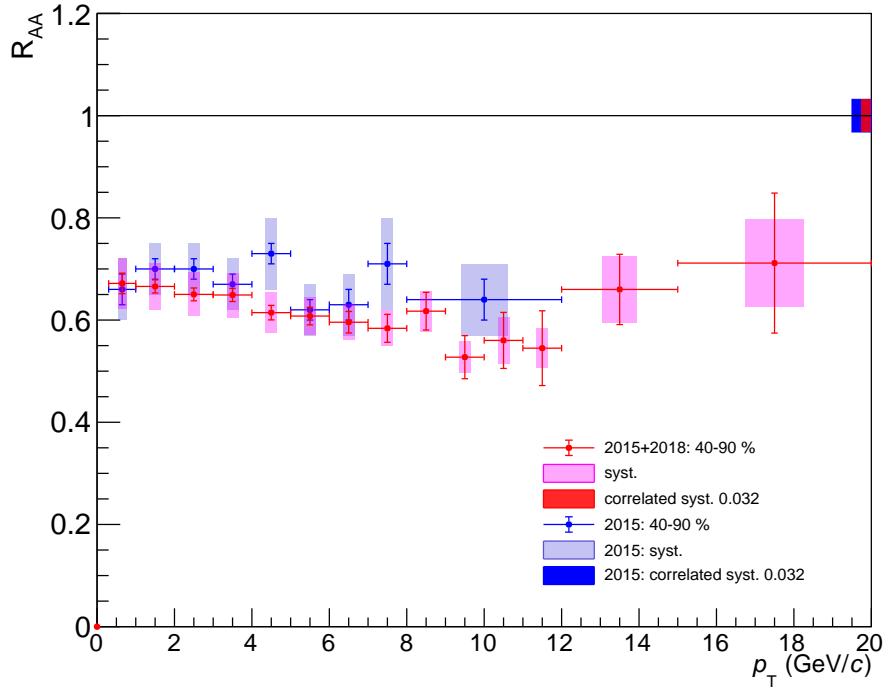


Fig. 33: J/ ψ R_{AA} as a function of p_T for $2.5 < y < 4$ in 40–90% centrality class and compared to the 2015 analysis [12]. The global uncertainties are 3% for the 2015+2018 analysis and the 2015 analysis.

p_T (GeV/c)	$R_{\text{AA}} \pm (\text{stat}) (\%) \pm (\text{syst}) (\%) (\text{CL})$	2015 data
0.3–1	$0.67 \pm 0.02 (3.0) \pm 0.05 (7.3)$	$0.66 \pm 0.03 (4.5) \pm 0.06 (9.1)$
1–2	$0.67 \pm 0.01 (1.9) \pm 0.05 (6.8)$	$0.70 \pm 0.02 (2.9) \pm 0.05 (7.1)$
2–3	$0.65 \pm 0.01 (1.9) \pm 0.04 (6.5)$	$0.70 \pm 0.02 (2.9) \pm 0.05 (7.1)$
3–4	$0.65 \pm 0.01 (2.0) \pm 0.04 (6.8)$	$0.67 \pm 0.02 (3.0) \pm 0.05 (7.5)$
4–5	$0.61 \pm 0.01 (2.3) \pm 0.04 (6.4)$	$0.73 \pm 0.02 (2.7) \pm 0.07 (9.6)$
5–6	$0.61 \pm 0.02 (2.8) \pm 0.04 (6.0)$	$0.62 \pm 0.02 (3.2) \pm 0.05 (8.1)$
6–7	$0.60 \pm 0.02 (3.5) \pm 0.04 (5.9)$	$0.63 \pm 0.03 (4.8) \pm 0.06 (9.5)$
7–8	$0.58 \pm 0.03 (4.7) \pm 0.04 (6.0)$	$0.71 \pm 0.04 (5.6) \pm 0.09 (12.7)$
8–9	$0.62 \pm 0.04 (6.0) \pm 0.04 (6.4)$	–
9–10	$0.53 \pm 0.04 (8.0) \pm 0.03 (5.8)$	–
10–11	$0.56 \pm 0.05 (9.8) \pm 0.05 (8.1)$	–
11–12	$0.54 \pm 0.07 (13.4) \pm 0.04 (7.1)$	–
8–12	–	$0.64 \pm 0.04 (6.3) \pm 0.07 (10.9)$
12–15	$0.66 \pm 0.07 (10.4) \pm 0.06 (9.8)$	–
15–20	$0.71 \pm 0.14 (19.2) \pm 0.09 (12.1)$	–

Table 19: J/ ψ R_{AA} in various p_T intervals for $2.5 < y < 4$ in 40–90% centrality class. The total statistics are quadratical sum of the statistical uncertainties on the J/ ψ signal extraction, the acceptance efficiency and the pp reference. The global uncertainty (not included) is 3.2% for the 2015+2018 analysis and the 2015 analysis, respectively.

402 9 Conclusion

403 We have measured the inclusive J/ψ p_{T} -differential R_{AA} as a function of p_{T} in the 0–20%, 20–40%
404 and 40–90% centrality classes in the 2015+2018 Pb–Pb datasets (Run 2 statistics) at $\sqrt{s_{\text{NN}}} = 5.02 \text{ TeV}$.
405 The previous measurements (2015) have been extended up to $p_{\text{T}} = 20 \text{ GeV}/c$. In the 0–20% centrality
406 interval, the R_{AA} shows a flat p_{T} dependence for $p_{\text{T}} > 6 \text{ GeV}/c$. In this version of the AN, the p_{T}
407 dependence of R_{AA} in the 20–40% centrality interval is similar to the previous measurements (2015).
408 Furthermore, the p_{T} dependence of R_{AA} in the 40–90% centrality interval is also similar to the previous
409 measurements and overall it is flat as a function of p_{T} for this centrality range. In the three centrality
410 ranges, the main differences in the comparison between the published 2015 data and those results come
411 from the pp reference used (2017 pp reference in this work and 2015 pp reference with less statistics for
412 2015 published data).

413 **10 Plots for preliminary**

414 The plots requested to be preliminary plots for HP in 2020 are the J/ ψ R_{AA} as a function of p_T for
 415 20–40%, 40–90% centrality intervals, and J/ ψ invariant yield as a function of p_T for the three centrality
 416 intervals. Those plots are shown in Fig. 34, 35, and 36 respectively.

417

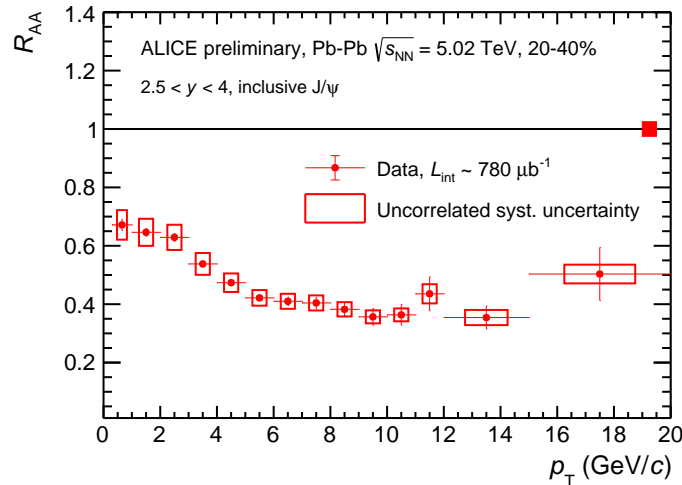


Fig. 34: J/ ψ R_{AA} as a function of p_T for $2.5 < y < 4$ in 20–40% centrality class. The global uncertainty is 2.5% for the Run 2 analyses.

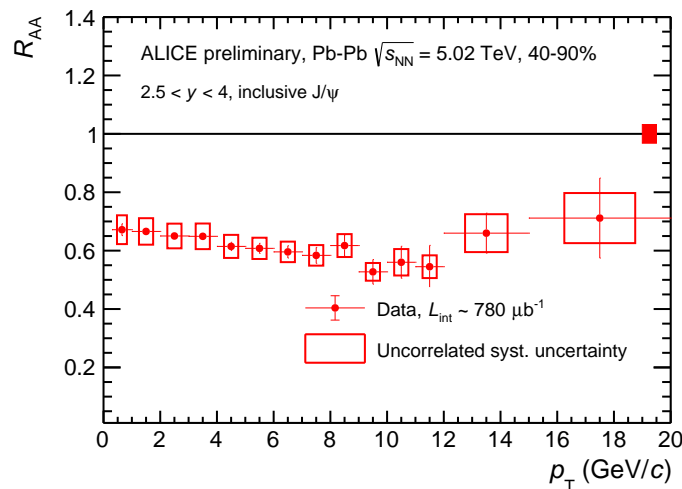


Fig. 35: J/ ψ R_{AA} as a function of p_T for $2.5 < y < 4$ in 40–90% centrality class. The global uncertainty is 3.2% for the Run 2 analysis.

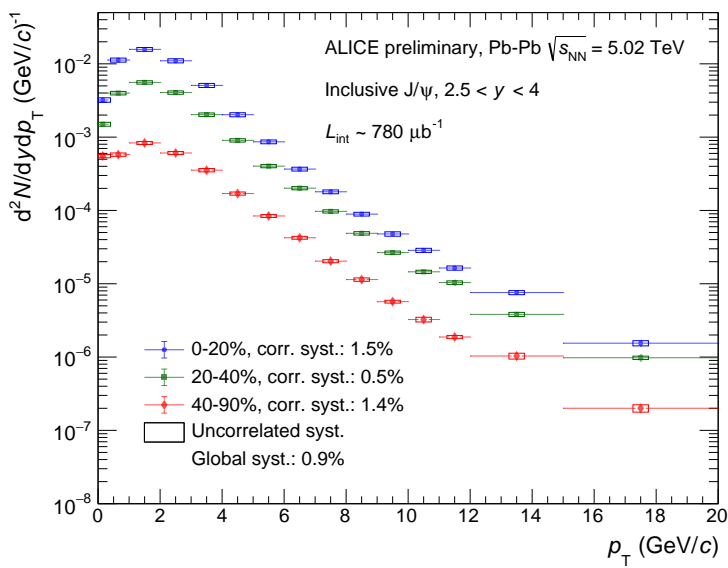


Fig. 36: J/ψ invariant yield as a function of p_T for $2.5 < y < 4$ in 0–20% (blue), 20–40% (green) and 40–90% (red) centrality classes. The correlated systematic uncertainty over p_T is written for each centrality range. The global uncertainty is 0.9% and is same for all the three centrality range.

418 **A Graphs of all systematic tests performed on signal extraction in various p_T bins for**
419 **various centrality classes**

420 The fit test which fails reaching the criteria of fitting have been removed from the figures. For the
421 successful fittings, the weights consequently changes in order to have the same weight between pp data
422 tail and MC tail parameters.

423 **0–20% centrality class:**

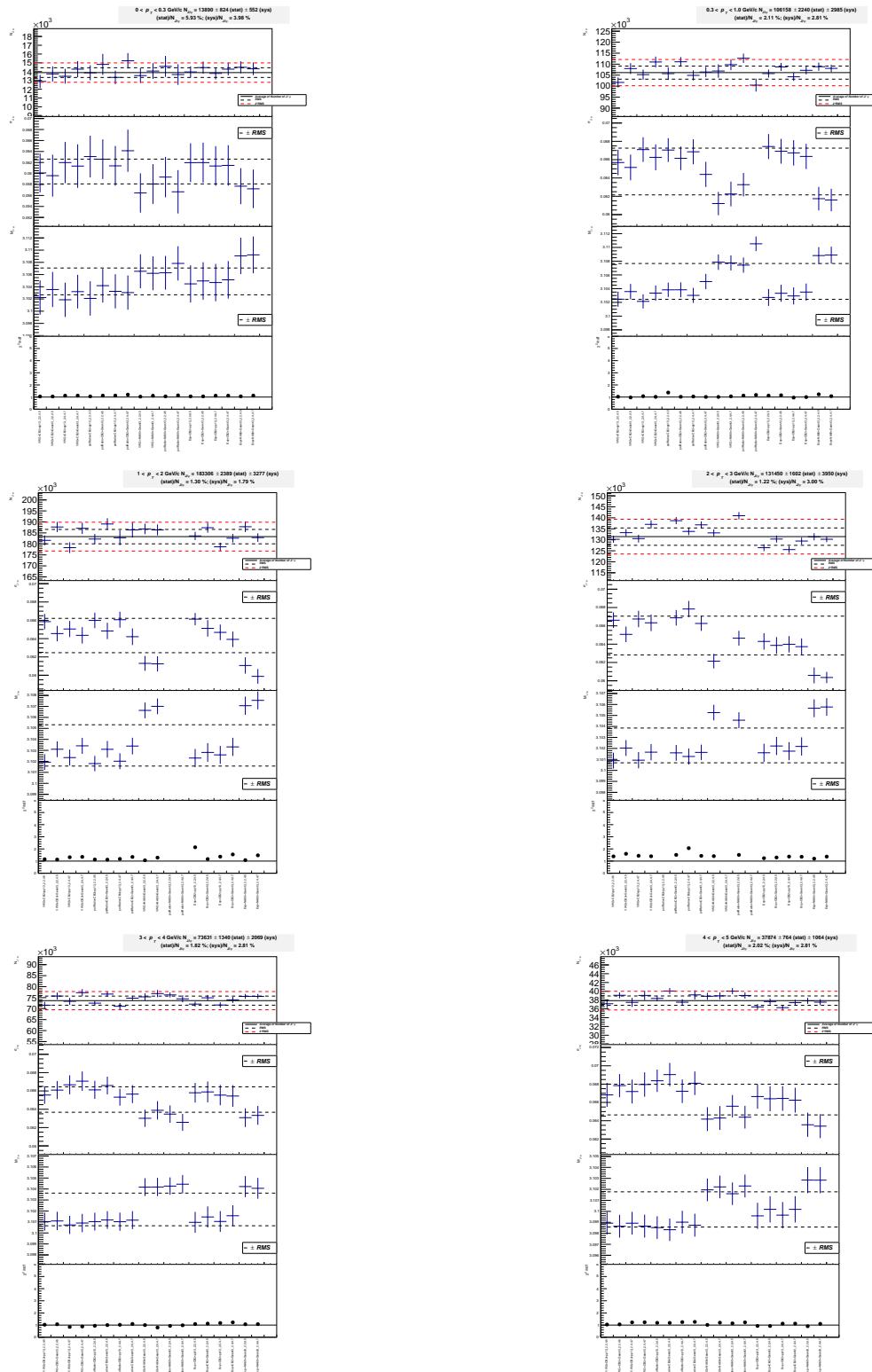


Fig. A.1: Graphs of all systematic tests performed on signal extraction for various p_T bins from 0 to 5 GeV/c .

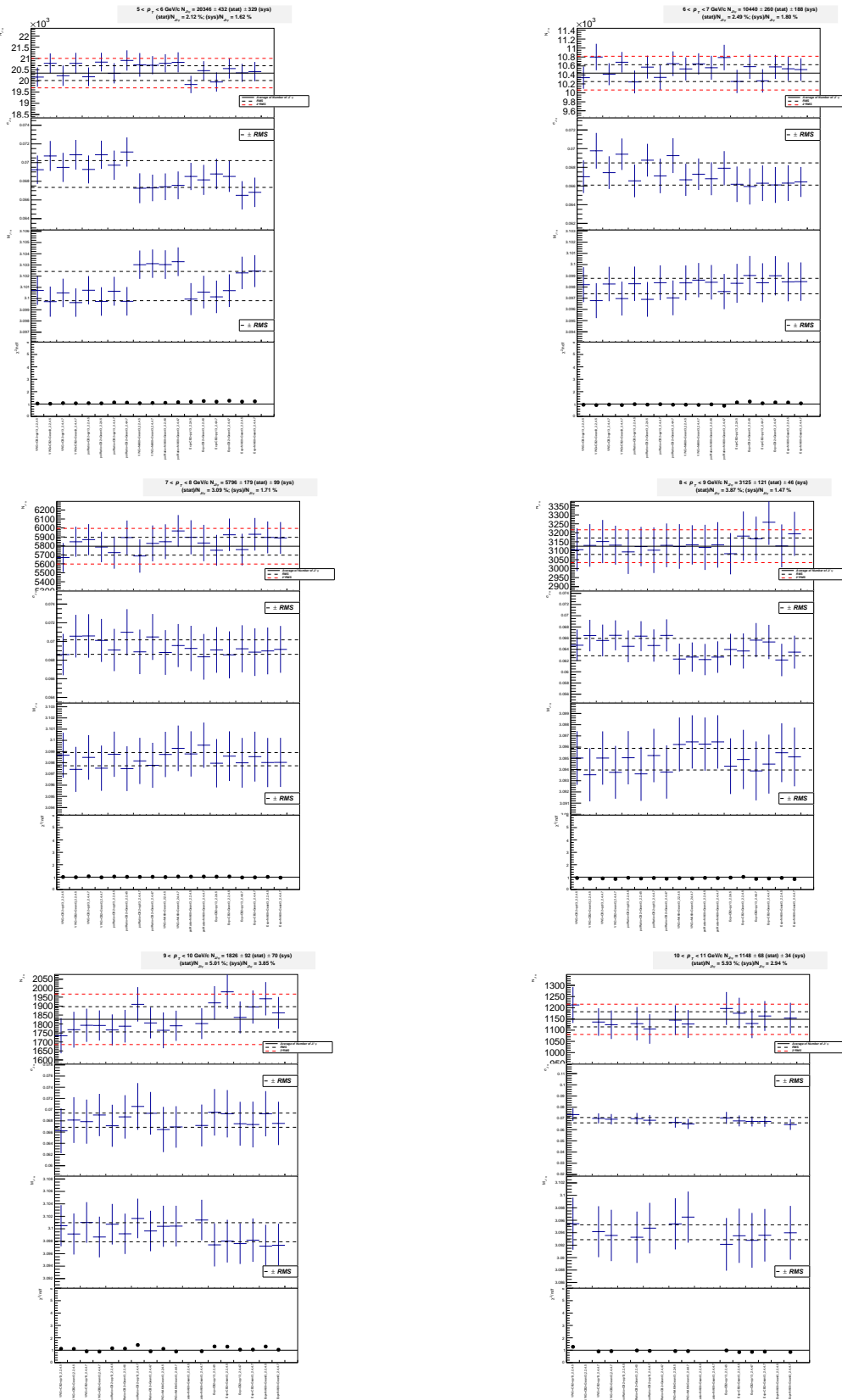


Fig. A.2: Graphs of all systematic tests performed on signal extraction for various p_T bins from 5 to 11 GeV/c .

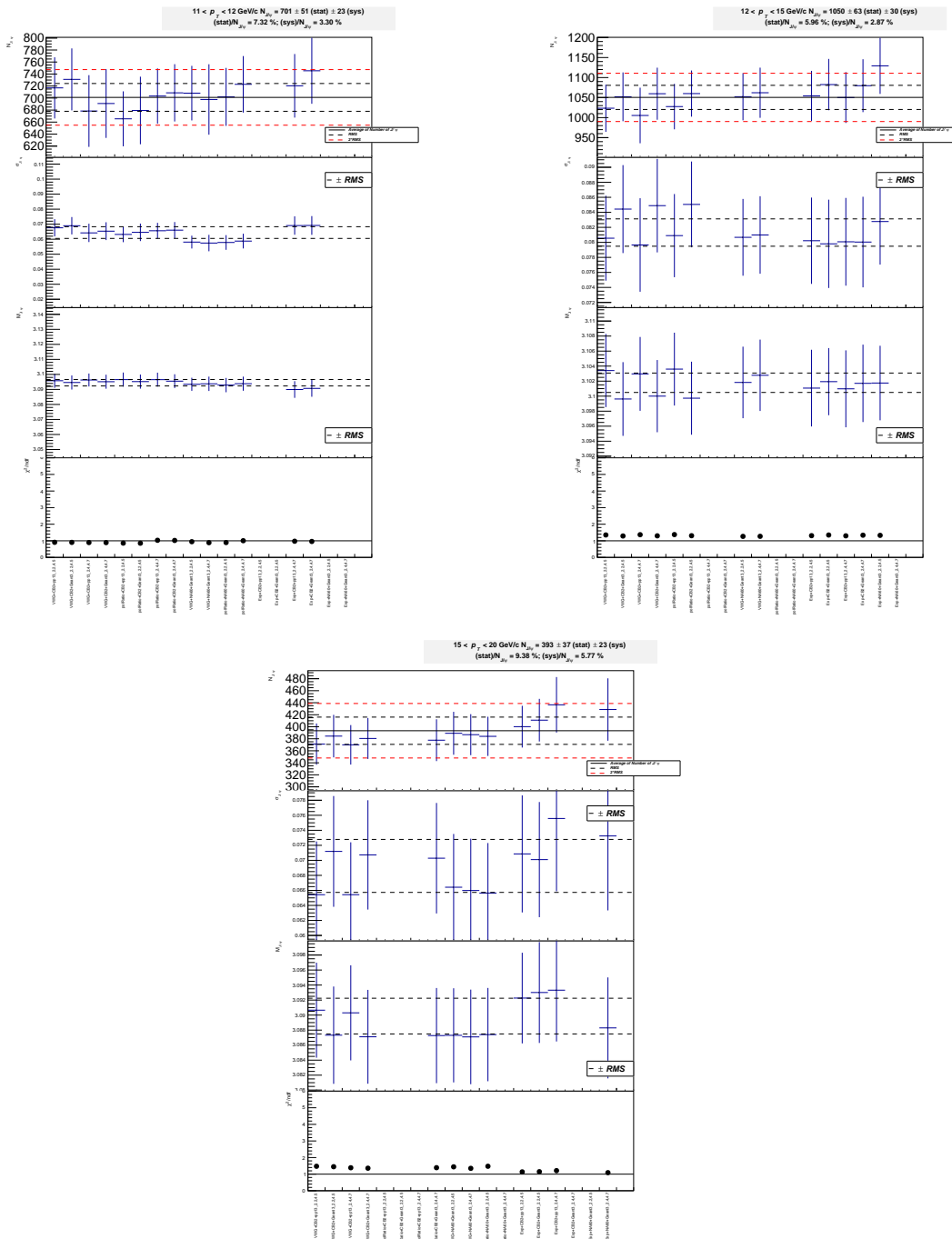
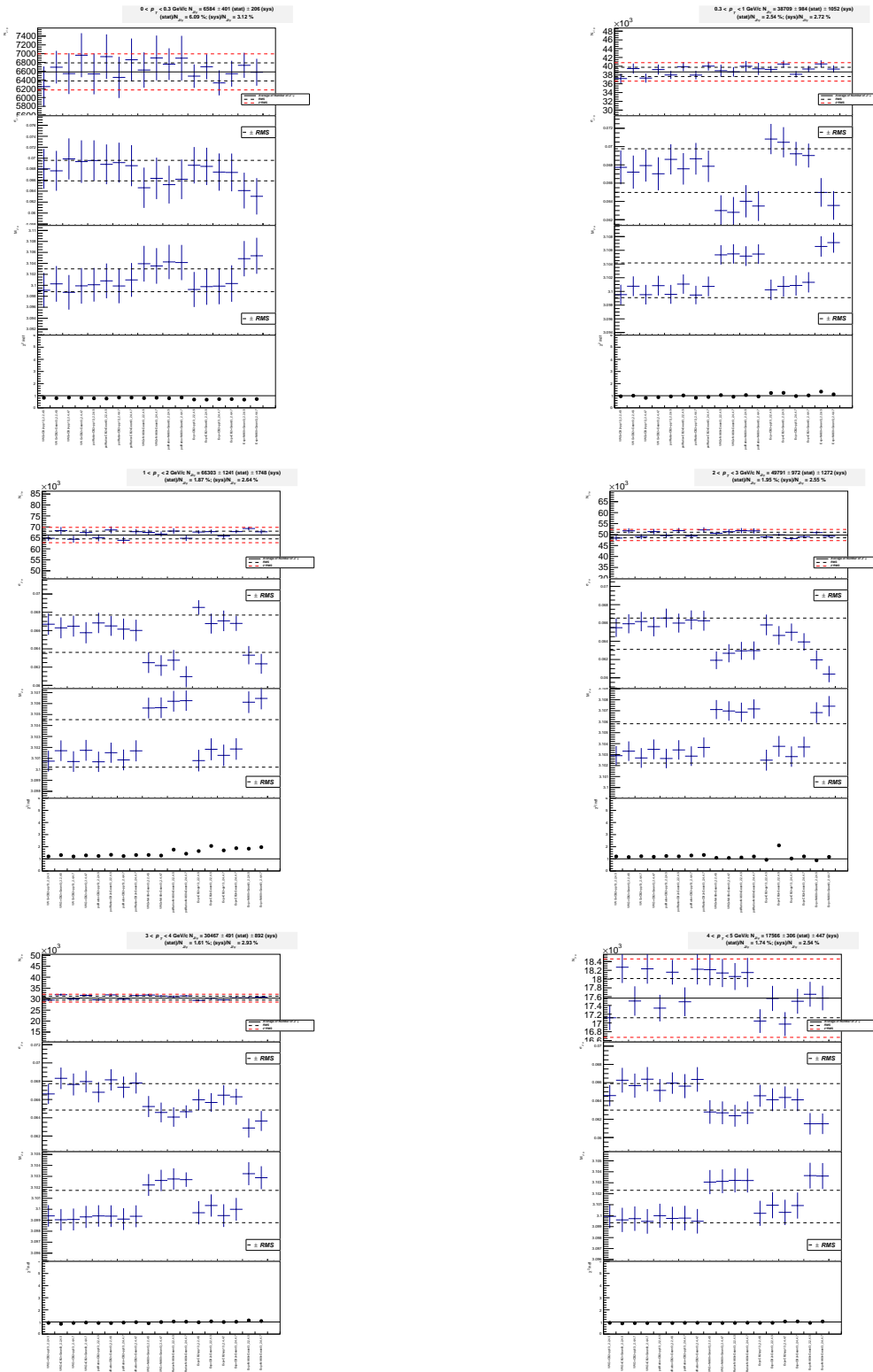


Fig. A.3: Graphs of all systematic tests performed on signal extraction for various p_T bins from 11 to 20 GeV/c .

20–40% centrality class:

**Fig. A.4:** Graphs of all systematic tests performed on signal extraction for various p_T bins from 0 to 5 GeV/c .

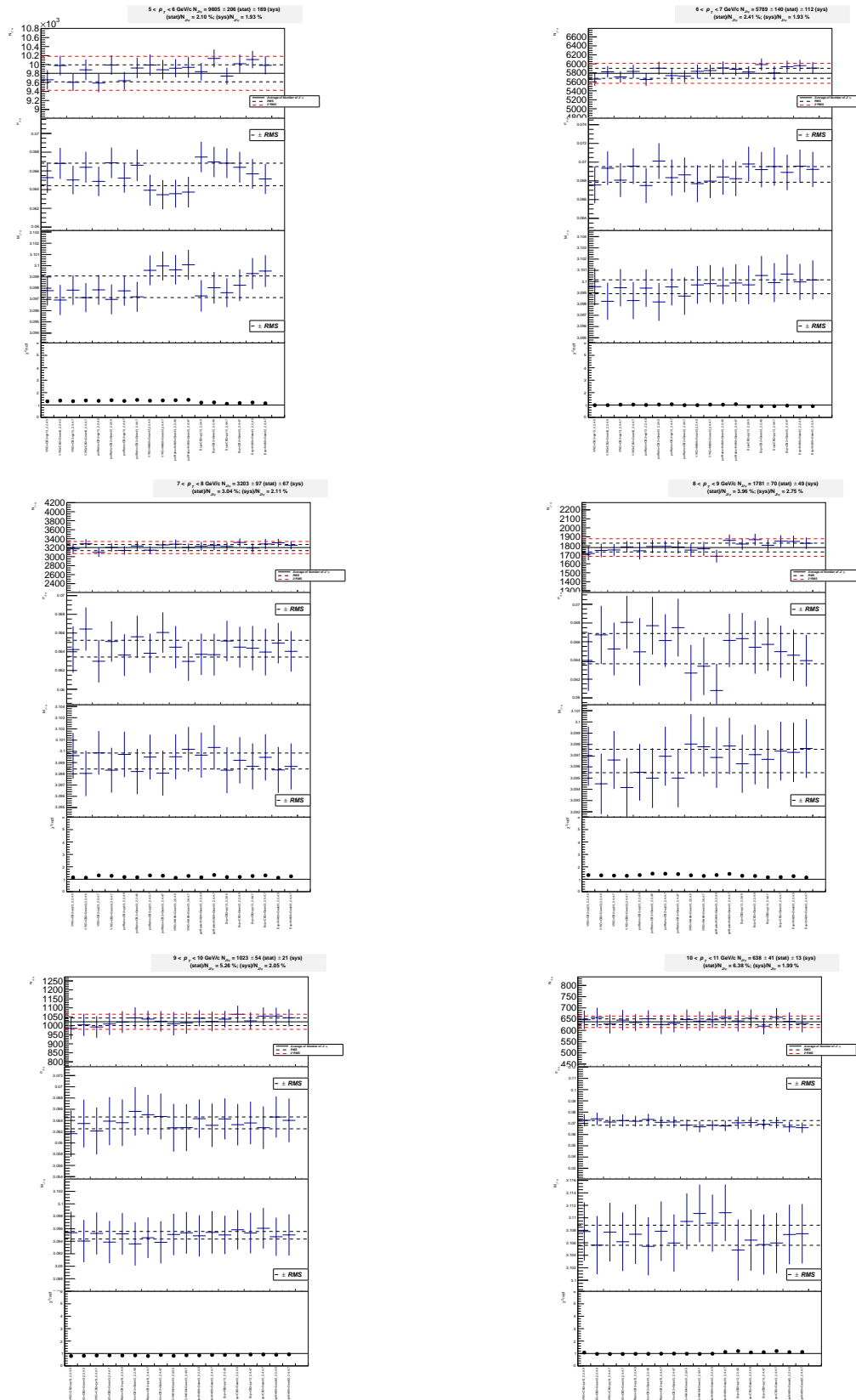


Fig. A.5: Graphs of all systematic tests performed on signal extraction for various p_T bins from 5 to 11 GeV/c .

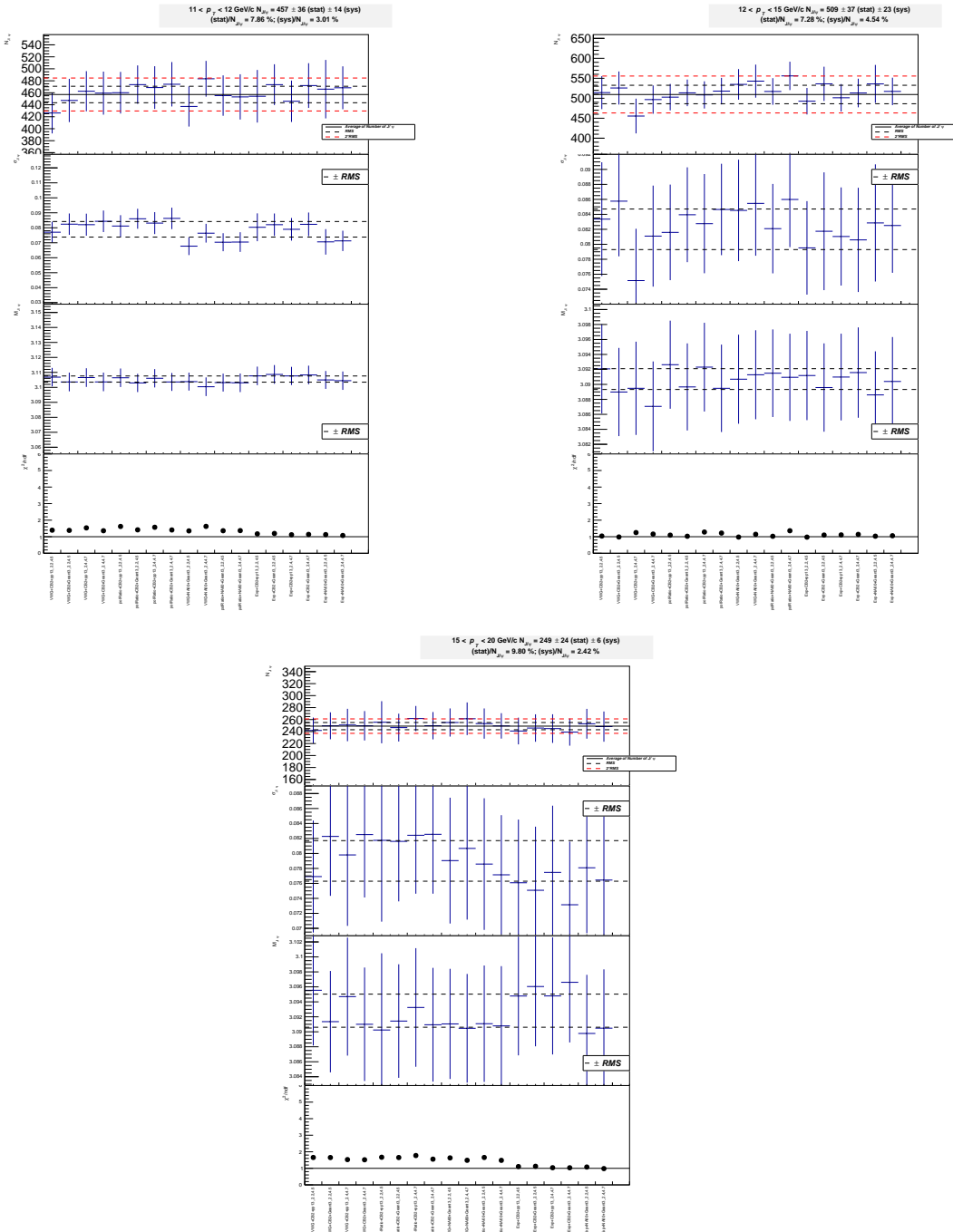


Fig. A.6: Graphs of all systematic tests performed on signal extraction for various p_T bins from 11 to 20 GeV/c .

40–90% centrality class:

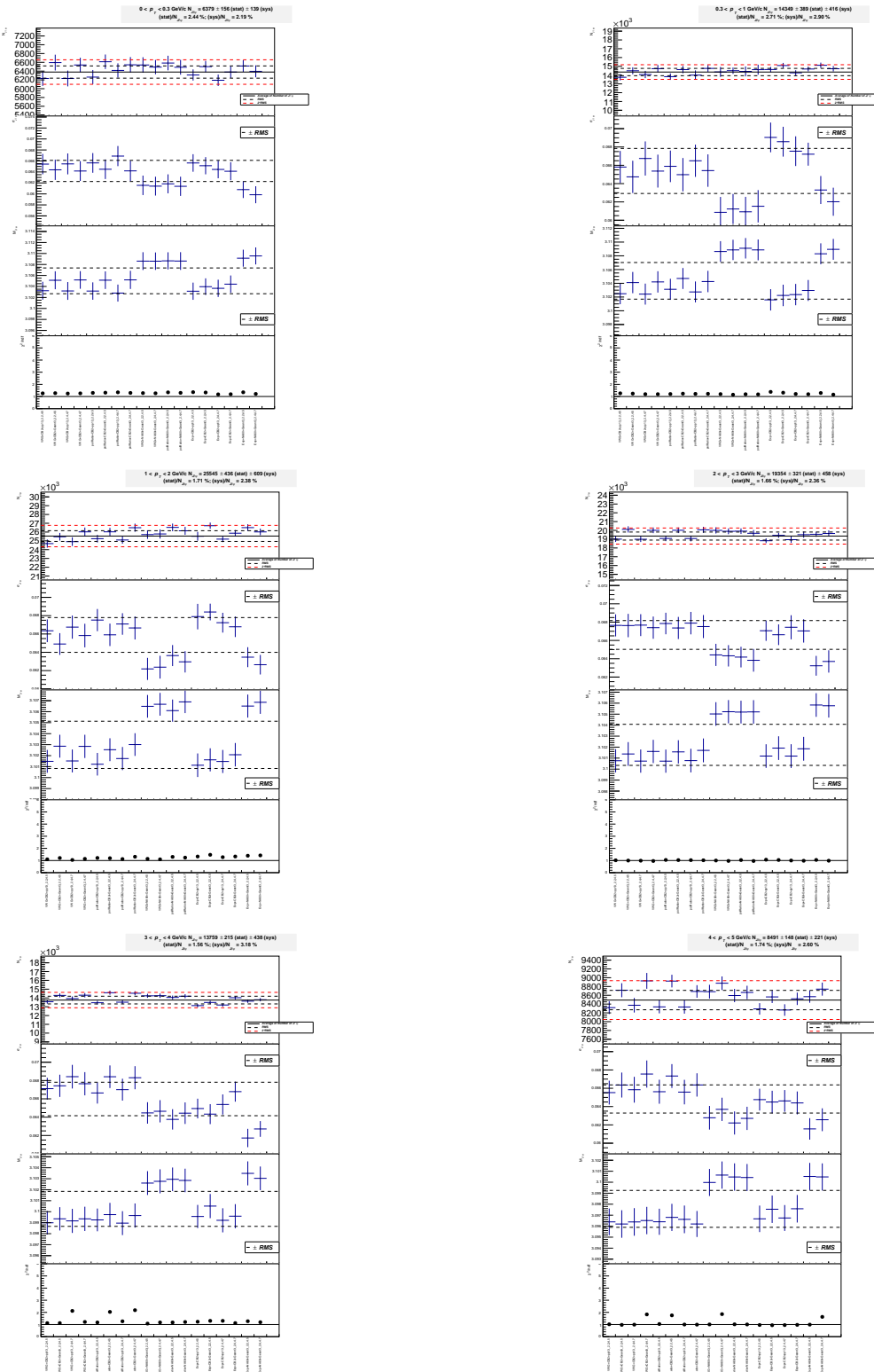


Fig. A.7: Graphs of all systematic tests performed on signal extraction for various p_T bins from 0 to 5 GeV/c.

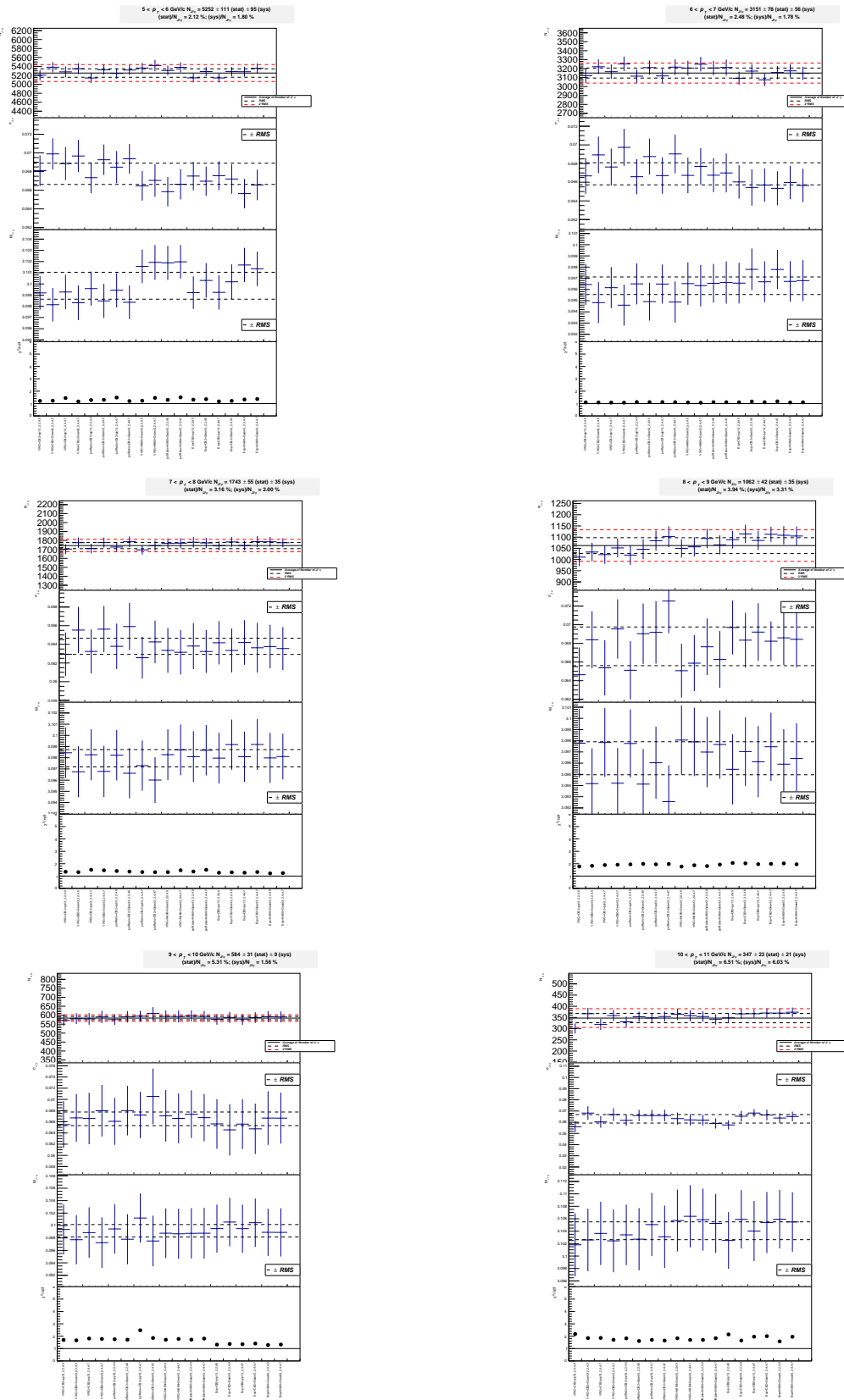


Fig. A.8: Graphs of all systematic tests performed on signal extraction for various p_T bins from 5 to 11 GeV/c .

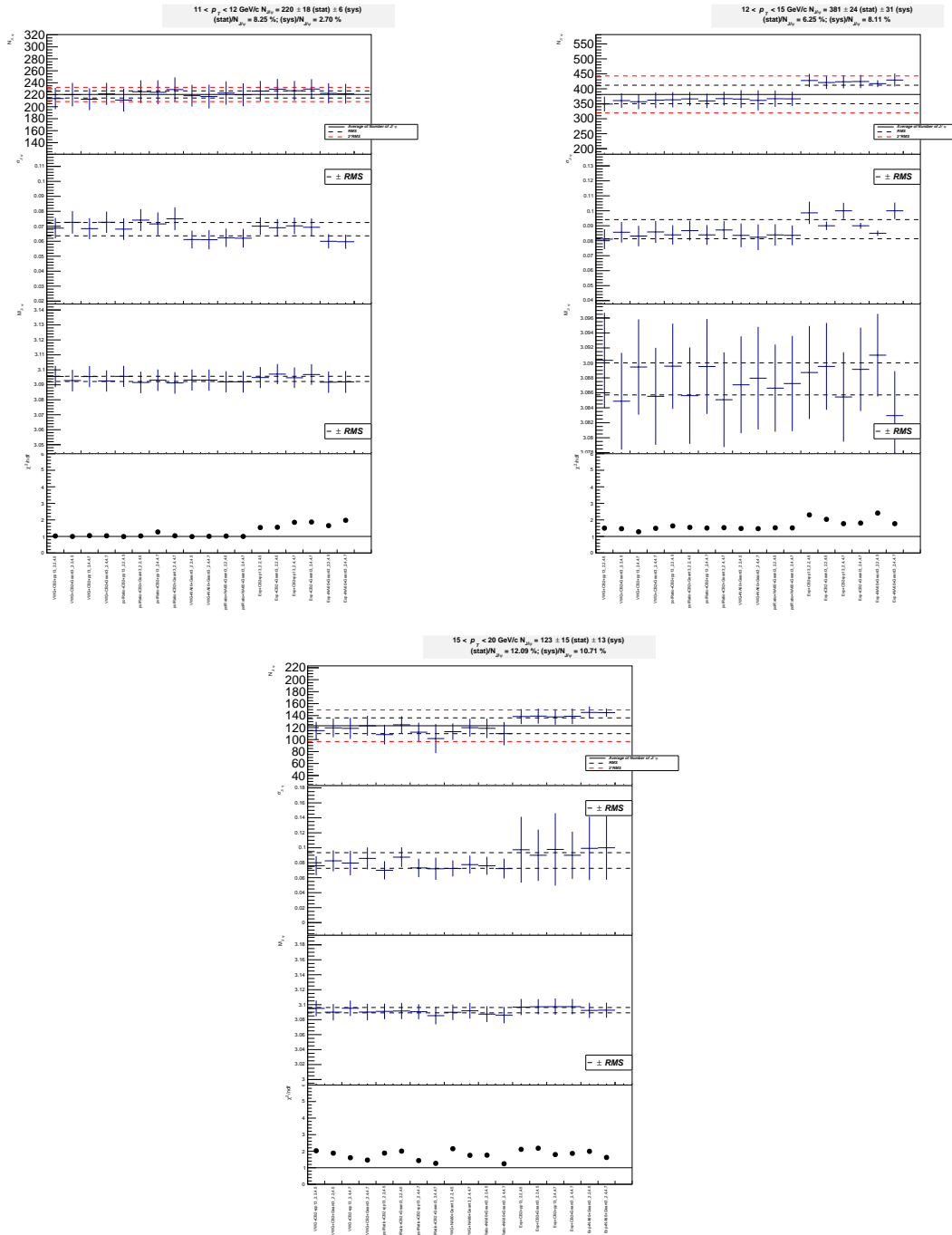


Fig. A.9: Graphs of all systematic tests performed on signal extraction for various p_T bins from 11 to 20 GeV/c.

426 **B Signal function tail parameters**

427 This appendix lists all the function tail parameters which are used for the signal extraction on the merged
428 data. The tail parameters are extracted by fitting the reconstructed J/ ψ in a given p_T bin from the merged
429 embedded MC, LHC16e2, LHC16e2_plus and LHC19a2. The details of fitting functions are described
430 in section 4.

431 The two signal functions are taken from [1].

432 **The extended Crystal Ball (CB2) function** is defined as follows:

$$f(x; N, \bar{x}, \sigma, t_1, t_2, p_1, p_2) = N \cdot \begin{cases} A \cdot (B - t)^{-p_1}, & t \leq t_1 \\ \exp(-\frac{1}{2}t^2), & t_1 < t < t_2 \\ C \cdot (D + t)^{-p_2}, & t \geq t_2 \end{cases}$$

where

$$\begin{aligned} t &= \frac{x - \bar{x}}{\sigma} \\ A &= \left(\frac{p_1}{|t_1|}\right)^{p_1} \cdot \exp\left(-\frac{|t_1|^2}{2}\right) \\ B &= \frac{p_1}{|t_1|} - |t_1| \\ C &= \left(\frac{p_2}{|t_2|}\right)^{p_2} \cdot \exp\left(-\frac{|t_2|^2}{2}\right) \\ D &= \frac{p_2}{|t_2|} - |t_2| \end{aligned}$$

The NA60 function is defined as follows:

$$f(x; N, \bar{x}, \sigma, t_1, t_2, p_1, \dots, p_6) = N \cdot \exp\left(-\frac{1}{2}\left(\frac{t}{t_0}\right)^2\right)$$

where

$$t = \frac{x - \bar{x}}{\sigma}$$

433 and

$$t_0 = \begin{cases} 1 + (p_1(t_1 - t))^{p_2 - p_3\sqrt{t_1 - t}}, & t \leq t_1 \\ 1, & t_1 < t < t_2 \\ 1 + (p_4(t - t_2))^{p_5 - p_6\sqrt{t - t_2}}, & t \geq t_2 \end{cases}$$

434 The tables below show the parameter values that are used for fitting with the two signal functions.

p_T (GeV/c)	t_1	p_1	t_2	p_2
0–0.3	0.858638	4.75501	2.39564	2.98727
0.3–1	0.868405	4.79548	2.33271	3.21768
1–2	0.905241	4.43764	2.27224	3.11843
2–3	0.947708	3.81769	2.21367	3.12354
3–4	0.99405	3.33908	2.24532	2.89599
4–5	1.0403	3.19553	2.22141	3.04096
5–6	1.1121	3.1524	2.17173	3.00136
6–7	1.15302	3.07992	2.10733	3.01155
7–8	1.14585	3.24897	1.97849	3.40429
8–9	1.22804	3.23804	1.9891	3.41379
9–10	1.16759	3.64974	1.9451	3.09714
10–11	1.11029	4.29653	1.82087	2.9752
11–12	1.15395	3.84457	1.97581	2.2759
12–15	1.25662	3.77059	1.74842	2.91646
15–20	1.39855	3.08345	2.08449	1.52249
0–12	0.947348	3.95428	2.2598	2.99278
0–20	0.948307	3.95177	2.26146	2.96375

Table B.1: Signal tail parameters for crystal ball functions. The tail is extracted for $2.2 < m_{\mu\mu} < 4.5$ GeV/c 2

p_T (GeV/c)	t_1	p_1	t_2	p_2
0–0.3	0.859069	4.74966	2.3952	2.98897
0.3–1	0.856975	5.02211	2.32967	3.21829
1–2	0.888613	4.71713	2.26606	3.13384
2–3	0.927825	4.0684	2.20707	3.13788
3–4	0.980496	3.47151	2.24094	2.90626
4–5	1.03441	3.24756	2.22022	3.04136
5–6	1.09746	3.27716	2.16939	3.00034
6–7	1.14352	3.15667	2.10713	3.00362
7–8	1.12367	3.4459	1.97517	3.40243
8–9	1.21117	3.38108	1.9857	3.41876
9–10	1.17766	3.54081	1.94713	3.09206
10–11	1.07806	4.74863	1.81225	2.99831
11–12	1.12526	4.17953	1.9658	2.30136
12–15	1.23354	4.01809	1.75107	2.88354
15–20	1.39392	3.13096	2.10209	1.47488
0–12	0.93185	4.15725	2.249	3.04118
0–20	0.932833	4.15389	2.25013	3.01511

Table B.2: Signal tail parameters for crystal ball functions. The tail is extracted for $2.4 < m_{\mu\mu} < 4.7$ GeV/c 2

p_T (GeV/c)	p_1	p_2	p_3	p_4	p_5	p_6	t_1	t_2
0–0.3	0.227844	1.19712	0.0580133	0.18059	1.42656	0.159209	-0.375907	2.32339
0.3–1	0.22253	1.17787	0.0471578	0.0155434	0.958522	0.405112	-0.265771	2.1229
1–2	0.225255	1.1517	0.0396723	0.182678	1.40039	0.111366	-0.422348	2.14517
2–3	0.226637	1.18106	0.0431824	0.187605	1.39856	0.116916	-0.476256	2.13196
3–4	0.228273	1.23285	0.0548562	0.183291	1.42959	0.109851	-0.535736	2.04047
4–5	0.218256	1.34578	0.0779883	0.175326	1.48574	0.111163	-0.399143	1.85323
5–6	0.213125	1.34341	0.0738626	0.181365	1.37334	0.0855587	-0.501682	1.95567
6–7	0.226716	1.2436	0.0610855	0.1824	1.39921	0.0938813	-0.906812	1.89735
7–8	0.226668	1.18554	0.0460065	0.183082	1.52498	0.166031	-0.958171	1.75937
8–9	0.194649	1.47218	0.0956228	0.173678	1.33928	0.040727	-0.354529	1.57951
9–10	0.212385	1.37996	0.104611	0.194831	1.07251	-0.0152409	-0.817693	2.06744
10–11	0.206401	1.16172	0.0293803	0.196967	1.13884	0.000906145	-0.657045	1.74469
11–12	0.232892	0.978057	-0.00522759	0.129342	2.25677	0.17092	-1.00596	-0.999999
12–15	0.198959	1.45539	0.120246	0.200891	1.08304	-0.0149148	-0.725192	1.73634
15–20	0.213429	1.26738	0.0665217	0.178276	1.59638	0.0702053	-1.11842	0.912538
0–12	0.224267	1.19868	0.0486047	0.183418	1.38359	0.09798	-0.453045	2.11392
0–20	0.224213	1.19923	0.0487403	0.183674	1.37646	0.0952221	-0.454648	2.117761

Table B.3: Signal tail parameters for NA60 functions. The tail is extracted for $2.2 < m_{\mu\mu} < 4.5$ GeV/ c^2

p_T (GeV/c)	p_1	p_2	p_3	p_4	p_5	p_6	t_1	t_2
0–0.3	0.229042	1.18206	0.0544107	0.0204168	0.944891	0.403649	-0.402107	2.37018
0.3–1	0.216573	1.26112	0.0681674	0.17607	1.54893	0.155772	-0.128272	2.04701
1–2	0.218613	1.25881	0.0688342	0.0120016	0.828705	0.357007	-0.270536	2.21767
2–3	0.220074	1.29358	0.0746722	0.187532	1.39988	0.11705	-0.326089	2.12744
3–4	0.220095	1.36597	0.0905219	0.183121	1.42975	0.109254	-0.351072	2.03241
4–5	0.208868	1.50425	0.118152	0.0102309	0.8468	0.357886	-0.174185	1.95037
5–6	0.204915	1.49886	0.115279	0.00910112	0.775677	0.33325	-0.292239	2.03727
6–7	0.221633	1.36469	0.0991189	0.182409	1.38923	0.0900907	-0.779748	1.89998
7–8	0.213008	1.47069	0.130561	0.181965	1.54844	0.170563	-0.607696	1.70784
8–9	0.19358	1.52744	0.115096	0.17454	1.30577	0.030592	-0.321634	1.62322
9–10	0.202575	1.58219	0.158377	0.194799	1.07274	-0.0150415	-0.554627	2.05797
10–11	0.179121	1.78469	0.199183	0.197241	1.13388	0.000151176	0.197016	1.73148
11–12	0.232147	1.0039	0.00441948	0.129297	2.26358	0.172422	-0.987715	-0.999983
12–15	0.177301	2.10834	0.307633	0.200544	1.11466	-0.00473842	-0.0294971	1.70083
15–20	0.208771	1.41034	0.117804	0.178693	1.57512	0.065096	-0.978568	0.923774
0–12	0.217663	1.30818	0.0783826	0.183411	1.37785	0.0956517	-0.299621	2.1141
0–20	0.21765	1.3085	0.0785074	0.183701	1.36878	0.0922852	-0.302219	2.11987

Table B.4: Signal tail parameters for NA60 functions. The tail is extracted for $2.4 < m_{\mu\mu} < 4.7$ GeV/ c^2

435 C Systematic uncertainty on the trigger efficiency

436 Two sources of systematic uncertainties are taken into account for the systematics uncertainties associated
 437 to the trigger efficiency:

- 438 – Uncertainties on the trigger chambers efficiency maps
- 439 – Differences in the shapes of the trigger response versus p_T between data and MC

440 **Systematic on the efficiency map of the trigger chambers** The systematic uncertainty on the intrinsic
 441 trigger efficiency is 1.5% estimated in the published results on the 2015 Pb-Pb [9]. This contribution is
 442 uncorrelated versus p_T and y and it is correlated versus centrality.

443 444 Systematic due to the trigger response function

445 The standard procedure [7] to evaluate the uncertainty from the trigger response as a function of p_T can
 446 be summarized as follow:

- 447 – First, obtain the muons matching the L_{p_T} trigger or the A_{p_T} trigger in the minimum bias trigger
 448 of data and of realistic MC, where $L_{p_T} = 1 \text{ GeV}/c$ is the low- p_T trigger threshold and $A_{p_T} = 0.5$
 449 GeV/c is the minimum- p_T trigger threshold for which a muon is firing the trigger. Then group
 450 the muons into six groups depending on its local board, according to the geometry in the trigger
 451 chamber plane. Table C.1 shows the local board numbers in six groups and Figure C.6 shows the
 452 geometry of the local boards in the trigger chamber plane. The RF of the p_T distribution of the
 453 six groups are shown in Figure C.1, C.2 and C.3. The same group with the same-size strip pitch
 454 has a similar response function. Grouping local boards with the same RF is expected to reduce
 455 the associated systematics as compared to the systematics obtained by integrating over all local
 456 boards.
- 457 – Fit the response function (RF) obtained as the ratio of the p_T distributions of muons matching the
 458 L_{p_T} trigger over muons matching the A_{p_T} trigger in each group of data and of realistic MC. The
 459 fitting function used is the following:
 460 if $p_T < 2 \text{ GeV}/c$, then

$$461 RF = \frac{L_{p_T}}{A_{p_T}} = p_7 + p_0 \times erf\left[\frac{\max(p_T, p_6)}{\sqrt{2}p_2} - 1\right]. \quad (C.1)$$

462 However, the extra term is added to the RF fitting function if $p_T < p_6$. That extra term is expressed
 463 as:

$$464 RF + p_3 \times \left\{ erf\left[\frac{-1 \times \max(p_T, p_6) - p_4}{\sqrt{2}p_5}\right] - erf\left(\frac{p_6 + p_4}{\sqrt{2}p_5}\right) \right\}. \quad (C.2)$$

465 If $p_T \geq 2 \text{ GeV}/c$, another fitting function is used:

$$466 RF = p_0 + \frac{p_1}{1 + exp[-p_2(p_T - p_3)]} \quad (C.3)$$

467 Note that $p_0, p_1, p_2, \dots, p_7$ are the free parameters. The function \max gives the larger values of
 468 its two arguments. The fitting has to be done for the response functions for the six group for a
 469 given centrality classes. However, as we will see later, the systematics is found to be similar in all
 470 centrality classes and for the final results, the study is carried out integrated over centrality. The
 471 asymmetry uncertainty is considered by using binomial error.

- 469 – Select muons matching the $A p_T$ trigger in J/ ψ MC simulations and weight each of them by either
 470 the data or the MC trigger response function versus p_T given by the above fits:
 471 $w_{\text{data}} = \text{RF}_{\text{data}}(p_T^{\mu 1}) * \text{RF}_{\text{data}}(p_T^{\mu 2})$
 472 $w_{\text{MC}} = \text{RF}_{\text{MC}}(p_T^{\mu 1}) * \text{RF}_{\text{MC}}(p_T^{\mu 2})$
- 473 – Extract the number of reconstructed J/ ψ in the two cases. The difference in the number of recon-
 474 structed J/ ψ gives the systematic uncertainty.
- 475 The systematic uncertainty on the trigger efficiency integrated over p_T , y and centrality is 0.77 %. The
 476 corresponding results for p_T bins for 0–90% centrality class is tabulated in Table C.2, which are used in
 477 this analysis.

Group	Local board number
1	26,27,28,29,48,49,50,51,165,166,167,168,143,144,145,146
2	6,7,8,22,23,24,25,44,45,46,47,9,10,11,30,31,32,33,52,53,54,55,123,124,125, 139,140,141,142,161,162,163,164,169,170,171,172,147,148,149,150,126,127,128
3	215,216,217,218,219,220,199,200,201,202,203,204,183,184,185,186,187,188, 66,67,68,69,70,71,82,83,84,85,86,87,98,99,100,101,102,103
4	213,214,197,198,181,182,159,160,137,138,121,122,4,5,20,21,42,43,64,65,80,81,96,97, 221,222,205,206,189,190,173,174,151,152,129,130,12,13,34,35,56,57,72,73,88,89,104,105
5	211,212,195,196,179,180,157,158,135,136,119,120,2,3,18,19,40,41,62,63,78,79,94,95, 223,224,207,208,191,192,175,176,153,154,131,132,14,15,36,37,58,59,74,75,90,91,106,107
6	1, 16, 17, 39, 61, 77, 93, 109, 109, 110, 111, 112, 113, 114, 115, 116, 117, 108, 92, 76, 60, 38, 133,134,155,156,177,178,193,194,209,225,234,233,232,231,230,229,228,227,226

Table C.1: The local board numbers in six groups according to the geometry of the trigger chamber plane [7].

0–90% centrality	
p_T (GeV/c)	Sys. Unc. (%)
0 – 0.3	2.38
0.3 – 1	1.38
1 – 2	0.14
2 – 3	0.03
3 – 4	0.15
4 – 5	0.15
5 – 6	0.12
6 – 7	0.12
7 – 8	0.13
8 – 9	0.11
9 – 10	0.13
10 – 11	0.13
11 – 12	0.11
12 – 15	0.12
15 – 20	0.12

Table C.2: The systematic uncertainty on trigger efficiency associated to the J/ ψ trigger response as function of p_T for $2.5 < y < 4$ for 0 – 90 % centrality class.

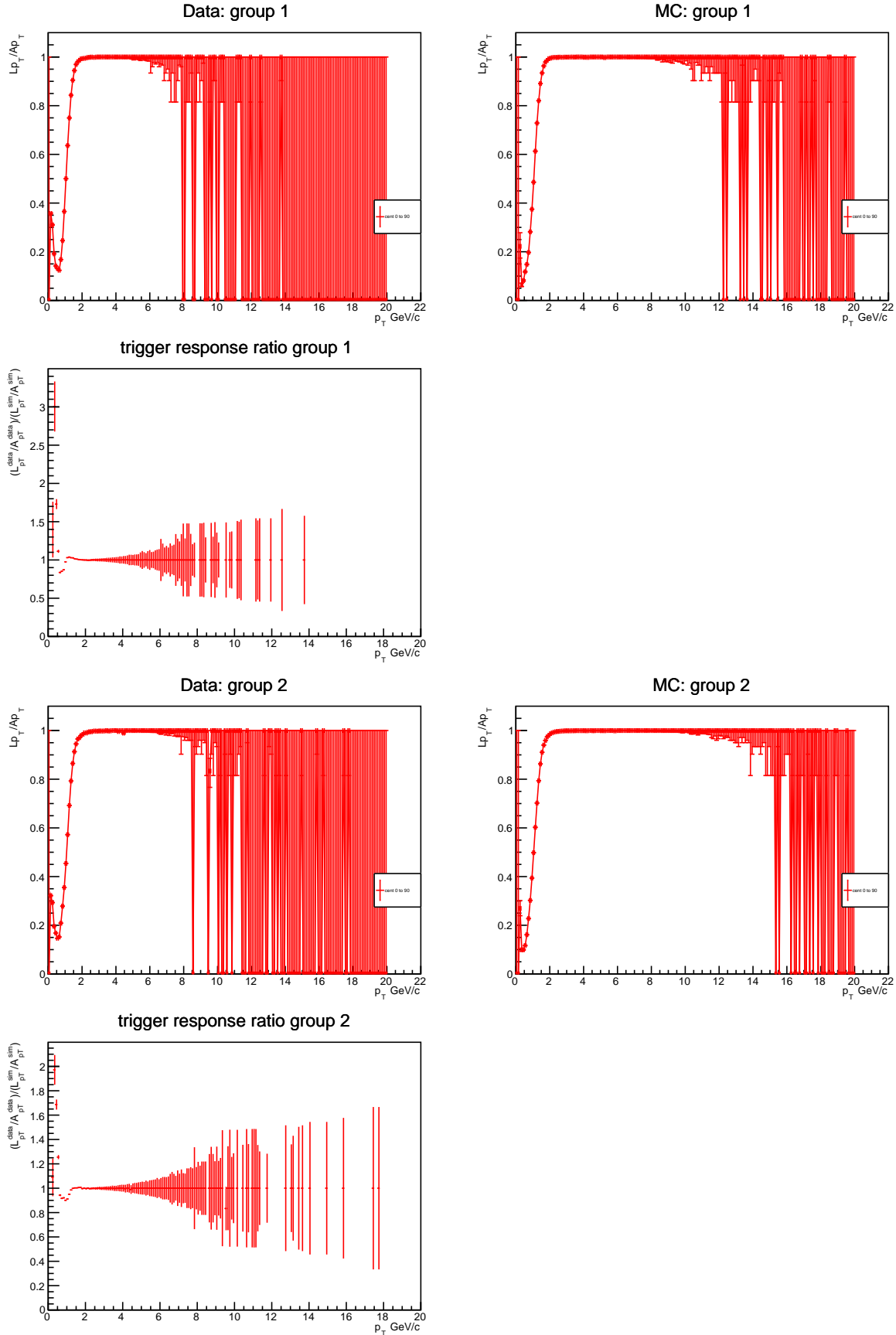


Fig. C.1: The $L_{\text{pT}} / A_{\text{pT}}$ distribution of the first and second groups in data and MC for 0–90% centrality class.

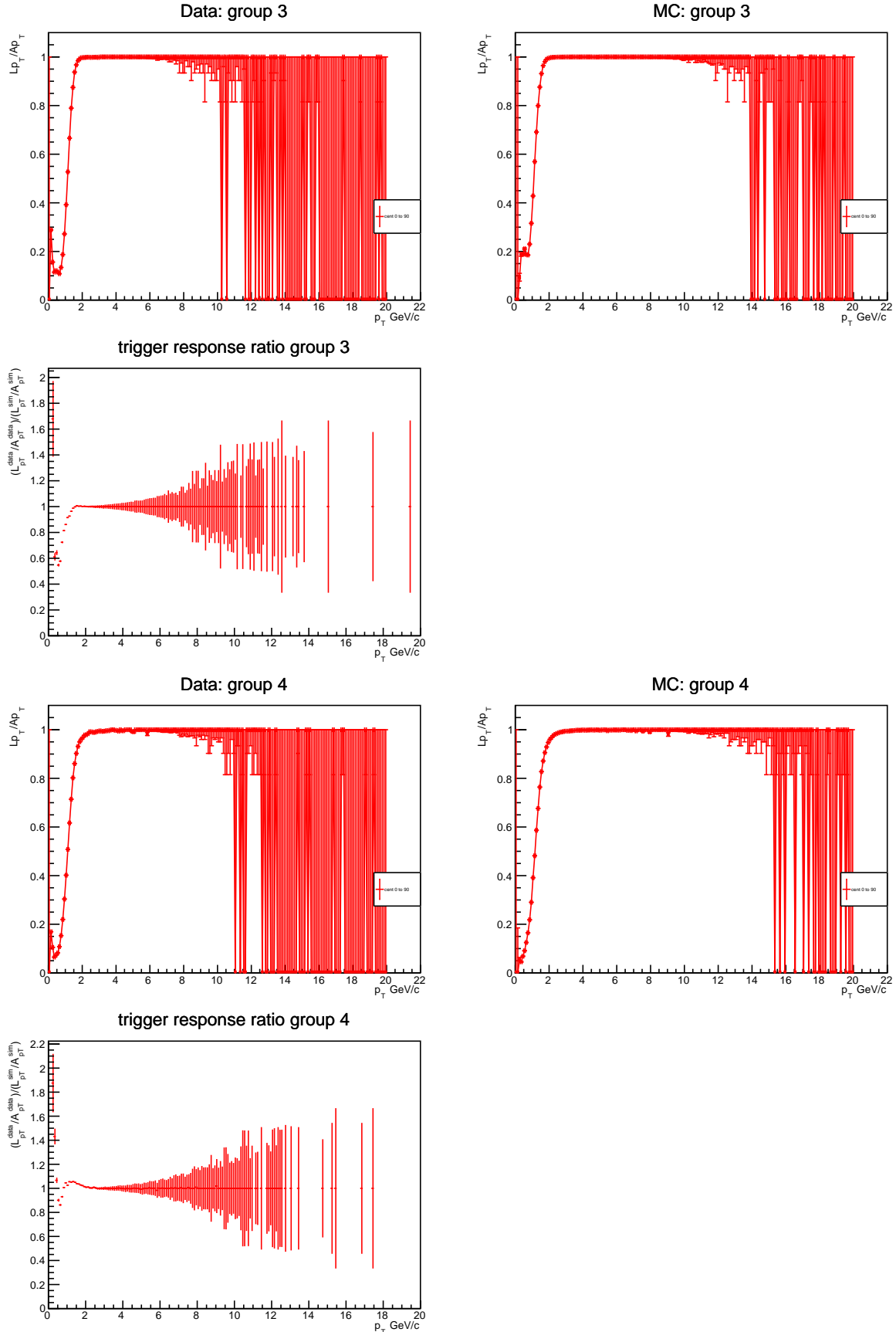


Fig. C.2: The Lp_T / Ap_T distribution of the third and fourth groups in data and MC for 0–90% centrality class.

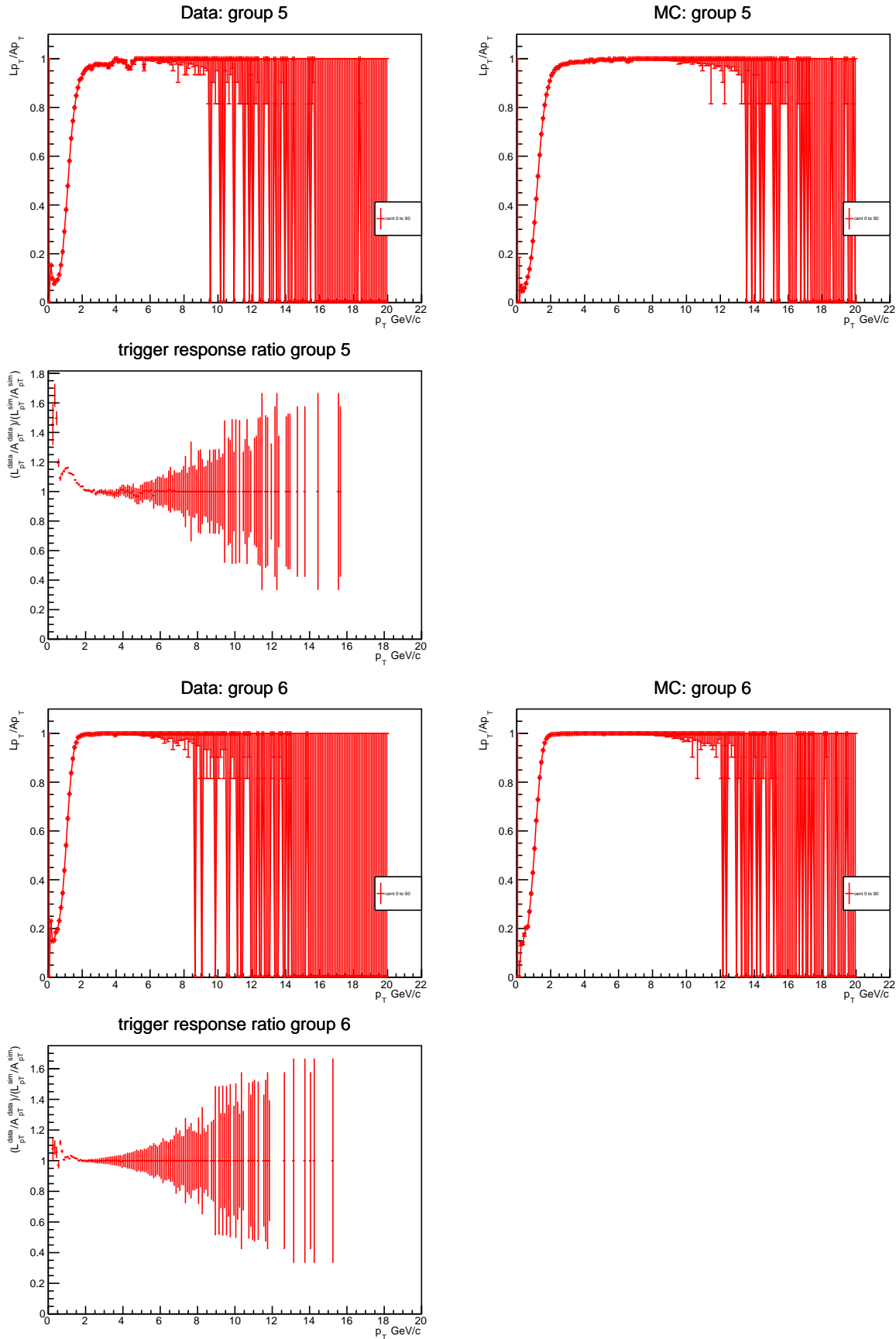


Fig. C.3: The Lp_T / Ap_T distribution of the fifth and sixth groups in data and MC for 0–90% centrality class.

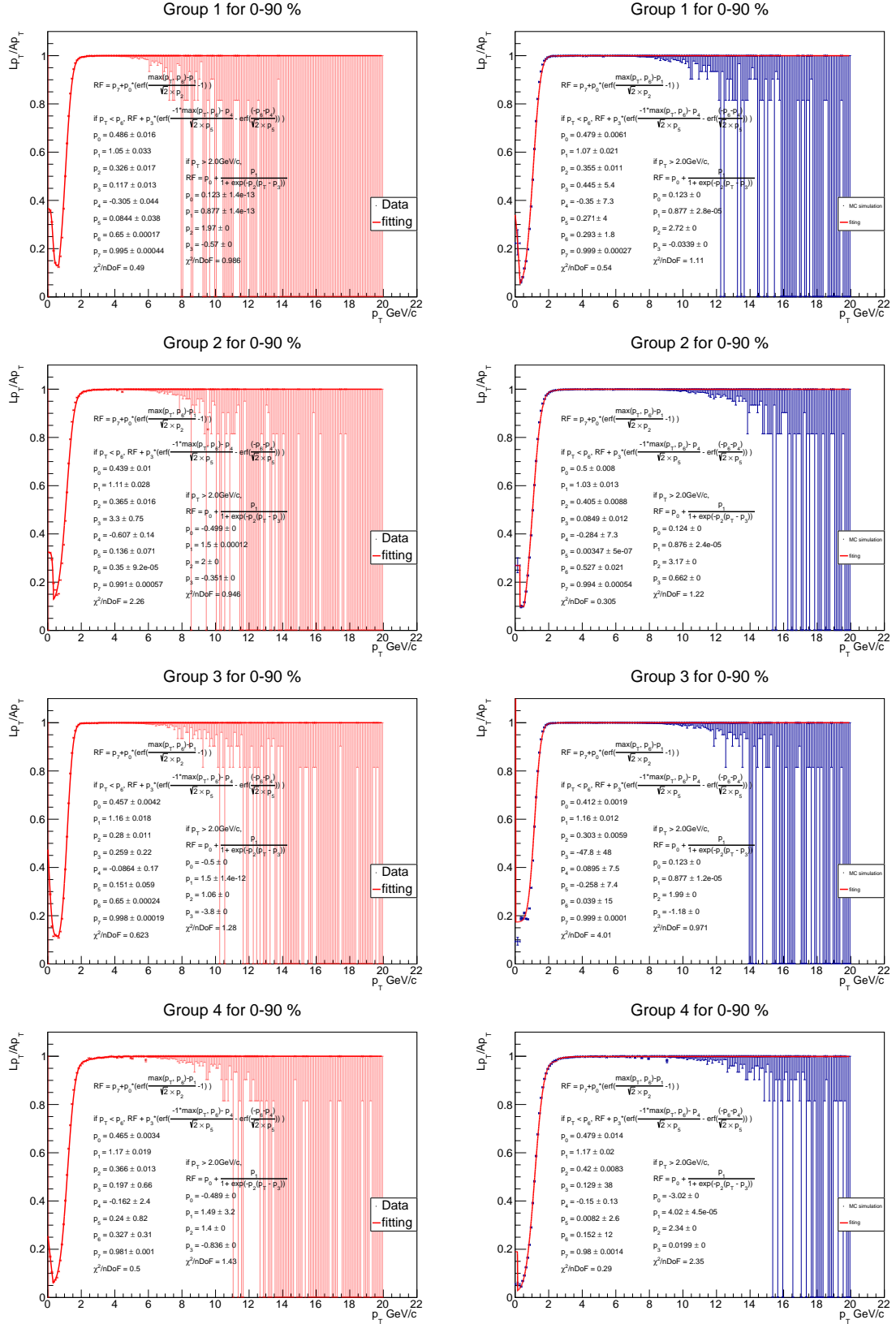


Fig. C.4: The fitting on RF function of the first four groups in data and MC for 0–90% centrality class.

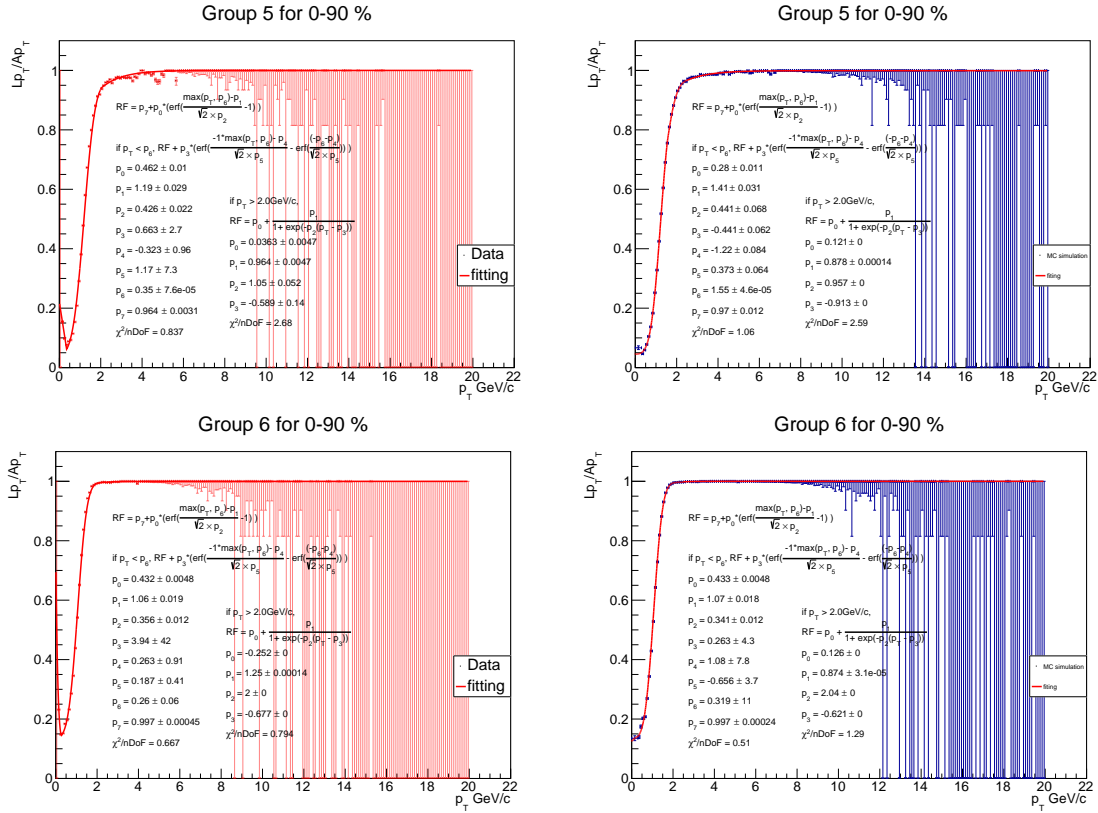


Fig. C.5: The fitting on RF function of the fifth and sixth groups in data and MC for 0–90% centrality class.

05	234	225	209	193	177	155	133	16	38	60	76	92	108	117	04	
9.Out	LC7L9B1	LC6L9B1	LC5L9B1	LC4L9B1	LC3L9B1	LC2L9B1	LC1L9B1	RC1L9B1	RC2L9B1	RC3L9B1	RC4L9B1	RC5L9B1	RC6L9B1	RC7L9B1	09.In	
06	233	224	208	192	176	154	132	15	37	59	75	91	107	116	03	
8.Out	LC7L8B1	LC6L8B1	LC5L8B1	LC4L8B1	LC3L8B1	LC2L8B1	LC1L8B1	RC1L8B1	RC2L8B1	RC3L8B1	RC4L8B1	RC5L8B1	RC6L8B1	RC7L8B1	08.In	
07	222	206	190	174	152	130	13	35	57	73	89	105		115	02	
7.Out	LC7L7B1	LC6L7B1	LC5L7B1	LC4L7B1	LC3L7B1	LC2L7B1	LC1L7B1	RC1L7B1	RC2L7B1	RC3L7B1	RC4L7B1	RC5L7B1	RC6L7B1	RC7L7B1	07.In	
08	220	204	188	172	150	128	11	33	55	71	87	103		114	01	
6.Out	LC6L6B1	LC5L6B1	LC4L6B1	LC3L6B1	LC2L6B1	LC1L6B1	RC1L6B1	RC2L6B1	RC3L6B1	RC4L6B1	RC5L6B1	RC6L6B1	RC7L6B1	06.In		
09	218	202	186	168	146	126	10	32	54	71	85	101		113	00	
5.Out	LC6L5B1	LC5L5B1	LC4L5B1	LC3L5B1	LC2L5B1	LC1L5B1	RC1L5B1	RC2L5B1	RC3L5B1	RC4L5B1	RC5L5B1	RC6L5B1	RC7L5B1	05.In		
10	216	200	184	164	142	122	8	30	52	71	86	102		112	17	
4.Out	LC6L4B1	LC5L4B1	LC4L4B1	LC3L4B1	LC2L4B1	LC1L4B1	RC1L4B1	RC2L4B1	RC3L4B1	RC4L4B1	RC5L4B1	RC6L4B1	RC7L4B1	04.In		
11	228	214	198	182	160	138	12	5	21	43	65	81	97		111	16
3.Out	LC6L3B1	LC5L3B1	LC4L3B1	LC3L3B1	LC2L3B1	LC1L3B1	RC1L3B1	RC2L3B1	RC3L3B1	RC4L3B1	RC5L3B1	RC6L3B1	RC7L3B1	03.In		
12	227	212	196	180	158	136	120	3	19	41	63	79	95		110	15
2.Out	LC7L2B1	LC6L2B1	LC5L2B1	LC4L2B1	LC3L2B1	LC2L2B1	LC1L2B1	RC1L2B1	RC2L2B1	RC3L2B1	RC4L2B1	RC5L2B1	RC6L2B1	RC7L2B1	02.In	
13	226	210	194	178	156	134	118	1	17	39	61	77	93	109	14	1.In
1.Out	LC7L1B1	LC6L1B1	LC5L1B1	LC4L1B1	LC3L1B1	LC2L1B1	LC1L1B1	RC1L1B1	RC2L1B1	RC3L1B1	RC4L1B1	RC5L1B1	RC6L1B1	RC7L1B1		

 = RPC

 = Board

Fig. C.6: The local board numbers in the trigger chamber plane.

D Fit parameters for the iteration procedure on tuning of the input MC shapes

The fit parameters for the iteration procedure are tabulated in all the tables of this appendix. See the section [5.3](#) for more details.

first iteration		first iteration		first iteration	
centrality 0–10 (%)		centrality 10–20 (%)		centrality 20–30 (%)	
parameters	values	parameters	values	parameters	values
A	1474179.8	A	884300.34	A	570136.43
B	3.5	B	3.48	B	3.49
n ₁	1.93	n ₁	1.94	n ₁	1.93
n ₂	3.96	n ₂	3.92	n ₂	3.96
C	-650.09	C	678.6	C	-5603.09
n ₃	1.03	n ₃	0.47	n ₃	1.33
first iteration		first iteration		first iteration	
centrality 30–40 (%)		centrality 40–90 (%)		centrality 40–90 (%)	
parameters	values	parameters	values	parameters	values
A	311811.62	A	377489.61		
B	3.49	B	3.48		
n ₁	1.94	n ₁	1.95		
n ₂	3.95	n ₂	3.92		
C	-1535.42	C	2233.03		
n ₃	1.25	n ₃	0.91		

Table D.1: First iteration fit parameters of empirical p_T functional form for generated J/ ψ for $2.5 < y < 4$ and several centrality classes.

480

second iteration		second iteration	
centrality 0–10 (%)		centrality 10–20 (%)	
parameters	values	parameters	values
A	960128.18	A	571699.52
B	2.85	B	2.94
n ₁	2.81	n ₁	2.67
n ₂	2.43	n ₂	2.5
C	201005.32	C	122835.49
n ₃	0.69	n ₃	0.64

Table D.2: Second iteration fit parameters of empirical p_T functional form for generated J/ ψ for $2.5 < y < 4$ and several centrality classes.

first iteration		first iteration		first iteration	
centrality 0–10 (%)		centrality 10–20 (%)		centrality 20–30 (%)	
parameters	values	parameters	values	parameters	values
A	1030648.09	A	596170.22	A	424100.93
B	2.85	B	2.94	B	3.11
n ₁	2.81	n ₁	2.67	n ₁	2.36
n ₂	2.43	n ₂	2.50	n ₂	2.92
C	215765.94	C	128583.46	C	45700.64
n ₃	0.69	n ₃	0.64	n ₃	0.55
first iteration		first iteration		first iteration	
centrality 30–40 (%)		centrality 40–90 (%)		centrality 40–90 (%)	
parameters	values	parameters	values	parameters	values
A	169952.27	A	257093.73		
B	3.15	B	4.17		
n ₁	2.66	n ₁	1.90		
n ₂	2.49	n ₂	4.21		
C	57532.4623	C	16444.56		
n ₃	0.58	n ₃	0.89		

Table D.3: First iteration fit parameters of empirical p_T functional form for corrected J/ ψ yield from data for $2.5 < y < 4$ and several centrality classes.

second iteration		second iteration	
centrality 0–10 (%)		centrality 10–20 (%)	
parameters	values	parameters	values
A	991641.93	A	583729.42
B	2.85	B	2.93
n ₁	2.84	n ₁	2.7
n ₂	2.39	n ₂	2.46
C	211778.63	C	129170.74
n ₃	0.69	n ₃	0.64

Table D.4: Second iteration fit parameters of empirical p_T functional form for corrected J/ ψ yield from data for $2.5 < y < 4$ and several centrality classes.

first iteration		first iteration		first iteration	
centrality 0–10 (%)		centrality 10–20 (%)		centrality 20–30 (%)	
parameters	values	parameters	values	parameters	values
A	5498539.1	A	3569209.3	A	2423655.77
n ₁	-0.11	n ₁	-0.03	n ₁	-0.0006
n ₂	2.09	n ₂	2.11	n ₂	2.13
first iteration		first iteration			
centrality 30–40 (%)		centrality 40–90 (%)			
parameters	values	parameters	values		
A	1342126.63	A	1579359.94		
n ₁	0.0241	n ₁	0.02		
n ₂	2.13	n ₂	2.13		

Table D.5: First iteration fit parameters of empirical rapidity functional form for generated J/ ψ for $0 < p_T < 20$ and several centrality classes.

second iteration		second iteration	
centrality 0–10 (%)		centrality 10–20 (%)	
parameters	values	parameters	values
A	2517844.17	A	2035258.53
n ₁	-2.43	n ₁	-1.53
n ₂	1.08	n ₂	1.6

Table D.6: Second iteration fit parameters of empirical rapidity functional form for generated J/ ψ for $0 < p_T < 20$ and several centrality classes.

first iteration		first iteration		first iteration	
centrality 0–10 (%)		centrality 10–20 (%)		centrality 20–30 (%)	
parameters	values	parameters	values	parameters	values
A	2517878.20	A	2035273.88	A	2616534.52
n ₁	-2.43	n ₁	-1.53	n ₁	0.44
n ₂	1.08	n ₂	1.6	n ₂	2.34
first iteration		first iteration			
centrality 30–40 (%)		centrality 40–90 (%)			
parameters	values	parameters	values		
A	632140.69	A	779875.31		
n ₁	-1.81	n ₁	-1.81		
n ₂	1.63	n ₂	1.54		

Table D.7: First iteration fit parameters of empirical rapidity functional form for corrected J/ ψ yield from data for $0 < p_T < 20$ and several centrality classes.

second iteration		second iteration	
centrality 0–10 (%)		centrality 10–20 (%)	
parameters	values	parameters	values
A	2517878.20	A	2035273.88
n ₁	-2.43	n ₁	-1.53
n ₂	1.08	n ₂	1.6

Table D.8: Second iteration fit parameters of empirical rapidity functional form for corrected J/ψ yield from data for $0 < p_T < 20$ and several centrality classes.

481 E Acceptance efficiency and checks

482 This appendix shows the presentations that discuss the checks on the acceptance and efficiency. For $A \times \varepsilon$
 483 in 0–20%, its weights of the run number and centrality were not properly applied when integrating over
 484 centrality and run numbers. Those checks and the corrections can be found in [13, 14]. Table E.1 shows
 485 the corrected $A \times \varepsilon$ in 0–20%.

centrality 0 – 20 %	
p_T (GeV/c)	$A \times \varepsilon \pm$ stat. (%)
0–0.3	0.139 ± 0.0008 (0.56)
0.3–1	0.130 ± 0.0003 (0.26)
1–2	0.112 ± 0.0002 (0.20)
2–3	0.115 ± 0.0003 (0.23)
3–4	0.140 ± 0.0004 (0.31)
4–5	0.181 ± 0.0007 (0.39)
5–6	0.228 ± 0.0013 (0.57)
6–7	0.274 ± 0.0021 (0.77)
7–8	0.311 ± 0.0032 (1.00)
8–9	0.338 ± 0.0047 (1.40)
9–10	0.371 ± 0.0071 (1.90)
10–11	0.387 ± 0.0106 (2.70)
11–12	0.414 ± 0.0162 (3.90)
12–15	0.449 ± 0.0137 (3.00)
15–20	0.505 ± 0.0321 (6.30)

Table E.1: J/ψ acceptance times efficiency as a function of p_T for $2.5 < y < 4$ and 0–20% centrality class.

486 References

- 487 [1] **ALICE** Collaboration, “Quarkonium signal extraction in ALICE,” 2015.
488 <https://cds.cern.ch/record/2060096>.
- 489 [2] A. M. and, “J/ ψ and $\psi(2S)$ cross sections in pp collisions at $\sqrt{s} = 13$ TeV measured with the
490 Muon tracker,” in Analysis Note. 2016. <https://alice-notes.web.cern.ch/node/497>.
- 491 [3] R. Arnaldi *et al.*, “J/ ψ production in Pb-Pb collisions at $\sqrt{s} = 2.76$ TeV,” 2014.
492 <https://alice-notes.web.cern.ch/node/340>.
- 493 [4] N. Valle and S. Aziz, “Z boson production in Pb-Pb collisions at $\sqrt{s_{NN}} = 5.02$ TeV LHC in 2018,”
494 in Regular Public Note. 2019. <https://alice-notes.web.cern.ch/node/952>.
- 495 [5] A. Toia, “Centrality determination in heavy ion collisions,” 2017.
496 <http://cds.cern.ch/record/2636623>.
- 497 [6] O. Bugnon, “Muon tracking efficiency for LHC18r and LHC18q,” in Talk. 2019.
498 https://indico.cern.ch/event/796503/contributions/3359823/attachments/1822060/2980665/MuonTrackingEfficiency_PbPb5TeV.pdf.
- 500 [7] B. Audurier *et al.*, “Multi-differential studies of J/ ψ production in Pb-Pb collisions at $\sqrt{s} = 5.02$
501 TeV,” 2017. <https://alice-notes.web.cern.ch/node/581>.
- 502 [8] H. Hushnud *et al.*, “Differential studies of J/ ψ production as a function of rapidity in Pb-Pb
503 collisions at $\sqrt{s} = 5.02$ TeV,” in Analysis Note. 2019.
504 <https://alice-notes.web.cern.ch/node/721>.
- 505 [9] **ALICE** Collaboration [Phys. Lett. B766](#) (March, 2017) 212–224, arXiv:1606.08197
506 [[nucl-ex](#)].
- 507 [10] C. L. Huang, H. Hushnud, *et al.*, “J/ ψ production in pp collisions at $\sqrt{s} = 5.02$ TeV with the 2017
508 data sample,” in Analysis Note. 2019. <https://alice-notes.web.cern.ch/node/909>.
- 509 [11] **Particle Data Group** Collaboration, M. Tanabashi *et al.* [Phys. Rev. D98](#) no. 3, (2018) 030001.
- 510 [12] **ALICE** Collaboration [J. High Energ. Phys. 2020](#) (2020) 41, arXiv:1909.03158 [[nucl-ex](#)].
- 511 [13] C. L. Huang, “Inclusive J/ ψ production as a function of p_T and centrality at forward rapidity in
512 Pb-Pb collisions at $\sqrt{s_{NN}} = 5.02$ TeV,” in Talk. 2020. https://indico.cern.ch/event/912459/contributions/3837516/attachments/2025311/3400891/2020_DQ_May_5.pdf.
- 513 [14] C. L. Huang, “Inclusive J/ ψ production as a function of p_T and centrality at forward rapidity in
514 Pb-Pb collisions at $\sqrt{s_{NN}} = 5.02$ TeV,” in Talk. 2020.
515 https://indico.cern.ch/event/913249/contributions/3856082/attachments/2039406/3415110/2020_0515_update_ALICE_approval.pdf.